6-1-2017

# Characterizing Resident Space Object Earthshine Signature Variability

Jared D. Van Cor

jdv8762@rit.edu

# Characterizing Resident Space Object Earthshine Signature Variability

by

Jared D. Van Cor

A thesis submitted in partial fulfillment of the
requirements for the degree of Master of Science
in the Chester F. Carlson Center for Imaging Science
College of Science
Rochester Institute of Technology

June 01, 2017

Signature of the Author ⎯⎯⎯⎯⎯⎯⎯⎯⎯⎯⎯⎯⎯⎯⎯⎯⎯⎯⎯⎯⎯⎯

Accepted by ⎯⎯⎯⎯⎯⎯⎯⎯⎯⎯⎯⎯⎯⎯⎯⎯⎯⎯⎯⎯⎯⎯⎯⎯⎯
            Coordinator, M.S. Degree Program          Date

CHESTER F. CARLSON CENTER FOR IMAGING SCIENCE

COLLEGE OF SCIENCE

ROCHESTER INSTITUTE OF TECHNOLOGY

ROCHESTER, NEW YORK

<u>CERTIFICATE OF APPROVAL</u>

---

M.S. DEGREE THESIS

---

The M.S. Degree Thesis of Jared D. Van Cor
has been examined and approved by the
thesis committee as satisfactory for the
thesis required for the
M.S. degree in Imaging Science

_____

Dr. Michael Gartley , Thesis Advisor

_____

Dr. John Kerekes

_____

Dr. Rolando Raqueno

_____

Date

# Characterizing Resident Space Object Earthshine Signature Variability

by

Jared D. Van Cor

Submitted to the
Chester F. Carlson Center for Imaging Science
in partial fulfillment of the requirements
for the Master of Science Degree
at the Rochester Institute of Technology

## Abstract

There are three major sources of illumination on objects in the near Earth space environment: Sunshine, Moonshine, and Earthshine. For objects in this environment (satellites, orbital debris, etc.) known as Resident Space Objects (RSOs), the sun and the moon have consistently small illuminating solid angles and can be treated as point sources; this makes their incident illumination easily modeled. The Earth on the other hand has a large illuminating solid angle, is heterogeneous, and is in a constant state of change. **The objective of this thesis was to characterize the impact and variability of observed RSO Earthshine on apparent magnitude signatures in the visible optical spectral region.**

A key component of this research was creating Earth object models incorporating the reflectance properties of the Earth. Two Earth objects were created: a homogeneous diffuse Earth object and a time sensitive heterogeneous Earth object. The homogeneous diffuse Earth object has a reflectance equal to the average global albedo, a standard model used when modeling Earthshine. The time sensitive heterogeneous Earth object was created with two material maps representative of the dynamic reflectance of the surface of the earth, and a shell representative of the atmosphere. NASA's Moderate-resolution Imaging Spectroradiometer (MODIS) Earth observing satellite product libraries, MCD43C1 global surface BRDF map and MOD06 global fractional cloud map, were utilized to create the material maps, and a hybridized version of the Empirical Line Method (ELM) was used to create the atmosphere. This dynamic Earth object was validated by comparing simulated color

imagery of the Earth to that taken by: NASAs Earth Polychromatic Imaging Camera (EPIC) located on the Deep Space Climate Observatory (DSCOVR), and by MODIS located on the Terra satellite.

The time sensitive heterogeneous Earth object deviated from MODIS imagery by a spectral radiance root mean square error (RMSE) of $\pm 14.86[\frac{watts}{m^2 sr \mu m}]$ over a sample of ROIs. Further analysis using EPIC imagery found a total albedo difference of $+0.03\%$ and a cross correlation of 0.656. Also compared to EPIC imagery it was found our heterogeneous Earth model produced a reflected Earthshine radiance RMSE of $\pm 28[\frac{watts}{m^2 sr \mu m}]$ incident on diffuse spherical RSOs, specular spherical RSOs, and diffuse flat plate RSOs with an altitude of 1000km; this resulted in an apparent magnitude error of $\pm 0.28$. Furthermore, it was found our heterogeneous Earth model produced a reflected Earthshine radiance RMSE of $\pm 68[\frac{watts}{m^2 sr \mu m}]$ for specular flat plate RSOs with an altitude of 1000km; this resulted in an apparent magnitude error of $\pm 0.68$.

The Earth objects were used in a workflow with the Digital Imaging and Remote Sensing Image Generation (DIRSIG) tool to explore the impact of a range of characteristic RSO geometries, geographies, orientations, and materials on the signatures from an RSO due to Earthshine. An apparent magnitude was calculated and used to quantify RSO Earthshine signature variability; this is discussed in terms of the RMSE and maximum deviations of visible RSO Earthshine apparent magnitude signatures comparing the homogeneous Earth model to heterogeneous Earth model. The homogeneous diffuse Earth object was shown to approximate visible RSO Earthshine apparent magnitude signatures from spheres with a RMSE in reflected Earthshine apparent magnitude of $\pm 0.4$ and a maximum apparent magnitude difference of 1.09 when compared to the heterogeneous Earth model. Similarly for diffuse flat plates, the visible RSO Earthshine apparent magnitude signature RMSE was shown to be $\pm 0.64$, with a maximum apparent magnitude difference of 0.82. For specular flat plates, the visible RSO Earthshine apparent magnitude signature RMSE was shown to be $\pm 0.97$ with maximum apparent magnitude difference of 2.26.

This thesis explored only a portion of the parameter dependencies of Earthshine, but has enabled a preliminary understanding of visible RSO Earthshine signature variability and its geometric dependence. This research has demonstrated the impact of Earth heterogeneity on the observed apparent magnitude signatures of RSOs illuminated by Earthshine and the potential for error that comes with approximating the Earth as a diffuse homogeneous object.

# Acknowledgements

I am grateful for the experience I have had as part of the Center for Imaging Science's graduate class. The program taught me the tools to work on problems of the greatest real world significance to the smallest interesting hobby ventures. I was provided an environment surrounded by what I have come to know as some of the smartest people, along with the most interesting and supportive friends a person could hope for. It has been the period of my life where I have experienced the most stress, excitement, business, and fulfillment, and I think the period I have grown the most as a scientist and human being.

Several people have helped me complete my research. My adviser, Dr. Michael Gartley whose inspiring genius and continued support, patience, and efforts have made my research possible, interesting, and fun. Dr. Rolando Raqueno's whose boundless willingness to help me trouble shoot programmatic issues has made some of my most stressful moments disappear. Dr. John Kerekes, who took on the major responsibility of helping turn my pile of work into a cohesive paper. The DIRSIG user group, namely the developers Scott Brown and Adam Goodenough, who gave me a platform to discuss my research and gave me thorough thoughtful feedback and direction. Finally, the DIRS group where I practiced presenting my research and gave me thoughtful feed back. Many more people helped in many ways, but the fore-mentioned put forth the largest efforts on my behalf.

# Contents

# List of Figures

**List of Symbols**

| | |
|---|---|
| $alt$ | Altitude [m] |
| $m$ | Apparent Magnitude [ ] |
| $\delta m$ | Apparent Magnitude Error [ ] |
| $\theta$ | Azimuth angle [$degrees$] |
| $\rho_{BRF}$ | Bidirectional Reflectance Factor, $\pi * \rho_{BRDF}$ [ ] |
| $\rho_{BRDF}$ | Bidirectional Reflectance Distribution Function [$\frac{1}{sr}$] |
| $XC$ | Cross Correlation Coefficient [ ] |
| Q | Energy [J] |
| $M$ | Exitance [$\frac{W}{m^2}$] |
| $\delta M$ | Exitance Error [$\frac{W}{m^2}$] |
| $\delta$ | Extinction Coefficient [$\frac{1}{km}$] |
| $\Phi$ | Flux [W] |
| $fl$ | Focal Length [m] |
| $I$ | Intenisty [$\frac{W}{sr}$] |
| $E$ | Irradiance [$\frac{W}{m^2}$] |
| $n_i$ | Number of Pixels in row or column i [ ] |
| P | Pixel Pitch [m] |
| $\rho$ | Reflectance [ ] |
| $\rho_{RSO}$ | Reflectance Of resident Space Object [ ] |
| $L$ | Radiance [$\frac{W}{m^2 sr}$] |
| $\delta L$ | Radiance Error [$\frac{W}{m^2 sr}$] |
| $RMSE$ | Root Mean Square Error [$Context\ Dependent$] |
| $r$ | Slant Range [m] |
| $\Omega$ | Solid Angle [sr] |
| $\Omega_{RSO}$ | Solid Angle of Resident Space Object [sr] |
| $R_\lambda$ | Spectral Response [$\frac{1}{\mu m}$] |
| $R_i$ | Spectral Response of the $ith$ element [$\frac{1}{\mu m}$] |
| $\tau$ | Transmission [ ] |
| $\lambda$ | Wavelength [nm] |
| $\phi$ | Zenith angle [$degrees$] |

**List of Acronyms**

| | |
|---|---|
| BRDF | Bidirectional Reflectance Distribution Function |
| COART | Coupled Ocean Atmosphere Radiative Transfer |
| DIRS | Digital Imaging and Remote Sensing |
| DIRSIG | Digital Imaging and Remote Sensing Image Generation |
| ELM | Empirical Line Method |
| ENU | East North Up |
| EPIC | Earth Polychromatic Imaging Camera |
| ESC | EarthShine Contamination |
| FOV | Field Of View |
| FOHS | Flat Opaque Homogeneous Surface |
| GBSS | Ground-Based Space Surveillance |
| GEO | Geosynchronous Earth Orbit |
| GSD | Ground Sample Distance |
| Lat | Latitude |
| LEO | Low Earth Orbit |
| Lon | Longitude |
| MCAT | Meter Class Autonomous Telescope |
| mdpt | mid point |
| MEO | Mid Earth Orbit |
| MODEST | Michigan Orbital Debris Survey Telescope |
| MODIS | The Moderate Resolution Spectrometer |
| MODTRAN | MODerate resolution atmospheric TRANsmission |
| MSX | Midcourse Space Experiment |
| MTF | Modulation Transfer Function |
| NASA | National Aeronautics and Space Administration |
| Obs | Observatory |
| ODB | Object Database |
| PSF | Point Spread Function |
| ROI | Region of Interest |
| RSO | Resident Space Object |
| SBSS | Space-Based Space Surveillance |
| SBV | Space-based Visible |
| SD | Solar Diffuser |
| SEO | Sun Earth Object |
| SEV | Sun-Earth-Vehicle |
| SOO | Source-Object-Observatory |
| SNR | Signal to Noise Ratio |
| SSN | Space Surveillance Network |
| UKIRT | United Kingdom Infrared Telescope |
| VIIRS | Visible/Infrared Imaging Radiometer Suite |

# Chapter 1

# Introduction and Objectives

The past 60 years have given rise to the mechanized utilization of the exoatmosphere. The 1967 Space Treaty made the exoatmosphere accessible to the global community for peaceful purposes, but this did not completely do away with the threats that face space assets and exploration [5,6]. With the number of countries with space assets reaching 60 and growing, the amount of debris and potential for costly catastrophe has increased as well [7]. Currently there are over 16,000 known Resident Space Objects (RSOs) 10cm or larger, an estimated 300,000 10-1cm, and millions of smaller RSOs in orbit about the Earth - the majority of these objects coming from human space activity [7].

In order to begin to mitigate this risk, Ground-Based Space Surveillance (GBSS) and Space-Based Space Surveillance (SBSS) systems have been tasked to examine, identify, and catalog RSOs. Current state of the art system's are capable of detection, tracking, and in the case of large targets, spatially and spectrally resolving RSOs illuminated by the solar radiation [8]. Depending solely on solar radiation makes the window of Source-Object-Observatory (SOO) angles which an object can be imaged small. This is because of the relatively small solid angle of the sun, Earth shadowing, and near Earth orbital speeds. This problem is compounded by bidirectional reflectance distribution functions (BRDFs) with primarily directional lobes. While the sun offers the brightest source of natural illumination in the near Earth space environment, it is not the only one.

There are three major sources of illumination in the near Earth space environment: Sunshine, Earthshine, and Moonshine. While Sunshine is the brightest of the three, the geometric and reflectance properties of the Earth make it a potentially better source given a range of conditions. Predicting Sunshine and Moonshine onto RSOs is quite simple due to their accurate approximation as point sources from the perspective of RSOs. The Earth on the other hand has a relatively large solid angle, a heterogeneous surface, and is in a constant state of flux.

To obtain optimal performance when developing an imaging system for a mission or related survey strategies, an understanding of the dynamic range of the free variables of the system is quintessential. One way of exploring this is building models using Digital Imaging and Remote Sensing Imaging Generation (DIRSIG). DIRSIG connects a series of submodels through the integration of a suite of physics based radiation transfer modules, tracing photons from source to scene to focal plane [9]. DIRSIG, in its current iteration, is used primarily for simulating the imagery of airborne systems observing ground objects under homogeneous atmospheres. This makes the exploration of Earthshine in RSO detection not conform to the higher

level work flow typically implemented in DIRSIG. This thesis creates a work flow which bridges this gap for the purposes of better understanding of RSO signature sensitivity to the heterogeneity of the Earth given a range of free variables.

## 1.1  Objectives

The primary objectives of this work was to create and validate a time sensitive work flow for modeling the detection of RSO and employ it to explore the sensitivity of observed RSO Earthshine apparent magnitude signatures to the actual heterogenity of the Earth. Specific tasks include:

(a) Create a time sensitive Earth object with surface properties consistent with the spatial and temporal variability of the Earth;

(b) Analyze the validity of our model by comparing simulated Earth images to those taken by the Earth Polychromatic Imaging Camera (EPIC) and Moderate-resolution Imaging Spectroradiometer (MODIS);

(c) Create a work flow which: given an object, date, and time, creates the geometric appropriate DIRSIG parameters for assembling the scenario;

(d) Explore the geographical *phase* variability in the reflectance using a diffuse world approximation;

(e) Use the model to examine the standard deviation from the diffuse Earth model.

## 1.2  Thesis Overview

Chapter 2 presents some background on the state of imaging RSOs, Earthshine research, and DIRSIG modeling. Chapter 3 provides a theoretical basis for understanding our exploration into the modeling of Earthshine's contribution in the detection of RSOs using DIRSIG. Chapter 4 discusses the inner workings of our DIRSIG workflow, explaining how we set up the geometric skeleton and then process imagery to make a 3 layer Earth objects out of the geometry. It then discusses its validity through comparison with ground truth imagery.

Chapter 5 uses the model described in chapter 4 to compare the apparent magnitude of Sunshine and Earthshine illuminated characteristic RSOs given a

homogeneous Earth object and our real Earth object over a range of geographic, geometric, and material parameters. Here we primarily concern ourselves with the apparent magnitude of an object given the different free variables of the system in order to contrast our real Earth model to the homogeneous model and determine RSO sensitivity to real Earth heterogeneity. We conclude this section with a summary of our results. Chapter 6 concludes our findings.

# Chapter 2

# Background

This chapter provides a background in which to contextualize our Earthshine analysis into the real world. Section 2.1 explores the problem of space debris, the systems employed by NASA's Space Surveillance Network (SSN) used to detect and catalog RSOs, and the heterogeneity in Earthshine. Section 2.2 explores some of the related research into Earthshine, introduces DIRSIG, and shows the closest to parallel work done into using DIRSIG for exploring Earthshine.

## 2.1 Identification and Significance of Research

Earth orbiting spacecrafts are an integral part of our modern world. Collisions between RSOs pose a real and growing threat to the safety of these spacecrafts [10–12]. Several events have brought the danger of collision to the forefront of the community's attension: the break up of satellites at Geostationary Earth Orbit (GEO) including the 1978 break up of the Russian Ekran 2 and the 1992 break up of the U.S. Titan IIIC Transtage; the Chinese 2007 anti-satellite missle test that destroyed the FY-1C in Low Earth Orbit (LEO); and the 2009 collision between the functional Iridium 33 satellite and the non-functional Kosmos 2251 [13]. As part of mitigating this threat, NASA's Orbital Debris Program office has placed great emphasis on obtaining direct RSO measurements from their Space Survalience Network (SSN) of optical and RADAR systems [10]. Current active and proposed optical systems rely on solar radiation as their source of illumination onto their observed RSOs [8,10]. The SOO geometry required for optical observation of RSOs place rigid geographical and survey constraints on GBSS and orbital constraints on SBSS.

### 2.1.1 The State of Detecting RSOs

NASA's SSN is comprised of a number of optical telescopes and RADAR stations. RADAR has been the preferred method for measuring LEO RSOs for it's independent source of illumination, large Field of View (FOV), and the capability to penetrate clouds; but it has fundimental limititations. The efficiency of electromagnetic radiation scattering drops off at a precipitous $1/r^4$, where $r$ is the slant range. [10]. Furthermore, the RADAR cross section drops off with size and operating frequency [14]. Most existing and planned RSO observing RADAR systems operate within the S-band, with frequencies of 2-5 Gigahertz (6-15 cm wavelength).

With a 3 Gigahert system, a perfectly conducting 1mm sphere will have a radar cross section 5 orders of magnitude smaller then its geometric cross section, compared to a typical X-band system of 10 Gigahertz, which will be 800 times smaller. Unfortunately, atmospheric absorption limits the feasibility of utilizing frequencies beyond the X-band. [15].

Until recently, SSN optical systems have been used as the primary means of detection for objects in far MEO (Medium Earth Orbit) and GEO [10, 13]. This is because the fore mentioned frequency and power constraints posed by deep space RADAR observation, and the *too-short arc* problem posed by the high orbital velocities of near Earth RSOs [16]. Performance of optical systems observing unresolved space objects is characterized by the ability to detect an object of a given apparent magnitude ($m_{obj}$). For perspective, a 1m diameter (d) spherical object with a diffuse reflectance ($\rho$) of 0.175, located 36,000km (R) from a SSBS, and a solar phase angle ($\Psi$) of 15 degrees will have an approximate apparent magnitude of 13.4, determined by:

$$m_{obj} = m_{sun} - 2.5 log[\frac{d^2}{R^2}\rho_{diff}p_{diff}(\Psi)] \tag{2.1}$$

where $p_{diff}(\Psi) = \frac{2}{3pi}[sin(\Psi) + (\pi - \Psi)cos(\Psi)]$ - the phase equation [17]. The resulting signal to noise ratio (SNR) is given by:

$$SNR = \frac{e_s}{\sqrt{e_b + e_n^2}} \tag{2.2}$$

where $e_s$ is the signal photoelectron , $e_b$ is the background photoelectrons, and $e_n$ is the detector noise electrons.

Detection is typically considered to be plausible with an SNR of 5, but in practice can be reduced by taking multiple images. The SNR becomes more complicated when objects have a relative velocity greater then the sample distance of a single pixel scaled by the integration time, but typically this is mitigated by a matched platform motion [18]. For GBSS, both the signal photoelectrons and background photoelectrons are contingent on the atmosphere. In an environment with negligible sources of artificial light, the brightness of the sky ranges from 18 $[\frac{mag}{arcsec^2}]$ for a full moon to 22 $[\frac{mag}{arcsec^2}]$ for a new moon. For a GBSS with a pixel sampling of 0.60", faint minimum object detection size increases $\approx 2.5\%$ per 0.1 apparent magnitude increase in sky brightness - typically ranging from 20% to 80%. Furthermore, atmospheric extinction will decrease the signal photoelectrons. This will increase the

minimum RSO observable size by 20% to 30%, depending on observatory altitude and atmospheric conditions [13, 19].

Since the mid 1950s, starting with the United States deployment of a network of Baker Nunn satellite tracking cameras, optical systems have been tasked with detecting and tracking RSOs [20]. The current work horse of the United States' SSN is the Ground-based Electro-Optical Deep Space Surveillance (GEODSS) network, serving as the primary means in which objects in the geosynchronous region (36000km) of space are detected and tracked by the United States. GEODSS is comprised of three sites, each with two main and one auxiliary telescope, capable of detecting and tracking objects as faint as an apparent magnitude of 16 [10]. The GEODSS Network is controlled by the Air Force and is not typically experimentally tasked.

Since 2001, NASA has utilized the 0.61m aperture Michigan Orbital Debris Survey Telescope (MODEST) in Chili to help characterize the GEO debris environment [10, 21, 22]. MODEST is able to observe objects as faint as apparent magnitude 18. To a lesser extent, NASA has also utilized the 6.5m Magellan telescopes, able to detect objects as faint as apparent magnitude 21 [21]. These telescopes have been confined to imaging the near GEO regime of space because of their relatively slow platform speeds. An optically similar system looking to keep a matched velocity for the ISS would need to be able to move 15 times as fast as to match a geosynchronous orbit.

The 3.8m aperture United Kindom Infrared Telescope (UKIRT) is the first optical telescope utilized by NASA able to follow LEO objects. However, due to the spectral regime which it occupies, it is only able to detect objects with an absolute magnitudes of 28, equivalent to an apparent magnitude 1 [23]. The 1.3m Meter Class Autonomous Telescope (MCAT) is the newest optical sensor dedicated to NASA's mission of characterizing the space debris environment, capable of detecting objects with an apparent magnitude of 19 [13, 24]. Optically MCAT does not offer much beyond the capabilities of MODEST. However, MCAT's fast tracking telescope, equally capable dome, and real-time Stare-Detect-Chase mode enables it the ability to survey the entirety of Earth's orbital space.

The Space-Based Visible SBV (SBV) system aboard the now decommissioned Midcourse Space Experiment (MSX) was the SSN's first and only SBSS. It served as an experimental platform for exploring the viability of spectral characterization of RSOs from space. It was capable of detecting objects with an apparent magnitude of 14.5 [25]. At the time of its decommissioning in 2008 it had spent all

of its fuel on its extended mission, this made it unable to preform any deorbiting maneuvers and ironically lead it to becoming space debris [26].

### 2.1.2 Earthshine

The solar reflected radiation emanating from the Earth onto an exoatmospheric object is referred to as Earthshine. The material compositions of the surface of the Earth vary spatially and temporally. This lends itself to a dramatic variation in surface reflectance properties. From the moon, where the incident solid angle encompasses a consistently large portion of the Earth, the Earth's average visible albedo is derived to be $0.297\pm0.005$ with daily fluctuations of approximately 5% [27].

For near Earth RSOs, the incident Earthshine illumination is much more sensitive to the heterogeneity of the surface the Earth. For example, Earthshine incident on the International Space Station (ISS) emanates from approximately $12x10^6 km^2$ (2.3% of the Earth's surface). If the ISS happens to be over Regina Canada in February, the Earthshine may primarily emanate from a snow covered surface with a diffuse albedo of approximately 0.83; that same spot's albedo 6 months later may drop to 0.20 [28]. If the ISS is over the middle of the pacific ocean, Earthshine may emanate primarily from a nearly specular surface with an albedo of approximately 0.06 (from first principles). Another thing to consider is that at any given time the Earth has an average fractional cloud cover of 75% [29]. A place on the Earth with a low albedo one hour can be partially or completely under the cover of high albedo clouds the next.

## 2.2 State of Research into Earthshine

No known research exists in exploring Earthshine as a source of illumination for imaging RSOs, but research with some parallels has been conducted into the effects of Earthshine Contamination (ESC) onto Solar Diffusers (SDs), and Earth's albedo as a means of observing the Earth's radiation budget $[1, 2, 30, 31]$. The Moderate Resolution Imaging Spectroradiometer (MODIS) and the Visible/Infrared Imaging Radiometer Suite (VIIRS) use a SD as one of their calibration sources. As these satellites enter the northern limb of the Earth on their polar orbits, they take an image of the sun oriented SD. Because the solar radiation is thought to be constant, they are able to determine the degradation of their receptive responsivities [30].

However, in the FOV of the SD of both MODIS and VIIRS, there is a portion of the sun illuminated Earth. Two models were used to examine the potential effects of Earthshine in both cases, a homogeneous diffuse Earth and a homogeneous ocean Earth model. Despite VIIRS having a larger portion of it's SD FOV include the sun illuminated Earth, both have been shown to have errors ranging from 0.25% to 4.5% [1,30][Fig-2.1]. This has a 1-1 correspondence to the grazing reflected radiation of the Earth given a range of materials, with the largest contribution emanating from water.
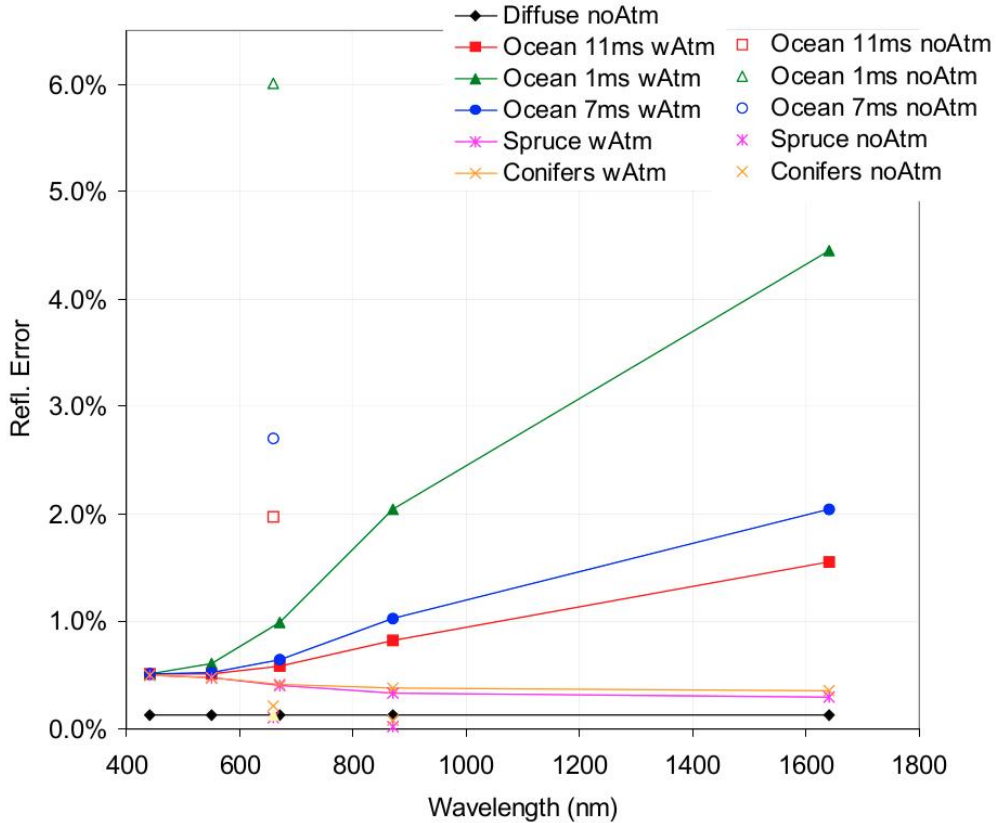


Figure 2.1: Earthshine modeling results for various surface types, with and without atmosphere [1].

NASA's Cloud and the Earth's Radiant Energy System (CERES) group

has utilized the MODIS system to create monthly global surface albedo products to explore the Earth radiation budget [Fig-2.2].
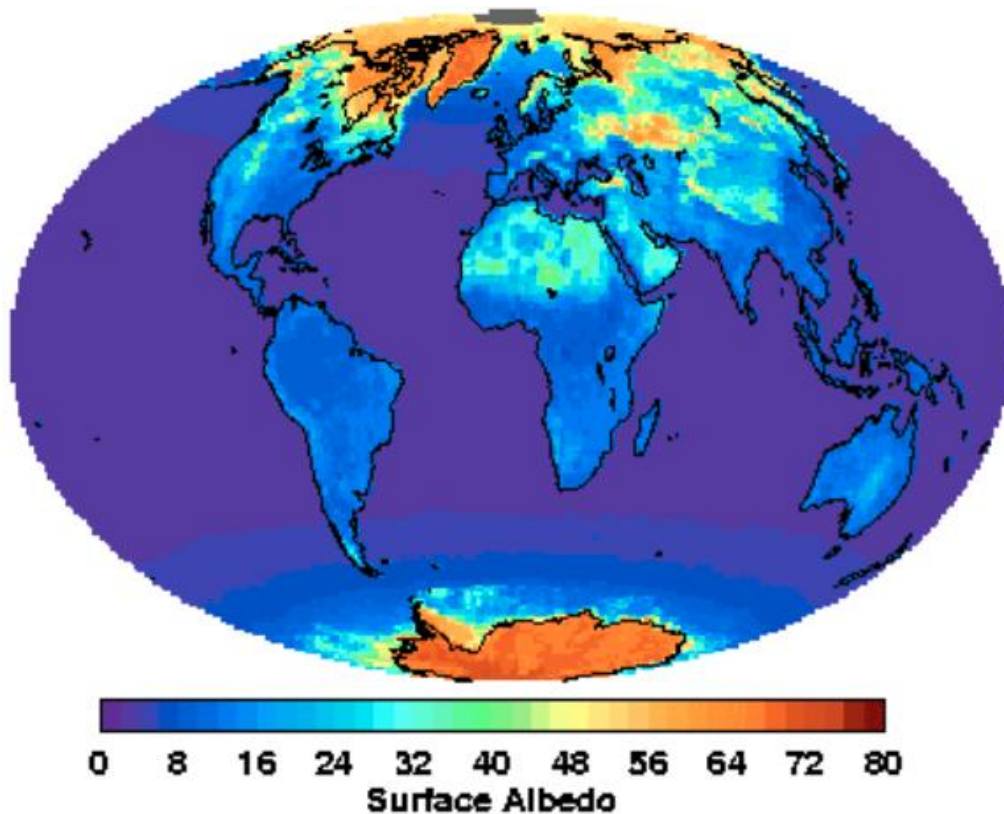


Figure 2.2: Global surface albedo derived by NASA's CERES group using MODIS [2]

To create the surface albedo map, first scene type is determined with a radiative transfer model and from that a fractional cloud map is derived [32]. Pixels determined to be cloud free are run against the Coupled Ocean Atmosphere Radiative Transfer (COART) model for surfaces expected to be snow and ice, and the Langley Fu & Lui model for all other surfaces, giving estimated pixel albedo. Finally, historical data are used for pixels determined to be cloudy throughout the month [2].

## DIRSIG Modeling of Earthshine

DIRSIG is a physics based synthetic image generation model developed by the Digital Imaging and Remote Sensing (DIRS) laboratory at the Rochester Institute of Technology (RIT). The model enables users to simulate single-band, multi-spectral, or hyperspectral imagery from the visible through thermal infrared region of the electromagnatic spectrum, along with Light Detection and Ranging (LIDAR) and Radio Frequency (RF) images. Given imaging system, scene, and atmosphere profiles, DIRSIG uses an adaptive sampling radiative transfer engine to propogate light from source to scene to system [9, 33]. DIRSIG has been used to symbolicly model Earthshine onto exoatmospheric objects[Fig-2.3].



Figure 2.3: DIRSIG recreations of a photo taken from the space shuttle during the fourth Hubble servicing mission [3]. Earthshine can be seen from the specular reflectance in the underside of the Hubble and Sunshine on the topside

However, our research is the first known venture into using a time sensitive radiometrically calibrated Earth object in DIRSIG, and furthermore, using it as a source to observe RSOs.

# Chapter 3

# Theory

This chapter provides a theoretical basis for understanding our exploration into modeling Earthshine. Section 3.1 introduces the core concepts of radiometry. Section 3.2 describes how reflectance models are used to approximate micro and macro BRDFs. Section 3.3 describes ray tracing and radiosity radiative transfer modeling. Finally, section 3.4 describes at how DIRSIG works.

## 3.1 Radiometry

Radiometry is the study of measuring light. While conceptually simple, it can be difficult to apply and cumbersome. Here we introduce the core radiometric concepts which will act as our foundation from which to discuss light.

### 3.1.1 Radiant Flux

Light is electromagnetic energy until it interacts with matter and turns into another form of energy. From microwaves turning into heat energy in the food in a microwave oven to solar radiation turning into kinetic energy on solar sails. The basic unit of energy is joules. Energy(Q) in radiometry usually deals with a continuous emmitters, opposed to finite packets such as the transfer of kinetic energy of two colliding objects. This makes the time derivative of the energy, **Radiant Flux** ($\Phi$), the most useful base unit from which to explore light.

$$\Phi = \frac{dQ}{dt} \quad [watts] \tag{3.1}$$

### 3.1.2 Radiant Flux Density

The **Radiant Flux Density** is the flux per unit area (dA), be it a real or a mathematical area construct. There are two conditions of Radiant Flux Density. Flux which is incident onto a surface is known as **Irradiance** (E). Flux which is exitent off a surface is known as **Exitance** (M).

$$E = \frac{d\Phi_{Incident}}{dA} \quad [\frac{watts}{m^2}] \tag{3.2}$$

$$M = \frac{d\Phi_{Exitent}}{dA} \quad [\frac{watts}{m^2}] \tag{3.3}$$

14

The relationship between these two terms on a shared surface can be used to explore the conservation of energy. At this time it maybe useful to introduce the idea of projected area. If the ray intersects a surface at an angle, the area is scaled by the dot product of the direction of incidence and the surface normal ($\hat{v} \cdot \hat{n}$, or equivalently the $\cos(\theta_{angleOfSeperation})$).

### 3.1.3 Radiant Intensity

**Radiant intensity** (I) is the energy emitted in a single direction. Instead of thinking about an illuminated object in terms of the it's projected area, we only consider the **solid angle**($\Omega$) which it subtends.

$$I = \frac{d\Phi}{d\Omega} \quad [\frac{watts}{sr}] \tag{3.4}$$

This becomes a useful tool for ray trace sampling, where radiation emanating from an area is not considered, but instead the directional incidence is considered.

### 3.1.4 Radiance

**Radiance** (L) may be considered as the energy of a single ray arriving or leaving a surface. A more formal definition requires thinking of that ray as a cone which subtends an infinitesimally small solid angle whose apex is on a surface.

$$L = \frac{d\Phi}{dAd\Omega} \quad [\frac{watts}{m^2 sr}] \tag{3.5}$$

Radiance is a useful construct because it is distance independent, meaning everywhere along the path of the ray has the same radiance.

### 3.1.5 Relating Radiometric Terms

Given the proper components, it is easy to go from one radiometric term to another. Given radiance, if one would like to know the irradiance onto the surface, one simply needs to know the relative solid angle subtended by the surface, or if one would like to know the intensity, one only need know the area. This provides the radiometric inquisitor a large number of tools for exploring the propogation of light, and multiple approaches to arriving at the solution.

## 3.2 Reflectance Models

When a surface is illuminated, three things can occur: the energy can be reflected, the energy can be transmitted, and/or the energy can be absorbed [Fig:3.1]. These are described by scale factors equal to the ratio of Exitance to Irradiance:

$$Reflectance(\rho) \equiv \frac{M_\rho}{E_I} \tag{3.6}$$

$$Transmittance(\tau) \equiv \frac{M_\tau}{E_I} \tag{3.7}$$

$$Absorption(\alpha) \equiv \frac{M_\alpha}{E_I} \tag{3.8}$$

where subscript $I$ indicates incident. These fundamental properties describe how all of the incident energy is conserved, that is:

$$\rho + \alpha + \tau = 1. \tag{3.9}$$

For the purposes of imaging, the absorption is not a useful term. What is useful is the amount of energy thermally emitted, this is described by a proportionality of Exitance at a given temperature to a black body at the same temperature

$$Emissivity(\epsilon) = \frac{M_\epsilon(T)}{M^{BB}(T)} \tag{3.10}$$
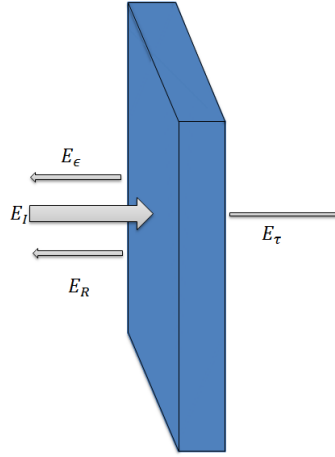
Figure 3.1: Representation of light interacting with matter

For materials in thermal equilibrium, the absorbed energy equals the emissive energy, this is an approximation often made and makes our energy balance look like:

$$\rho + \epsilon + \tau = 1. \tag{3.11}$$

Our treatment is a simplification of the total exitance from each term into a hemisphere about the surface normals. For reflectance, this total reflected radiation is called albedo ($\rho_a$). To describe the directional dependence of the reflectance, the **bidirectional reflectance distribution function** (BRDF) is used. This function is defined as the ratio of the surface leaving radiance to the incident irradiance.

$$f_{BRDF} = \frac{L(\theta_r, \phi_r)}{E(\theta_I, \phi_I)} [sr^{-1}] \tag{3.12}$$

For a lambertian material [Fig:3.2], a material that reflects energy equally in all directions, the BRDF reduces to:

$$f_{BRDF} = \frac{\rho_a}{\pi} \tag{3.13}$$
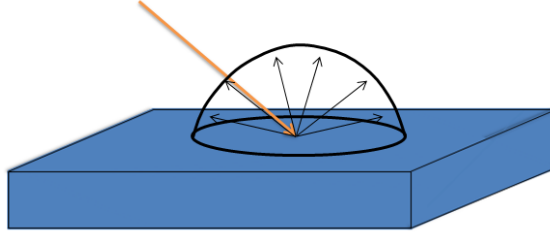
Figure 3.2: Representation of a Lambertian reflection

For an ideal specular material [Fig:3.3], a material that reflects all the energy at an angle equal to that of the angle of incidence, the BRDF reduces down to:

$$f_{BRDF} = \begin{cases} \rho_a, & \theta_r = \theta_I \ \& \ \phi_r = -\phi_I \\ 0, & \text{otherwise} \end{cases} \tag{3.14}$$
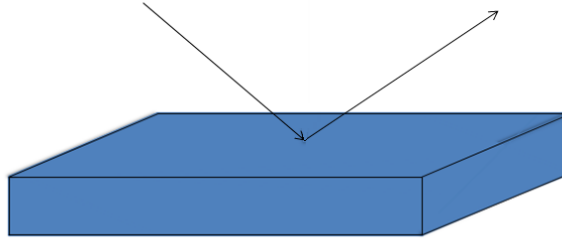


Figure 3.3: Representation of a specular reflection

For an ideal glossy material [Fig:3.5], a material that reflects all of the energy into a lobe about the specular reflection, the BRDF reduces down to:

$$f_{BRDF} = \frac{\rho_a}{4\pi\sigma_x\sigma_y\sqrt{(\hat{i}\cdot\hat{n})(\hat{o}\cdot\hat{n})}}e^{-((\frac{\hat{n}\cdot\hat{x}}{\alpha_x})^2+(\frac{\hat{n}\cdot\hat{y}}{\alpha_y})^2)} \tag{3.15}$$

Where $\sigma$ is refereed to as a roughness parameter, $\hat{i}$ is the unit incident direction vector, $\hat{o}$ is the unit exitance direction vector,$\hat{n}$ is the unit normal vector of the surface, $\hat{x}$ is the unit x coordinate vector, $\hat{y}$ is the unit y coordinate vector. The

roughness parameter dictates the size of the directional lobe and the distribution [34]. It tells us in angle where the Gaussian is equal to $\frac{1}{e}$ [Fig: 3.4]
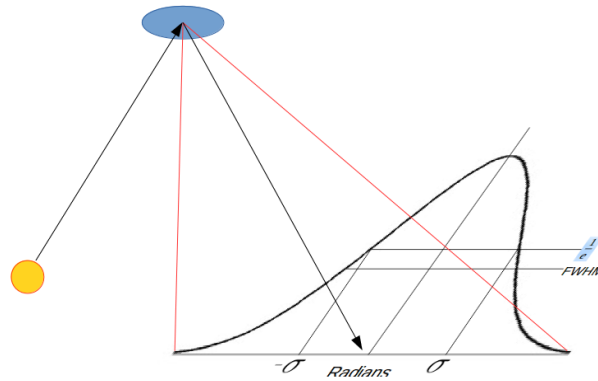


Figure 3.4: Representation of a specular lobe distribution

Within the bounds of $\pm\sigma$, 68% of the reflected energy is contained.
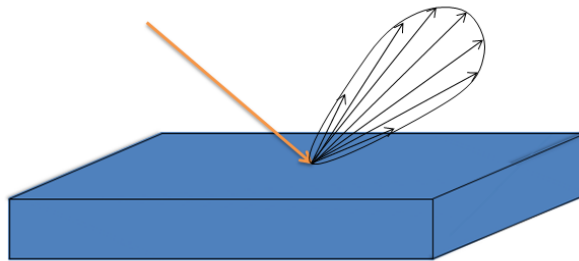


Figure 3.5: Representation of a specular lobe

These simple models embody the extremes of flat opaque homogeneous surfaces (FOHSs). In reality, most FOHSs are some mixture of these models. One common model used to represent more realistic FOHSs is the WardBRDF model [Fig: 3.6]. This model combines the Gaussian specular lobe with a diffuse compo-

19

nent. This BRDF looks like:

$$f_{BRDF} = \frac{\rho_d}{\pi} + \frac{\rho_a}{4\pi\sigma_x\sigma_y\sqrt{(\hat{i}\cdot\hat{n})(\hat{o}\cdot\hat{n})}}e^{-((\frac{\hat{n}\cdot\hat{x}}{\alpha_x})^2+(\frac{\hat{n}\cdot\hat{y}}{\alpha_y})^2)} \tag{3.16}$$
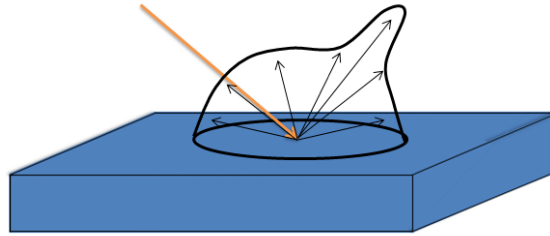


Figure 3.6: Representation of a diffuse object with a specular lobe

In nature, FOHSs are rare, yet treating surfaces as such can still be a viable approximation. Water, for example, given a variety of surface geometries, will still behave as a wardBRDF. A placid pond will have a tight lobe, appearing as an almost specular surface, with a diffuse contribution from internal reflection [Fig: 3.7].



Figure 3.7: Placid pond reflection
(Photo Credit https://christophermartinphotography.com/tag/hawaii/page/3/)

A pond with some surface roughness will still have a primarilly forward scattering, but with a blur proportional to the roughness, characteristic of a wider lobe [Fig: 3.8].

Figure 3.8: Pond with some roughness
(Photo Credit https://www.quora.com/What-were-your-impressions-of-visiting-Laos)

In practice, surfaces are defined by the observed resolution. A human observing a table may see a homogeneous surface, but give them a microscope and the underlying heterogeneity will become apparent. A surface comprised of microsurfaces with varying BRDFs may still be well approximated as a homogeneous macro surface with a single BRDF. For example, given an image with a high observed resolution of a forest, the individual pixels will have dramatically varying reflectances. But if we decrease the resolution, the inherent homogeneity of how a particular type of forest grows in a particular climate will show through [Fig: 3.9].



Figure 3.9: High resolution (left) vs low resolution (right) Image of Forest

While micro samples may show dramatically varying BRDFs, macro sampling can show an over all homogeneity. Taking the histogram of Digital Counts as

a function of intensity for our two images [Fig: ], we see the distribution is much tighter in the lower resolution image [Fig:3.10].
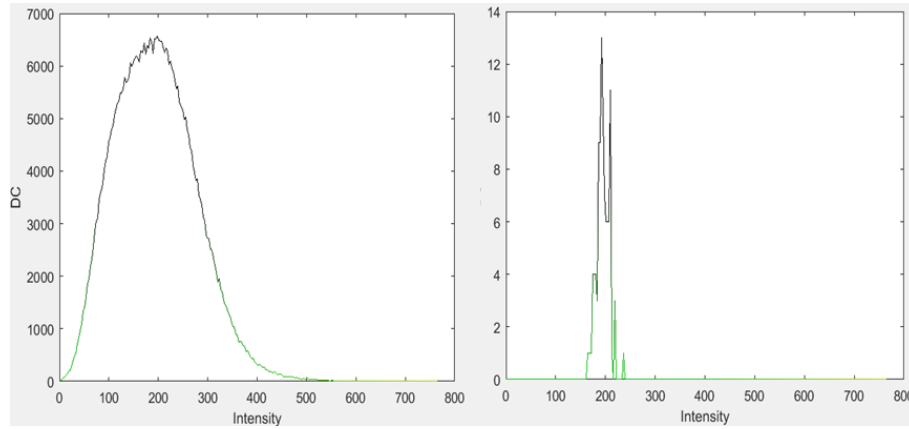


Figure 3.10: High resolution (left) vs low resolution (right) Histograms.

This can also be the case through out the different Source Object Observer (SOO) geometries. One kernel driven model used to capture the micro geometry inside of the macro sampling is the RossLi model [35]. Built upon the Ross leaf area index [36], and the Li mutual shadowing [37], the RossLi model combines these two characteristics of vegetation to create a way in which the underlying micro geometry is captured within the macro sampling. The components of which were derived and described by *Wanner et al* [35]. The RossLi BRDF is built upon the superposition of three geometric terms: An isotropic scaler, a scaled volumetric scattering kernel, and a scaled geometric scattering kernel.

$$R = f_{iso} + f_{geo}k_{geo} + f_{vol}k_{vol} \tag{3.17}$$

Where $f$ represents the scale factor of the kernels and k the kernels. The intricacies of the RossLi kernels are beyond the scope of this paper, but are built upon the SOO geometry, and: sparse/dense and thin/thick parameters. This model, though designed for vegetation, has enough dynamic range that it does a good job approximating a large range of non-specular non-glossy surfaces - this includes most macro samples of the Earth's land.

## 3.3 Modeling Radiative Transfer

Radiative transfer refers to how a traveling beam of radiation loses energy to absorption, gains energy by emission, and redistributes energy by scattering. This is typically done in stages when modeling the phenomology of the propergation of light. This can be something simple like light traveling unimpeded through the vacuum of space from a star to an aperture, or something much more complex such as radiation traveling through, and being reflected off different materials with complex geometries. There are many approaches to modeling radiative transfers: but we are going to narrow our focus to just two methods: Radiosity and Ray Tracing.

In image simulation, Radiosity and Ray Tracing are different means to approximating the electromagnatic energy onto a detector or detector array. Ray tracing works by tracing sampling lines along the directions of propogation of a Electromagnetic wave front ($\vec{k}$) as it undergoes Radiative Transfers, based on the FOV of each detector and the determined sampling technique. Radiosity on the other hand takes into account every single facet in the scene and for each, calculates the eminating radiation incident from every other facet. Each of these has fundamental benefits and limitations.

Ray tracing, while more robust, must resample the entire scene and the radiative transfer there in for every perturbation to system parameters and location. Radiosity on the other hand need only sample the facets in the field of view, because the subsequent calculations of radiative transfers is the same, i.e. system independent. This does not guarantee one method is ubiquitously faster then the other. The major short coming of radiosity is that it is unable to take into account non diffuse reflectances, while the major short coming of Ray tracing is that there is a chance that subpixel facets will be unsampled or under sampled. There are techniques and hybridizations of each which allow for an accounting of these shortcomings. In our case, we utilized both techniques independently to utilize their strengths to solve different problems. This section will primarily focus on basic implementation.

### 3.3.1 Ray Tracing Technique

Ray tracing can be done numerous ways. Rays can be traced from system to scene to source, from source to scene to system, or meet in the middle some how. The distinction is conceptually trivial. We will focus on the the first mentioned way as to follow the convention of DIRSIG. Light travels through space and optically

homogeneous material in a straight line, which we model as a ray. We know that the illumination originating from a point will fall off as $\frac{1}{r^2}$, where r is the slant range. The incident irradiance from a surface can be modeled as an array of point sources.

$$E = \sum_{i=1}^{n} \frac{I_i cos\theta_i}{d_i^2} \tag{3.18}$$
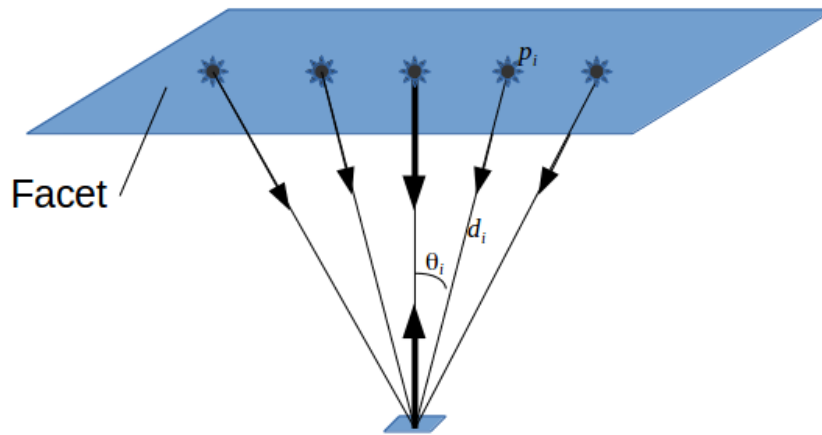


Figure 3.11: Modeling a facet as an array of point sources

There are a few complications though, each point ($p_i$) need be seen by the surface they are illuminating, we need know the distance, and we need know the intensity.

For scene modeling, this process is repeated for each reflection of each ray.
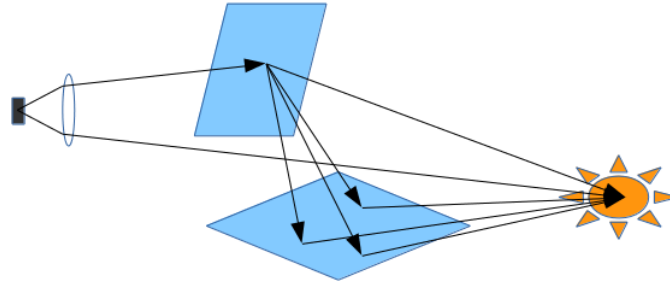
Figure 3.12: Modeling a facet as an array of point sources

At each intersection, the geometric and material properties of the surface are taken into account - scaling the ray appropriately. In reality, the contribution from each surface would take an infinite number of points to be precisely represented, and each subsequent reflectance another infinite number, so we are only able to sample the hemisphere in which the light is reflected each time, and must cut off the allowed number of inter-reflections somewhere.

### 3.3.2 Radiosity

Radiosity works by considering the contribution of every facet onto everyother facet. In its nonhybridized form it is unable to account for material properties. The incident irradiance from a surface can be modeled as a pyramid ray with the base area equal to the illuminating facet area $(dA_j)$.

$$E = L_i \frac{(\hat{n}_i \cdot \hat{r}_{ij})(\hat{n}_j \cdot \hat{r}_{ji})dA_j}{r^2} \tag{3.19}$$
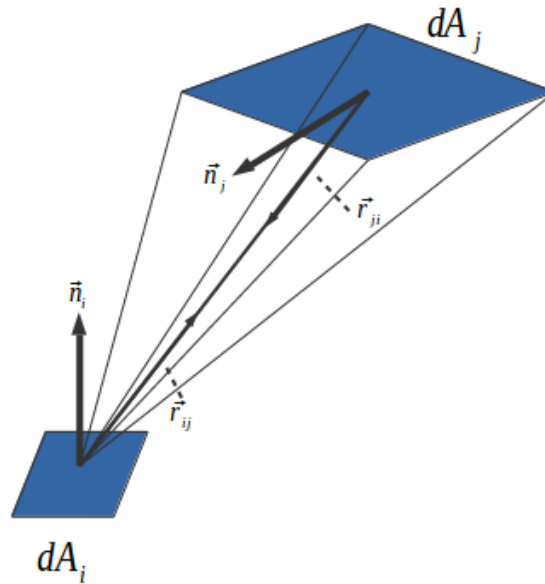
Figure 3.13: Single surface Radiosity modeling

where $\hat{n}_i$ is the normal of the illuminated surface, $\hat{r}_{ij}$ is the unit vector pointing from the illuminated surface to the center of the illuminating surface, $\hat{n}_j$ is the normal of the illuminating surface, and $\hat{r}_{ji}$ is the unit vector pointing from the illuminating surface to the center of the illuminated surface.

For scene modeling, the process is repeated for each facet.
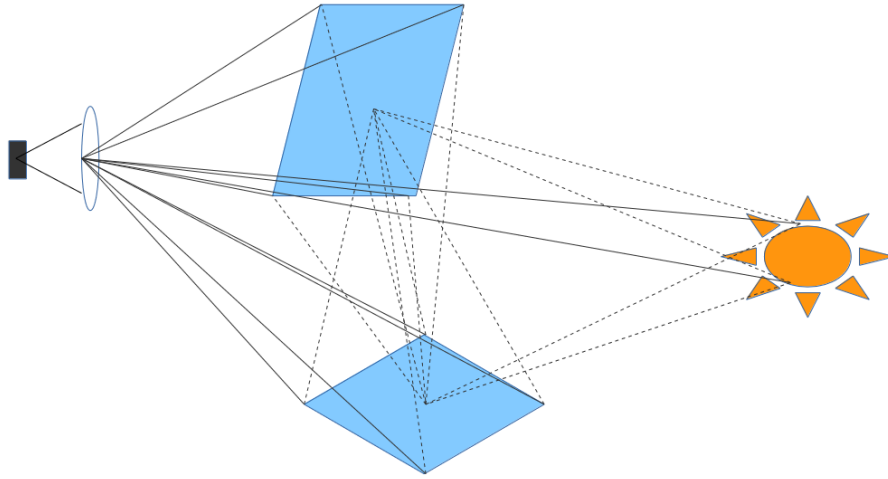
Figure 3.14: Multiple surface Radiosity modeling

Unlike in ray tracing, the only material property considered is a scale factor, all other considerations are purely geometric. While this is a major short coming, diffuse is a common, and in an many cases, representative approximation for materials. It may not be be a good approximation for the entire scene, but may serve as a useful tool for explore some geometric aspects.

## 3.4 DIRSIG

DIRSIG is a radiative transfer engine. A user develops a scene complete with: geometry, material properties, radiative transfer approximation, and motion; develops an imaging platform complete with: flight profile, orientation, and sensor(s) characteristics; creates an atmosphere accounting for: cloud cover, climate, time of year, and location on Earth; then implements a hybridized ray tracing scheme to simulate what said imaging system captures on its designated mission. This scenario development manifests itself as a series of input files which are feed into a succession of submodels. These models organize the scene, sample the geometry with ray tracing, calculate the respective radiative transfers, and then combine these with a sensor model to output a radiance image along with several truth images. This is illustrated in the subsequent flow chart [Fig: 3.15]. This overview is intended as a high level, even perfunctory introduction to the inner workings of DIRSIG. Some of the intricacies are glossed over with the larger concepts at hand. A deeper dive into the major components of DIRSIG can be found in *Schott et al* [9].
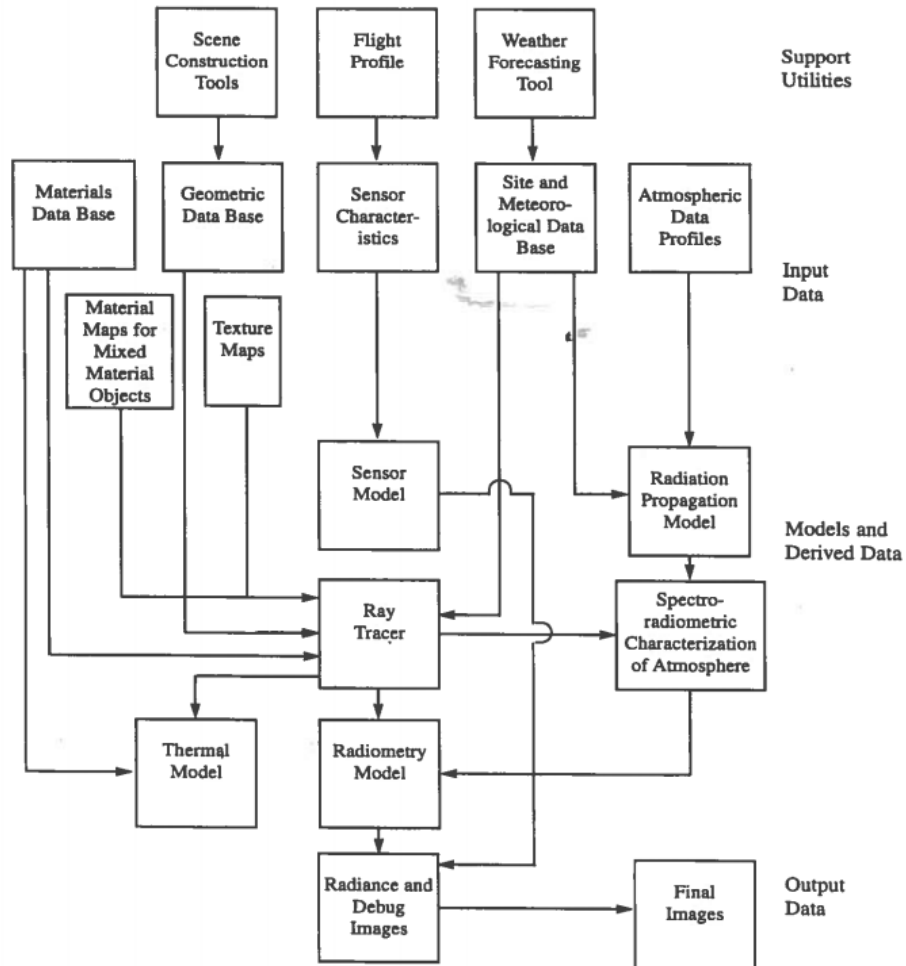
Figure 3.15: DIRSIG simplified flow chart

The ray tracer creates rays that pass from the focal point through the focal plane to projected pixel locations. Additional rays are then cast into the hemisphere above any sampled surfaces, and directly to the sun. The hemisphere sampling identifies potential shadowing and determines the potential downwell geometries to consider, while the solar ray gives us a measure of the incident radiation. The down-well is determined by taking the hemispheric sampling, and feeding the unimpeded ray geometry, along with the user defined atmospheric profile and geo-temporal information into the MODerate resolution atmospheric TRANsmission (MODTRAN) program [38]. This program does atmospheric propagation modeling, and allows the user to accurately account for the atmospheric effects.

28

Figure 3.16: DIRSIG single ray sampling example [4]

Once a ray intersects a facet with in the scene, a material database is called upon. This user defined material database scales the rays by how much the ray will be attenuated by the geometric transmission, reflections, absorption, and emission. Furthermore, texture maps and material maps are used to approximate more complex surface qualities or microfacets more efficiently then a facet by facet approach.

Each ray has the ultimate goal of filling in remote sensing's "BIG Equation" or at least a version of it to determine sensor reaching radiance. The Sensor reaching radiance modeled in DIRSIG derived by Schott [4] is given by:

$$
\begin{aligned}
L(r_{Obj-App}, \theta_r, \phi_r, \lambda) = & [\epsilon(\theta_r, \lambda) L_T(\lambda) + E'_S(\lambda)\tau_1(\lambda)\tau_{1p}(\lambda)cos(\sigma')\rho_{BRDF}(\lambda) + \\
& \int_{\phi_i=0}^{2\pi} \int_{\theta_i=0}^{\frac{\pi}{2}} L_d(\theta_i, \phi_i, \lambda)cos(\theta_i)\rho_{BRDF}(\lambda)sin(\theta_i)d\theta_i d\phi_i] \quad (3.20) \\
& \tau_2(r_{Obj-App}, \theta_r, \lambda)\tau_{2p}(\lambda) + L_u(r_{Obj-App}, \theta_r, \lambda) + L_p(\lambda)
\end{aligned}
$$

There is a lot to digest in this equation, and a variable by variable explanation may complicate the point so we will just look at the five terms the variables make up.

The first term is an accounting of the exitance from the thermal emission of the target, using a black body approximation with the estimated emissivity of the target. The second term is accounting for the reflected radiation from direct

solar illumination using the path geometry and transmission between the sun and the target, along with the reflective properties. The third term is an accounting of the downwell radiance from the light bouncing around the atmosphere. All of these terms make up the light being measured from the target and are all scaled by the same path transmission. The forth term is an accounting of the upwell term. This is all the light that is either being thermally emmitted or reflected from the atmosphere. The final term is the contribution of other in path objects, perhaps a partially transmissive cloud or window.

Once a the radiation incident onto the focal plane is determined, DIRSIG uses the sensor model to turn that into a simulated image. The radiance field image is first calculated,

$$L_i = \int L_\lambda R_i(\lambda) d\lambda. \tag{3.21}$$

where $R_i$ is the responsivity of the $ith$ element. Casacading Modulation Transfers Functions (MTFs) of the optics, detector, electronics, and platform and scan motions are used to create a system Point Spread Function (PSF). The final image pixel radiance is determined by a convolution of the system PSF and the radiance image.

# Chapter 4

# Framework for Simulating Earthshine Using DIRSIG

This chapter details the *under the hood* structure of our DIRSIG workflow.
Section 4.1 examines the structural geometry used as a foundation in DIRSIG.
Section 4.2 examines our work flow for creating an Earth object; from Imagery, to
IDL code, to Matlab code, to a DIRSIG Earth object. Finally, Section 4.3 examines
the level of ground truth we employ.

# 4.1  Setting Up a Geometric Foundation in DIRSIG

## 4.1.1  The ENU Coordinate System

DIRSIG operates under the assumption that the environment being simulated is
located on the Earth. For this reason, the coordinate system is defined relative to
an observer with a compass standing at a Latitudinal Longitudinal point on Earth.
The coordinate system used is known as East North Up (ENU) [Fig: 4.1]. This
coordinate system is a local Cartesian system, not spherical. Meaning $2\pi R_{Earth}$
units along the equator in the Eastern direction will not return us to the same
Location. All this leads to complications when the scene we seek to simulate is the
Earth, or has the Earth in it.
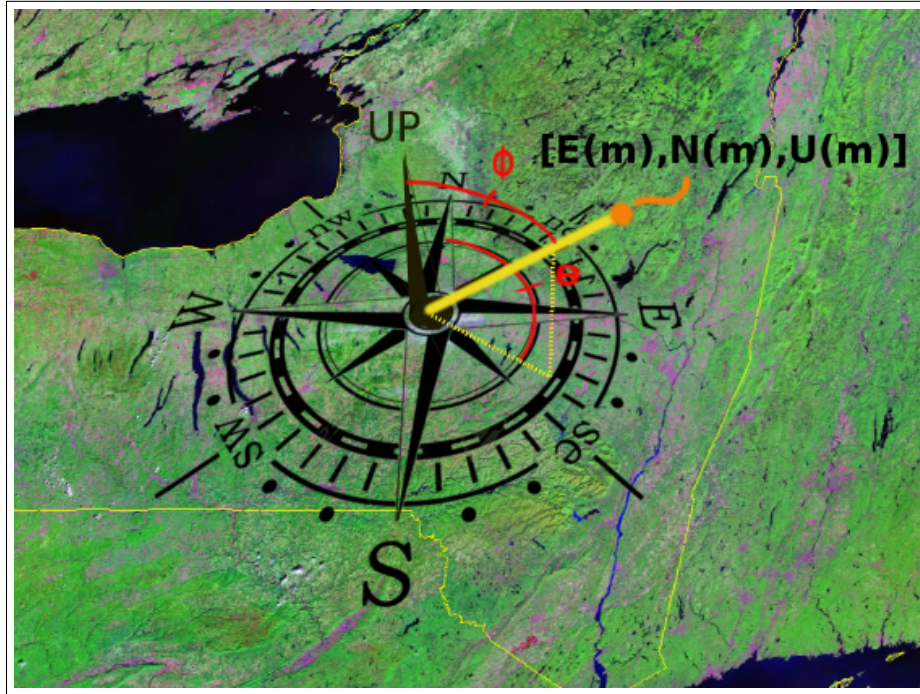
Figure 4.1: ENU convention

## 4.1.2 Object Database Geometry

There are two kinds of objects used in DIRSIG: DIRSIG built in base geometries, and imported Objects. Built in base geometries are characterized by the conventional characteristics of the object type in an Object DataBase (ODB) [Fig: 4.2]. We'll limit our scope to a sphere.

```
DIRSIG_ODB = 1.0

OBJECT{
    UNITS=METERS
OBJ_FILENAME=USSNimitzSplit.obj
INSTANCES{
        INFO=0,0,0,2,2,2,0,0,0
}
}

SPHERE {
   RADIUS = 100
   CENTER = 0,-300000,0
   MATERIAL_IDS = 12
}|
```

Figure 4.2: Sample ODB file

The sphere is comprised of three parameters: radius, center, and material
ID. The radius is the radius of the sphere given in meters. The center is the location
of the sphere center in our scene ENU coordinate system. The material ID is a
reference number for the material properties of the sphere. A sphere of radius 100m
and center [100,0,0] would appear as in our coordinated system as a shifted sphere
[Fig: 4.3].
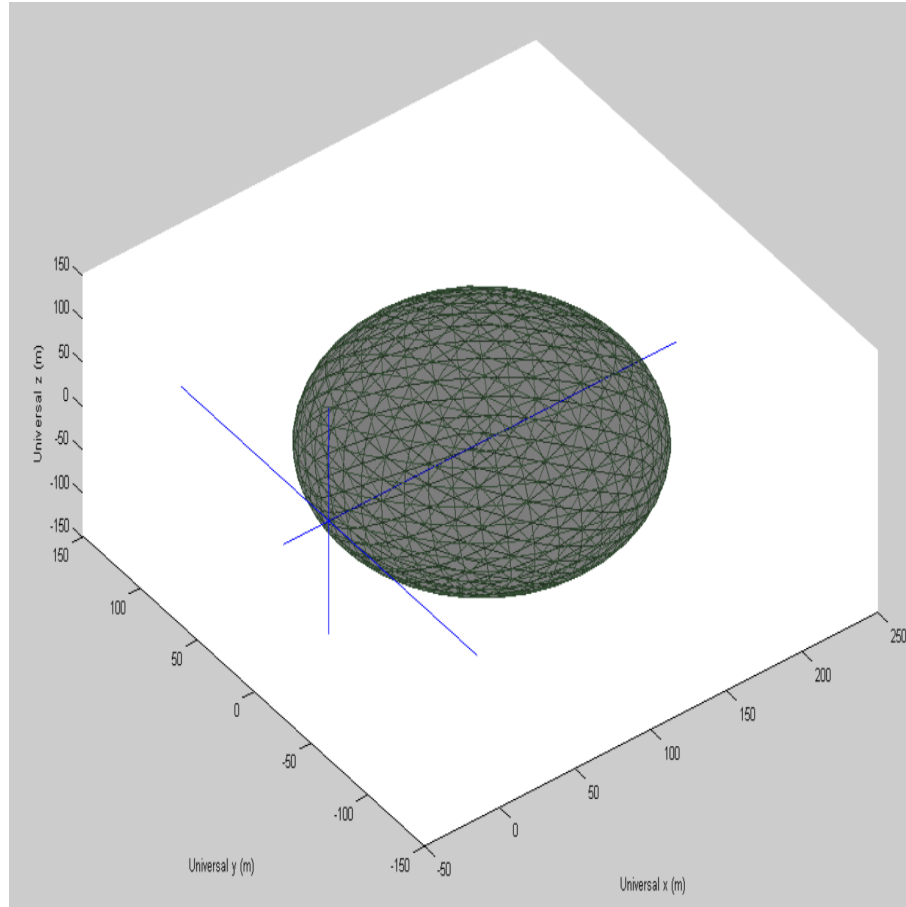
Figure 4.3: Matlab representation of a sphere shifted in the x direction in DIRSIG

The material ID can be either used to reference a material entry in a material database file or it can be used to reference an image representative of a property map. To reference a property map you must first reference a material entry with any material properties, it will be negated when the map is referenced. Next we go to the DIRSIG editor, enter the scene, and go to property maps. From there, the UV map is projected onto the sphere and the map's intensity values are mapped to their corresponding property values, in our case, their material ID [Fig: 4.4, 4.5].

(a) Enter Material reference number

(b) Determine Projection type - UV for sphere

(c) Image directory and digital count to material ID assignment
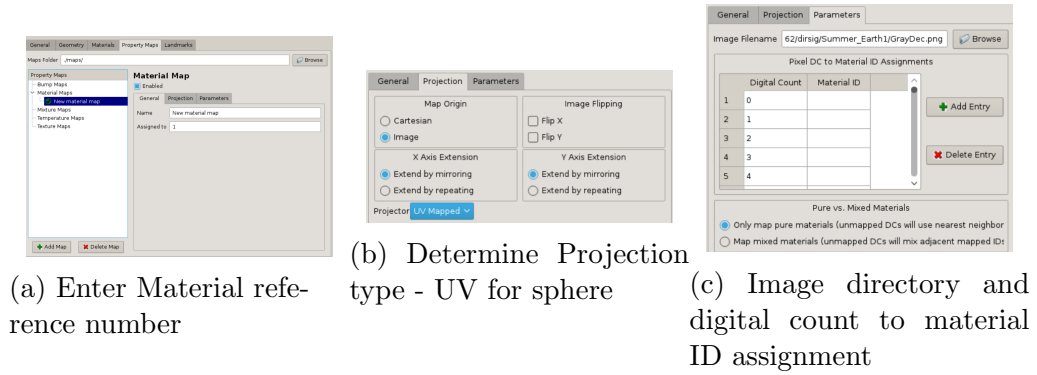
Figure 4.4: DIRSIG editor work flow to UV wrap a sphere.
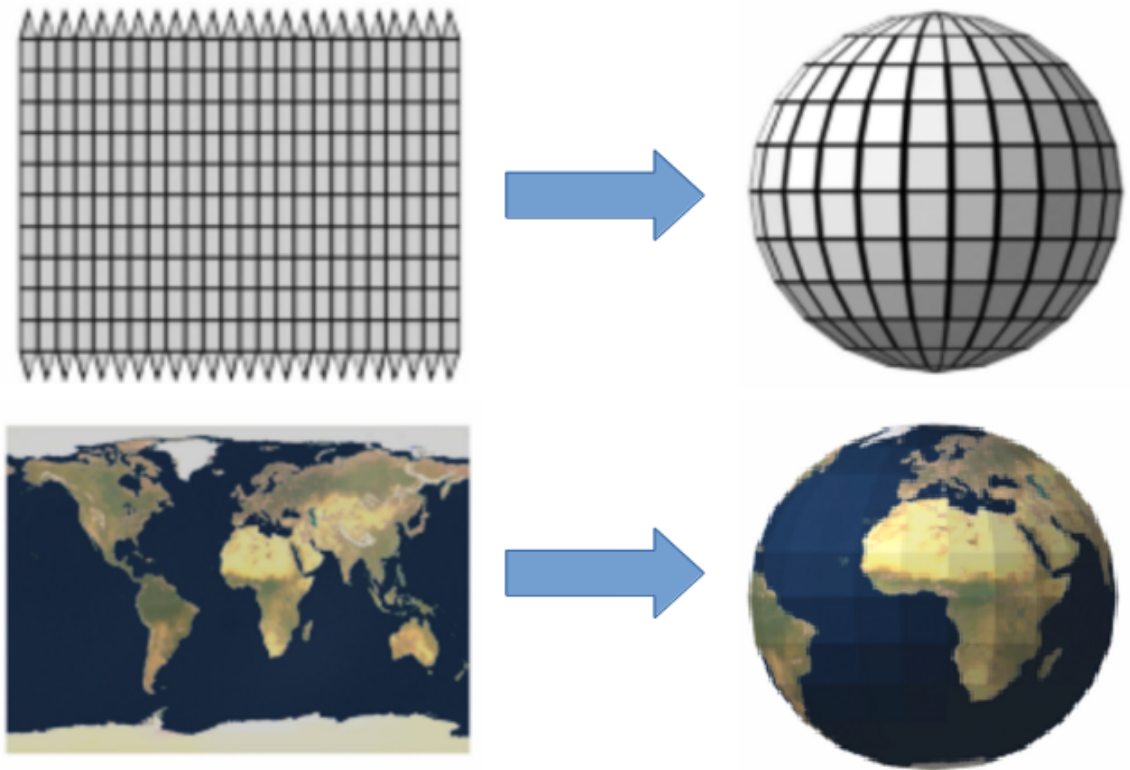


Figure 4.5: Representation of UV projection edited from Wikipedia images

Imported files have three parameters: units, filename, and instances. Units define the scale of the vertices [Fig: 4.2]. Filename is the path to find the object; this is simply the filename if it is in the same place as the primary simulation file. Instances are the parameters that detail how to manipulate the geometry of the objects and of the number of occurrence. Under instances, for each info followed by 9 numbers, an occurrence of that object will be added to the scene. The objects' local coordinate system will be centered at the Universal Cartesian [x,y,z] coordinate of the first three numbers. The objects will be scaled in the x, y, and z directions by the second three numbers. Lastly, the object will be rotated by the Euler angle convention about the local x, y, and z axis - first rotated about the z axis, then the y, and then the x.
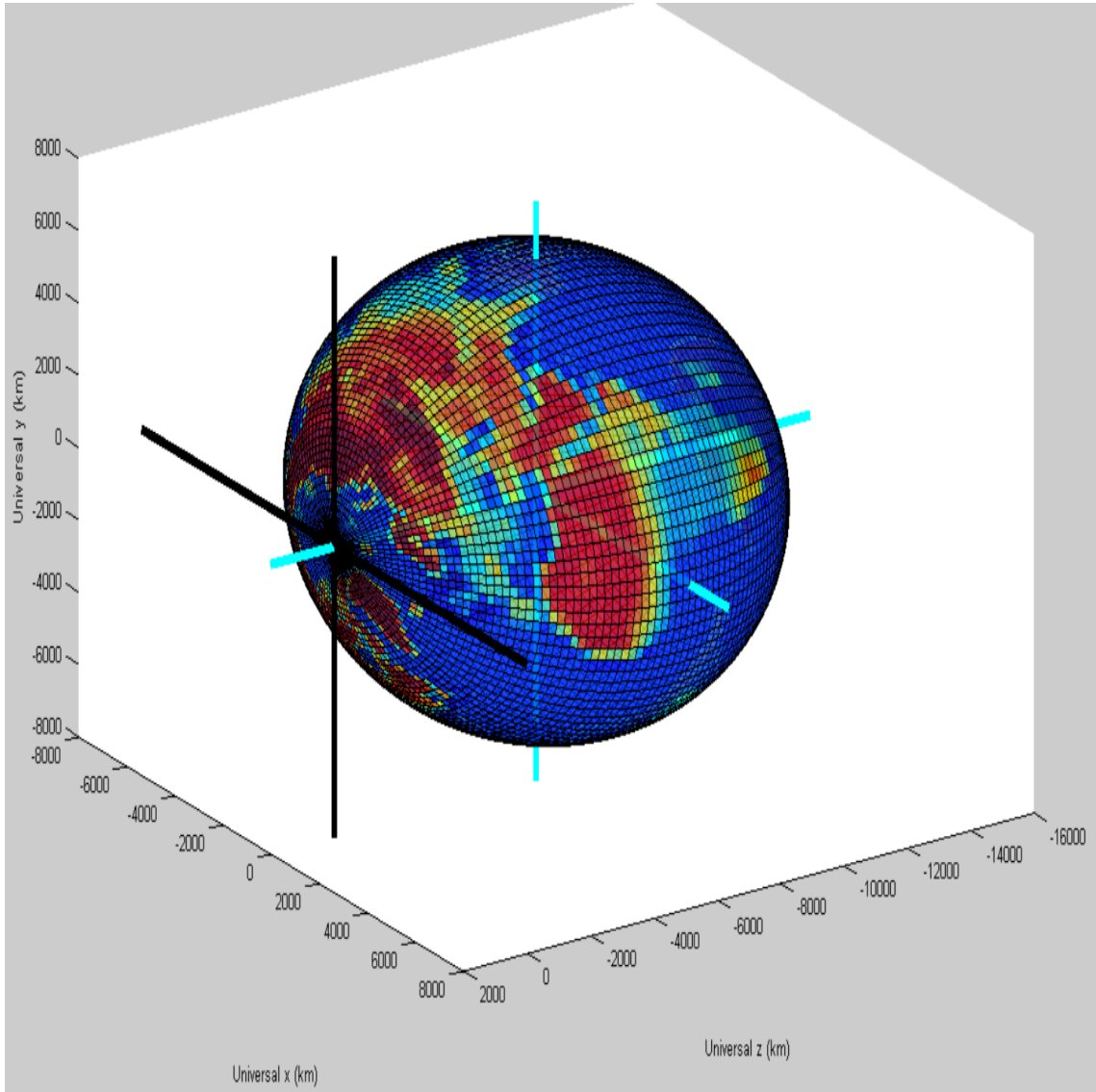
Figure 4.6: Matlab representation of mis-aligned ENU coordinate systems.

By wrapping a rectilinear map of the Earth around a sphere, we give it an orientation; the built in geometry assumes spherical symmetry, thus lacks parameters for orienting. DIRSIG allows for the filename to reference other ODB files, allowing for all the instance parameters to be applied. As mentioned above, DIRSIG uses ENU coordinates. To make future geometric references more intuitive, we want to align our Earth with the ENU system built into DIRSIG. If we set our object cen-

ter at [0,0,-6371000] and our latitude, longitude, and altitude, located in the scene
file, to [0,0,0], the origin would be located at [90,-90,0] on our Earth. Either this can
be taken into account when locating the solar illumination, other objects and our
imaging system, or we can use the instances rotation parameters to make the ENU
coordinates inherent to the Earth and global ENU coordinates align [Fig: 4.7]. The
instance parameters uses a local Cartesian coordinate system and requires a rotation
of [90,0,90]. We are prevented from simply making the altitude the negative of the
radius of the Earth by how DIRSIG deals with the atmosphere.
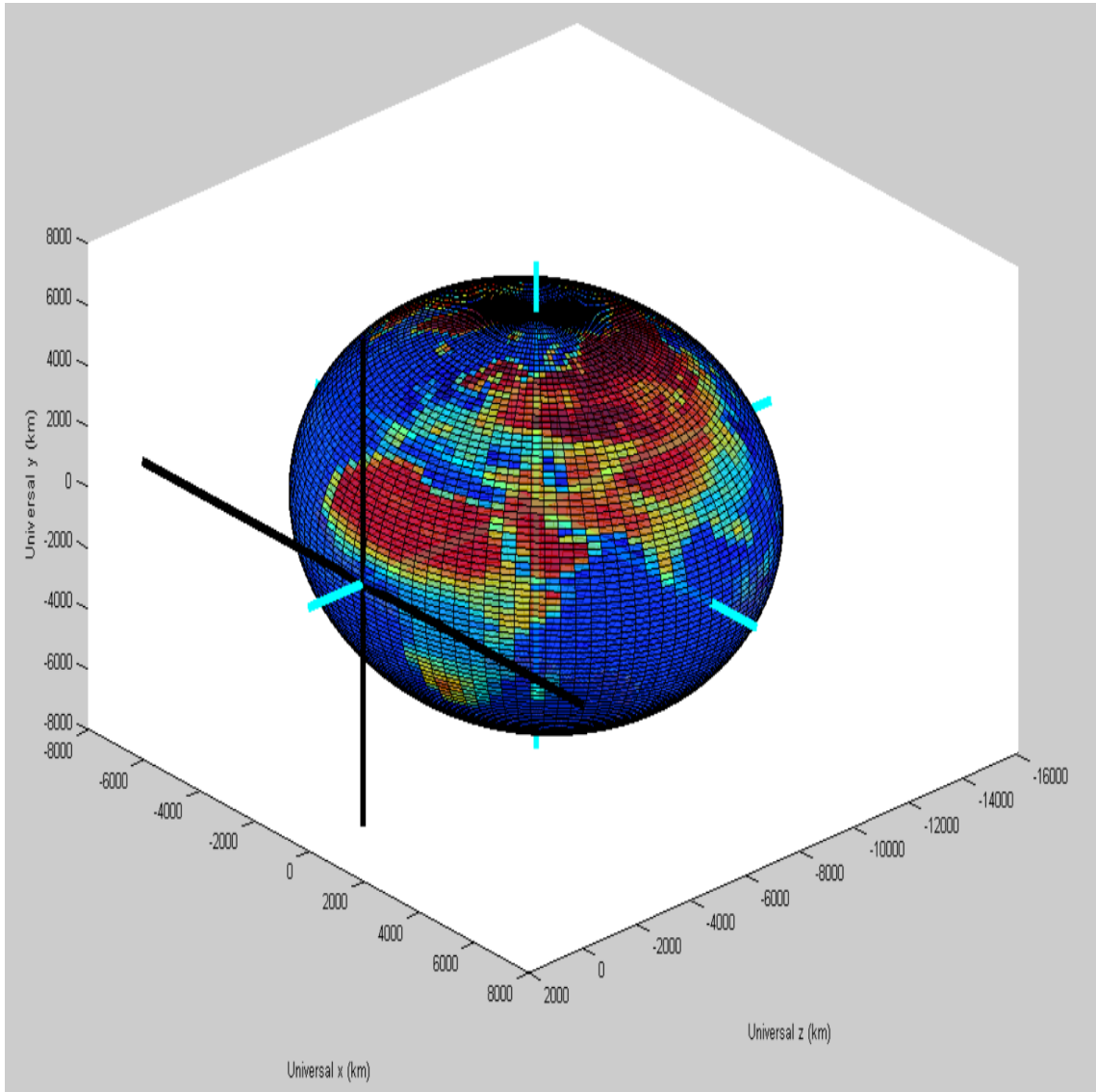
Figure 4.7: Matlab representation of aligned ENU coordinate system.

To add another object, namely a satellite or a geometric construct for later analysis, another object is added to the ODB file. The file name must now reference the object geometry. For our purposes, the new object will always be centered at [0,0,+z] [Fig: 4.9]. Changing geolocation or taking into account circular orbital information will all be accounted for using rotations of the Earth and solar illumination.
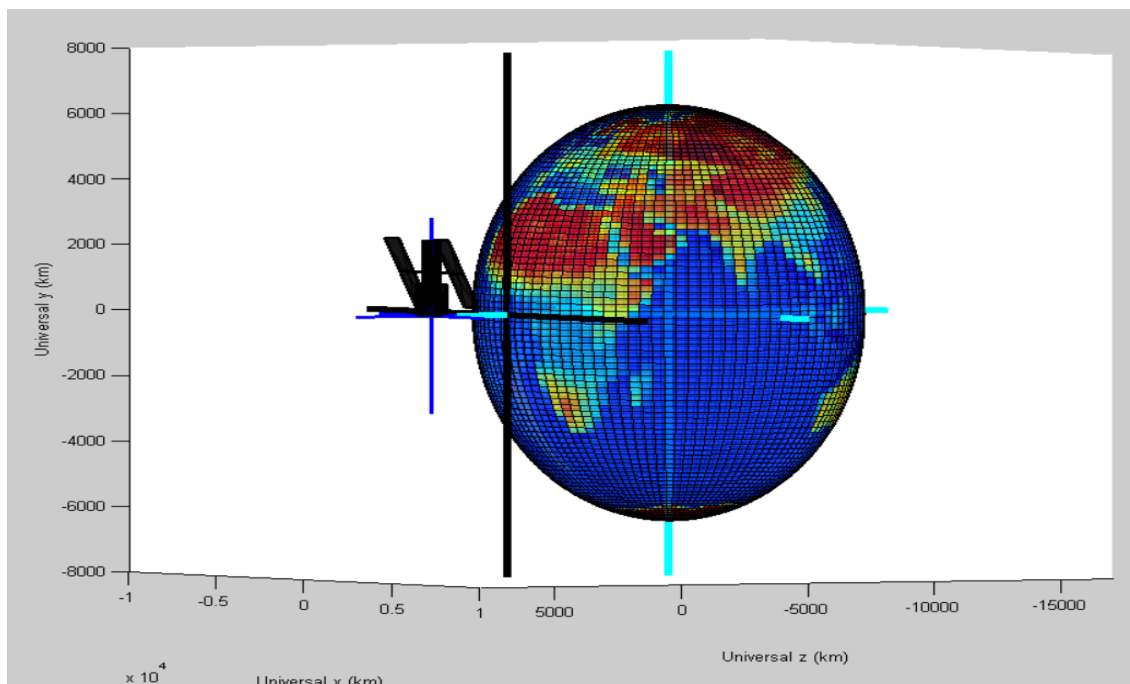
Figure 4.8: Matlab representation of an exaggerated satellite and Earth object con-
figuration.

Depending on how the coordinate system is defined in the .obj, rotations maybe
necessary in the INSTANCES.

### 4.1.3   Solar Irradiance

In DIRSIG there are two methods of identifying the direction of solar irradiance:
Date and time (found in .tasks), and solar azimuth ($\theta$) and zenith ($\phi$) [Fig: 4.1]
(found in .atm). To explore geometric relationships, the conventional solar angles
is the most intuitive, though those are returned if one chooses to use the date and
time. For our purposes we will use the solar angles, which negate any date and
time entry. An entry of [0,0] for the solar angle corresponds to a direction vector of
[0,0,1] in ENU coordinates. An entry of [a,b] corresponds to a rotation of 'a' about
the Up-Down axis in the direction of East 'a' degrees and a rotation about the E-W
axis in the direction of North 'b' degrees.
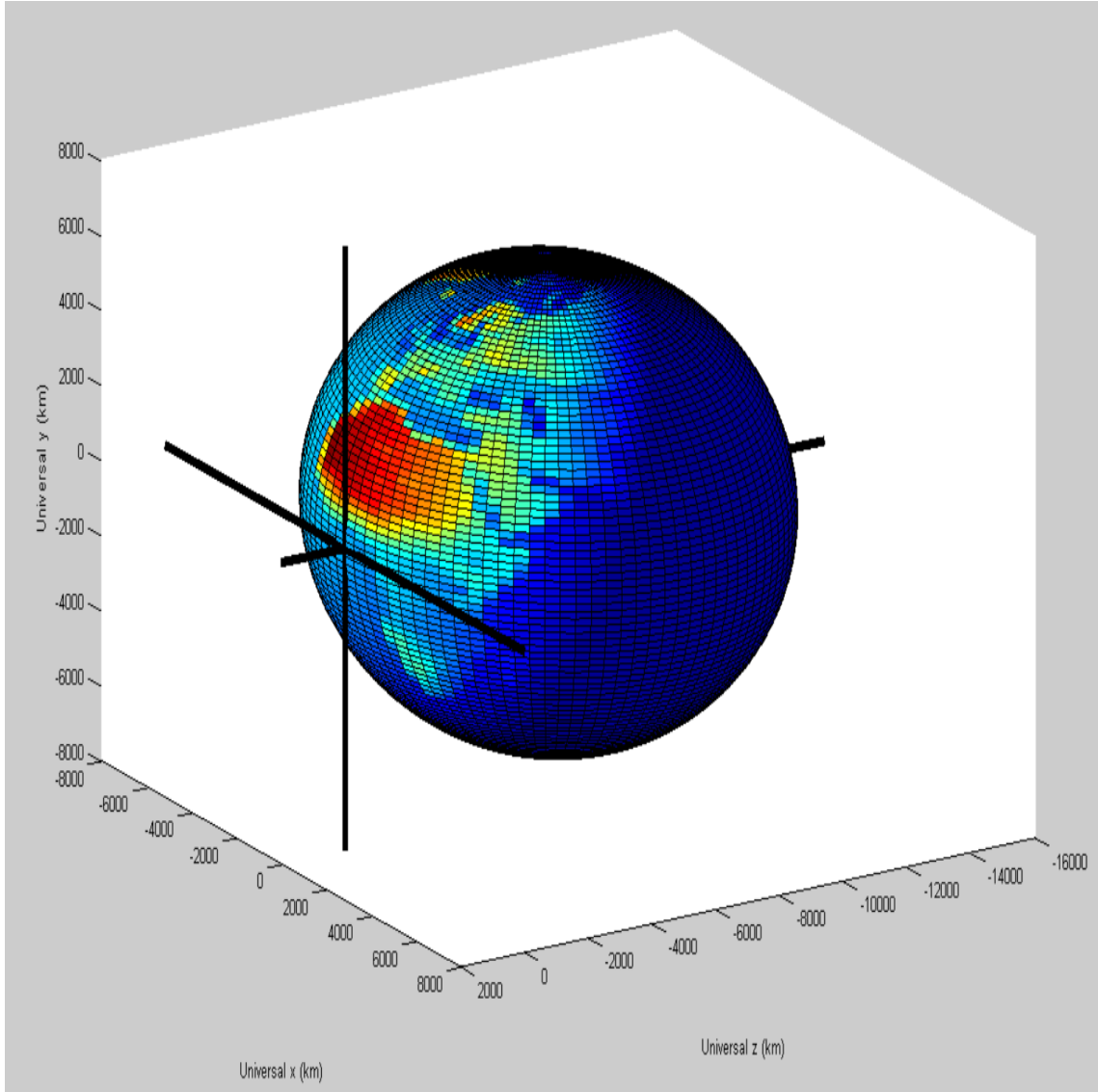
Figure 4.9: Matlab representation early summer Earth illumination

## 4.1.4   Imaging Geometry

There are two geometric considerations to be taken into account: the spatial ge-
ometry of the platform relative the scene and the optical geometry of the imaging
system. The geometry of the image will depend upon the marriage of these two ge-
ometries. The spatial geometry of the platform is defined similar to how we defined

our scene location, with the difference that the Imaging system has a predefined orientation and that orientation is with the aperture of the imaging system pointing in the [0,0,-1] direction. The platform location can be changed relative to our ENU coordinate system (found in .ppd). The orientation can be changed either by rotating the platform (found in .ppd) or by changing the location of the imaging system on the platform (found in .platform), both with the same Euler-angle convention used in the INSTANCES of the objects.

The GSD tells us how much area of our scene is mapped to a single pixel. The idealized GSD is calculated by:

$$GSD_{Ideal} = \frac{P * Alt}{fl}$$

where P is the pitch, the width of a pixel, Alt if the altitude and refers to the separations between the scene's origin, and fl is the Focal Length of the imaging system. The FOV is the angular field of view and refers to the angle subtended by the instruments field of view in a direction. The Idealized FOV is calculated by:

$$FOV_{Ideal} = \frac{GSD_{Ideal} * N_{Pixels}}{Alt}$$

where $N_{pixels}$ is the number of pixels on the array in the plane of the angle.

## 4.2 Three Layer DIRSIG Earth Object Approximation Workflow

Now that we have a geometric foundation, our goal is to attribute our geometry with material properties to create a time sensitive reflectance model of the Earth. To do this we break the Earth into three distinct shell objects: Earth's surface material shell, cloud material shell , and the atmosphere material shell. The shells are generated from three data products. The first two layers are derived using MODIS products, the MCD43A1 global surface BRDF map and MOD06 global fractional cloud map. This enables us to build a two layer Earth object. We then simulate EPIC Imagery. An ELM comparison is done between the simulated and actual EPIC imagery to determine a homogeneous third shell - our atmosphere. This section will explore in further detail the underlying physics and programmatics of the process which we utilized to approximate the Earth as a three layer DIRSIG object. For this section, flow charts will representing the pseudo-code are used.
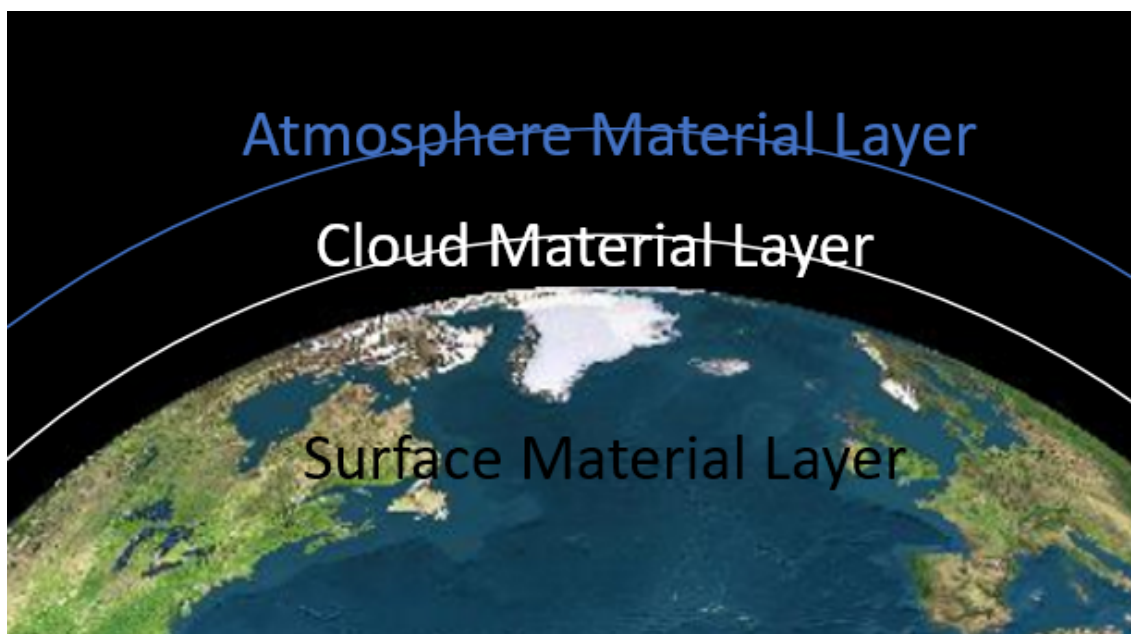


Figure 4.10: Representation of three layered Earth Object
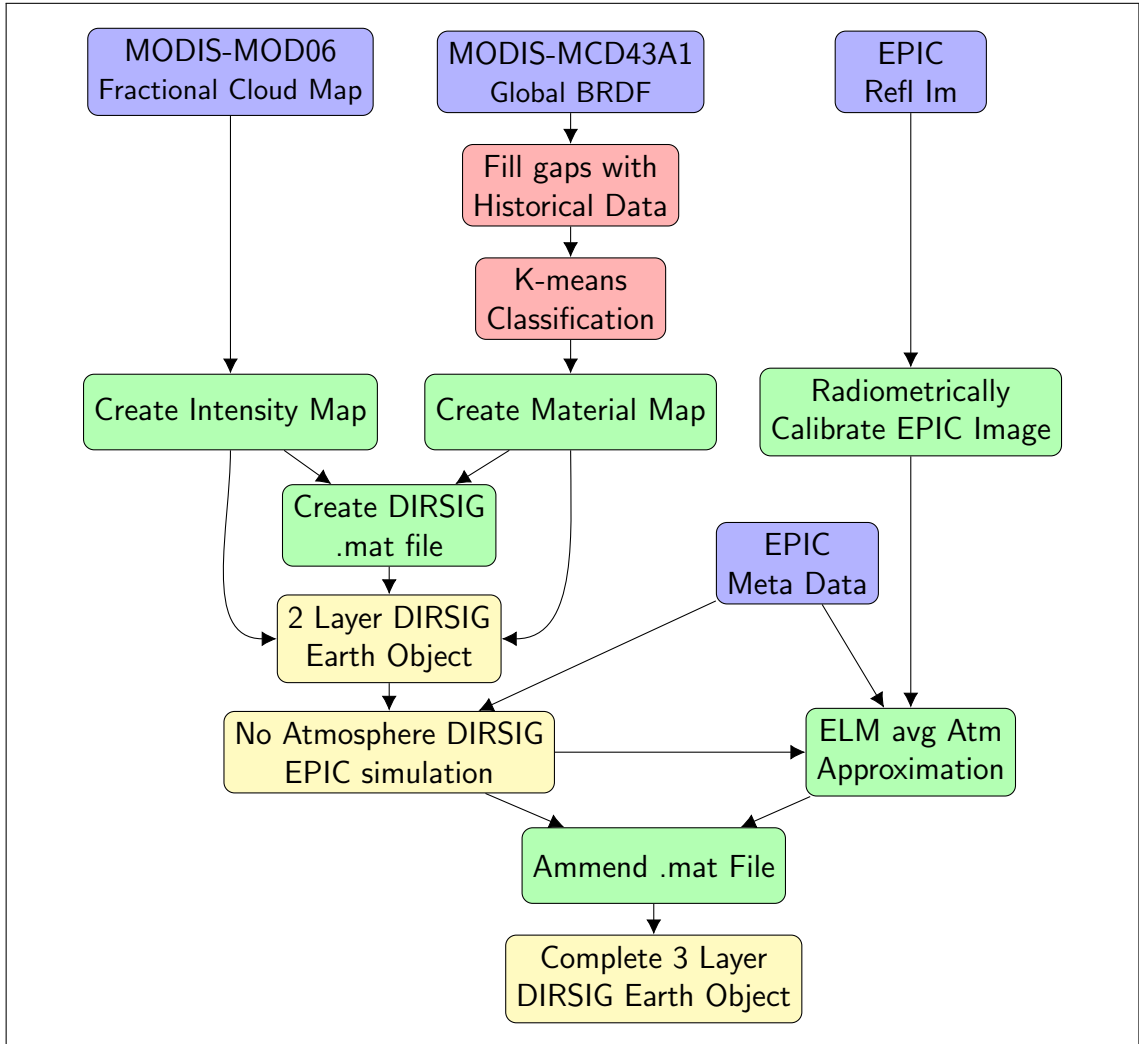
Figure 4.11: Flow chart for approximating the Earth as a three layer DIRSIG Object. Purple represents the input data, red represents the work done in IDL, green represents the work done in Matlab, and yellow represents the work done in DIRSIG.

## 4.2.1 The Imagery

There are two satellite platforms which we rely on to build our Earth object: The MOderate Resolution Imaging Spectrometer (MODIS), and the Earth Panchromatic Imaging Camera (EPIC).

MODIS is a payload built into the Terra and Aqua, sun-synchronous, near polar, circular orbiting satellites. It has a geographic revisit time of 1-2 days, with a GSD ranging from 250m to 1000m, and a spectral coverage of 36 bands ranging from 400 to 14,000nm; 16 of which ranging from 400nm to 1000nm (our regime of interest). All of this make the MODIS platform an ideal system to analyze the changing reflectance of the Earth. Furthermore, NASA has done some post processing of the Imagery into Data sets easily capitalized upon for the purposes of Earth reflectance modeling.

The two MODIS post processed data sets we use are the MCD43A1 Global Ross-Li BRDF parameter map [Fig: 4.12], and the MOD06 8day averaged fractional cloud map [Fig: 4.13]. MCD43A1 provides the weighting parameters associative with the Ross Thick Li Sparse Reciprocal (RossLi) BRDF Model [Eq:3.17] for each of it's spectral bands for the entire surface of the Earth with an equatorial resolution of 500mx500m and an 8day temporal recalculate frequency. Given a location on the Earth and any solar incident angle, the fraction of the light reflected in a given direction is well approximated. The MOD06 cloud map gives the fractional cloud cover for every point on the Earth, with an equatorial resolution of approximately 1kmx1km. Using what we know about the clouds, a BRDF and transmittance can be simply applied. While these two data sets do a good job approximating most the Earth, the RossLi parameters are unable to account for water. In our treatment the water is set to a WardBRDF determined using the methods explored in Cox et al. [39].
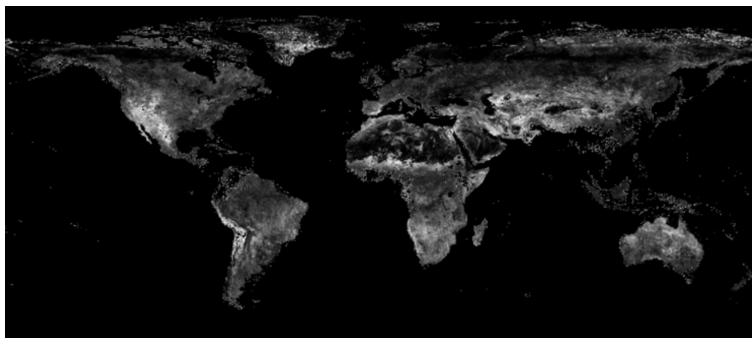
Figure 4.12: The diffuse parameter of a mid July MCD43A1 parameter map
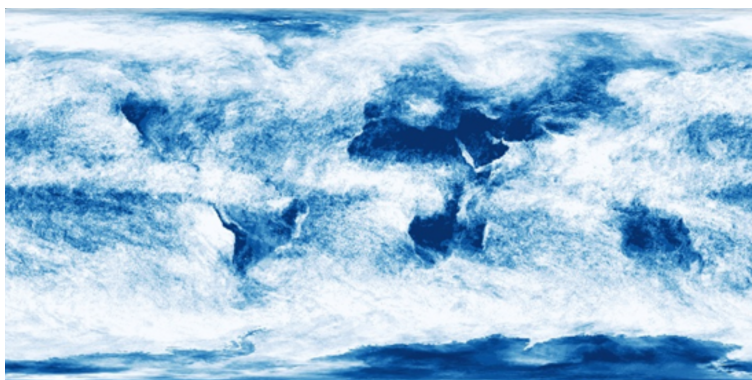


Figure 4.13: Example MOD06 fractional cloud map.

EPIC is a system aboard the DSCOVR satellite, located at L1 in Earth's orbital profile around the sun [4.14]. This enables it to have a unique sun-synchronous orbit where it is always facing the sun illuminated side of the Earth - creating multi view images of the entire Earth in under 24 hours. EPIC is a 10 band system, with spectral coverage from 317nm to 780nm. It's GSD in the center of the Earth is 15km and falls off towards the edges. This poor resolution makes it potentially a unsuitable source for direct reflectance measurements of the Earth, but a great source for temporal and spectral ground truth, and as we use it, as a means of approximating the atmosphere.

Figure 4.14: Example EPIC imagery with moon crossing path. [**?**]

While these platforms and their associated data products are a great source
of data for our analysis, their provided forms do not quite conform to our work
flow. MCD43A1 gives us a global parameter map, and in order to make that work
in the confines of DIRSIG, we would need to make a material for every unique
combination of parameters. It also leaves gaps where the RossLi parameters trying
to be derived was using data with cloud coverage. MOD06 has a smearing effect from
the multi-day averaging of the clouds and their movements. And current available
Epic imagery is not calibrated.

## 4.2.2   Processing Data Products

As previously explored, our data are representative of the global reflectance of the
Earth, but we need to get it into a format that allows for it to be used in DIRSIG.
This section will concisely analyze the process of taking each of the data sets into
a format which conforms to DIRSIG. We may seem to jump around, but the order
presented here is the order in which the user is expected to execute the processing.

### *Filling in the gaps in MCD43A1*

The 8 day MCD43A1 RossLi parameter maps are derived using the the data of the past 16 days. If too many of those images contain clouds, then the associated pixel defaults to a null value. It is possible that a day may not have enough data within the 16 day period to derive a surface reflectance, but the actual date of interest is cloud free, perhaps 7 days after the last derived map. To get the best data we can, we cycle through old imagery until every pixel of the parameter map is filled with the most resent RossLi parameters available, utilizing the capabilities of IDL to efficiently download and parse images of different formats and then output them in the desired format.
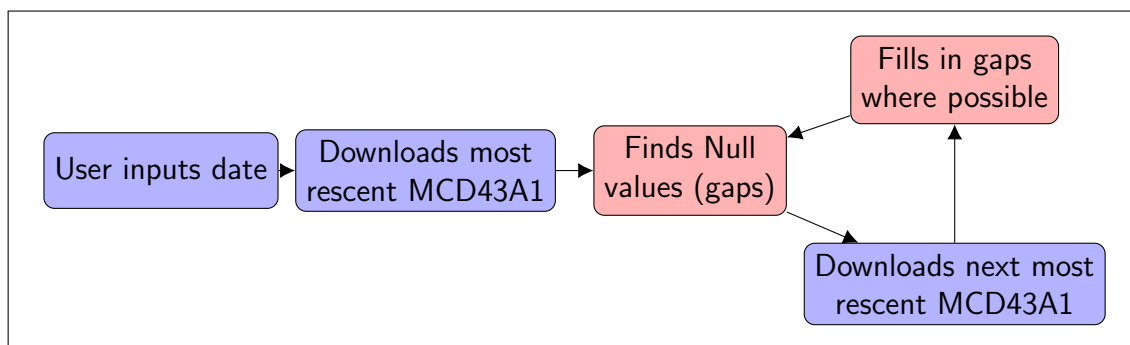


Figure 4.15: Flow chart for process of attaining a complete surface reflectance map of the Earth. Purple represents the input data. Red represents IDL code

While this is not temporally exact, for the most part it is an alright approximation. The change in surface reflectance, setting aside large derivate weather events, is temporally slow.

### *Biome Classification*

DIRSIG is unable to use an entire parameter map. Instead, a finite number of materials must be defined. To do this we use the built in K-means classifier of IDL/ENVI. K-means works by clustering data that is in close proximity with in space: be it physical space or attribute space; In our case we are concerned with physical and RossLi parameter intensity space. These classified areas serve as time sensitive biome identifies; we know Northern NY may be a temperate forest, but

spectrally it can easily look like Tundra. The number of Classes (Biomes), Iterations, and threshold are entirely up to the user. Also at this time, binning is done for those who desire a less resolute map. This makes for faster processing of the subsequent steps in our flow. The result is a gray value image of N possible intensities, where N is the number of identified classes.
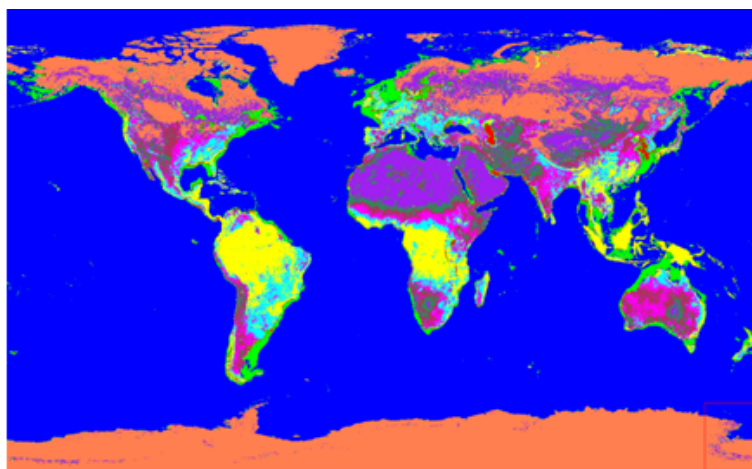


Figure 4.16: Global biome class image

### Create a Material Map

Once we have created our class image and our gapless parameter map, we are able to put them into our matlab work flow which creates a DIRSIG digestible material map and material database. The first thing we do is create a matrix of the average of every parameters within each class so that there is one set of Ross-Li parameters for each wavelength of each class. Now there is another kind of pixel type left null in the MODIS parameter map aside from consistently cloud obscured pixels - water. RossLi parameters do not do a approximate specular or glossy materials well. For that reason we artificially create another class for the remaining null pixels. Next, we turn the class map into a gray valued image of equal spaced 8-bit intensities based on the number of classes.
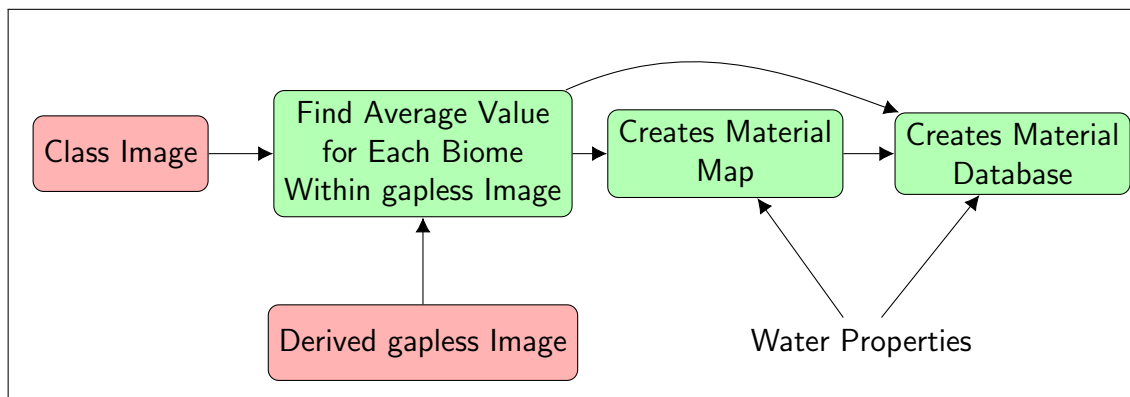
Figure 4.17: Flow chart for the process of creating a material maps and a material
data base for the first shell of our model. Red represents IDL code, green represents
Matlab, and nothing means derived.

Once we have our 8-bit intensity image, we can generate a material database
(.mat), relating class image intensity to $\lambda$ dependent RossLi parameters, and in the
case of the water, a predefined wardBRDF. These will later be used to attribute
surface reflectance properties to the most inner shell of our Earth Object.

**Fractional Cloud Map**
Intensity material maps work differently then normal material maps. Their
values are considered to be on a continuous BRDF spectrum between the material
attributed to the lowest intensity value, to the material attributed to the highest
intensity value. The cloud intensity map, in its current work flow iteration is pretty
straight forward to make. The fractional cloud map can be downloaded as a rec-
tilinear Lat/Lon image, with intensities that correspond to the fraction of cloud
coverage in the sampled area. While our work flow enables a user to rebin the image
for processing expediency, it can also be downloaded at different resolutions, and
either way is not entirely necessary. The resulting image is our intensity material
map for the cloud layer. The material database when constructed in the previous
section automatically includes the diffuse cloud values derived from a completely
cloudy MODTRAN run, and the inversely proportional transmission. These will
later be used to attribute surface reflectance properties to our second shell layer of
our Earth Object.

*Radiometrically Calibrating EPIC*

Unfortunately, EPIC is not as established or high profile of a system as MODIS, which means updates and data products are slow to be released. For the first year of this research we were only able to attain uncalibrated 8bit RGB imagery. With the hopes that future data product would be soon released, we worked them into our flow. Eventually the full 10 band raw data was released, but to date no calibrated data has been released. This left us with a need to calibrate the data on our own. There are three things we hope to do with the EPIC system: 1 - use the EPIC meta data to determine system and scene parameters so that we can simulate EPIC imagery, 2 -compare the simulated 2 layer imagery of the Earth Object with the actual imagery of EPIC to determine a homogeneous Atmosphere Model, and 3 - Use EPIC as ground truth to determine the near bistatic viability of our model.
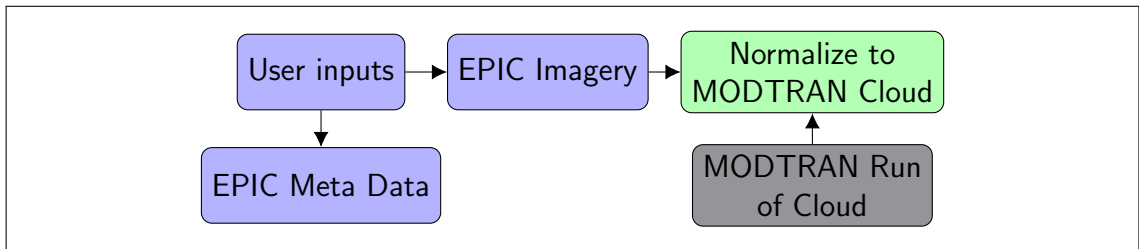


Figure 4.18: Flow chart for the process of creating a radiometrically calibrated EPIC image. Purple represents input data, green represent Matlab, and gray represents MODTRAN

Given a date and time, our code collects all of the associated meta data of interests and the most time relevant imagery. The imagery is then maximum normalized to a MODTRAN full cloud run.

## 4.2.3 Completing the Three Layered Earth Object

We now seek to determine a homogeneous approximation for the entirety of the atmosphere. Using our two derived inner shell material maps and our material data base, we follow the process alluded to in the first section of this chapter and wrap 2 spheres, squashed along their polar axis by the ratio of the two extremes

of the Earth's radius. One with the radius equal to the equatorial radius of the
Earth - wrapped with the surface reflectance material map, and another with the
radius equal to equatorial radius of the Earth plus 8 km (a rough average for cloud
height) - wrapped with the fractional cloud intensity material map. Together with
the material database, the second layer Earth scene is defined.
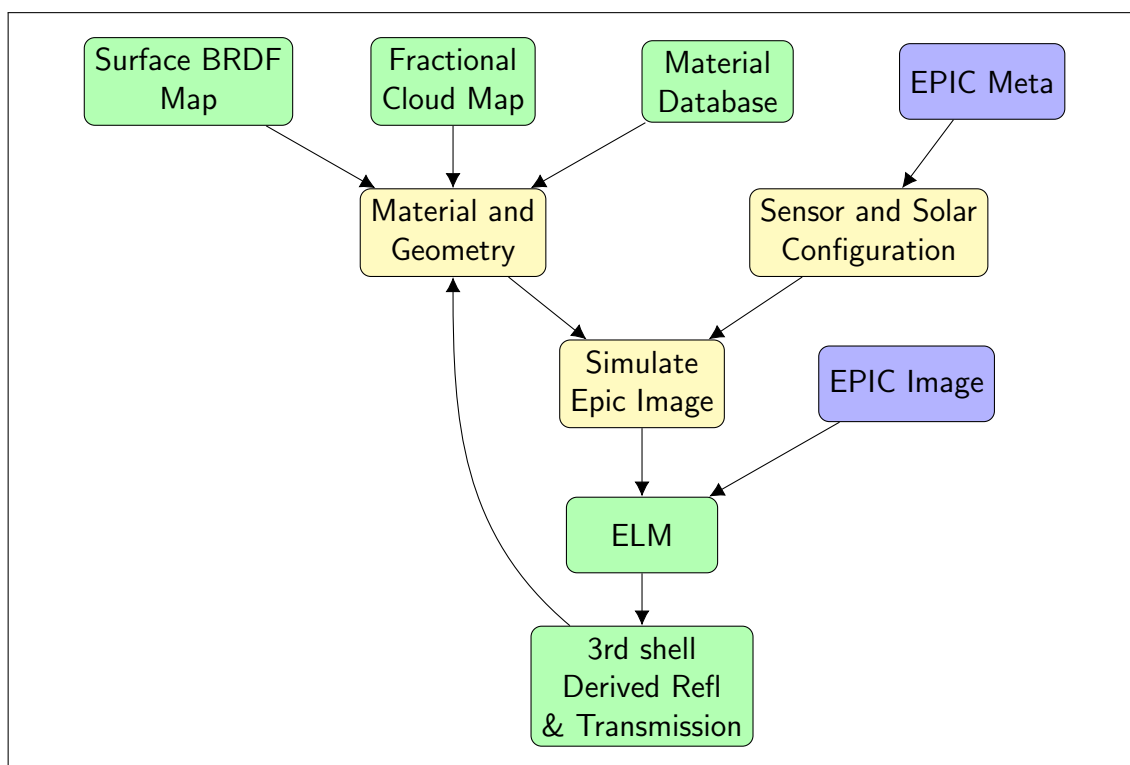


Figure 4.19: Flow chart for the process of creating a radiometrically calibrated EPIC
image. Purple represents input data, green represent Matlab, and gray represents
MODTRAN

The EPIC meta data is feed into the sensor and solar profiles, embedded in
the sensor characteristics and atmosphere data profiles alluded to in the flow chart
of the DIRSIG Theory section. This makes the FOV, sensor, and incident solar
radiation of the simulation match that of a desired EPIC image. We now simulate

an image of an atmosphere free Earth taken from the EPIC imaging system aboard
the DSCOVR satellite. This is to be used in conjunction with the actual EPIC
imagery to determine the radiance discrepancy, and from that determine material
properties for the atmosphere.

DIRSIG, in its current iteration, is unable to account for internal reflections
and absorptions of a medium. There are two ways we can get around this. Either
we may create multiple shells with surface properties that approximate our medium,
or we can do our best with one shell. Since each layer compounds the processing
time. We seek to approximate the atmosphere as one shell with surface properties
representative to the internal effects of the atmosphere medium. Fortunately, the
transmission is calculated by measuring the distance between the surface of the
intersecting shell and the next surface.

For a basic approximation of the atmosphere, we are going to need to
know three things: upwell radiance ($L_{UP}$), transmission ($\tau_{atm}$), and the extinction
coefficient ($\delta_{atm}$) for each of the bands. To do this, we use a hybridized Empirical
Line Method (ELM) between the known ground radiance of a few sample spots of
our simulations, compared to the EPIC imagery. Now what is hybridized about our
ELM is that, unlike a traditional ELM where a flat Earth and thus uniformly thick
atmosphere is assumed [4.1], we have to take into account the curvature of the Earth
or correspondingly the angle of off normal angle of the extant ray being measured
[4.2].

$$L_{measured} = L_{actual} * \tau_{atm}^2 + L_{UP} \tag{4.1}$$

where $L_{measured}$ is the measured radiance and $L_{actual}$ is the actual radiance emanating
from the surface of the Earth.

$$L_{EP} = L_{DIR} * \tau_{atm}^2 cos\theta + \frac{L_{UP}}{cos\theta} \tag{4.2}$$

where $L_{EP}$ is the measured radiance from the EPIC imagery, $L_{DIR}$ is the radiance
simulated from our two layered Earth object in DIRSIG, and $\theta$ is the angle of
incidence.

Because EPIC is $\approx 1,600,000 km$ away from the Earth, we can treat all of
the rays entering the imaging system as parallel [4.20].
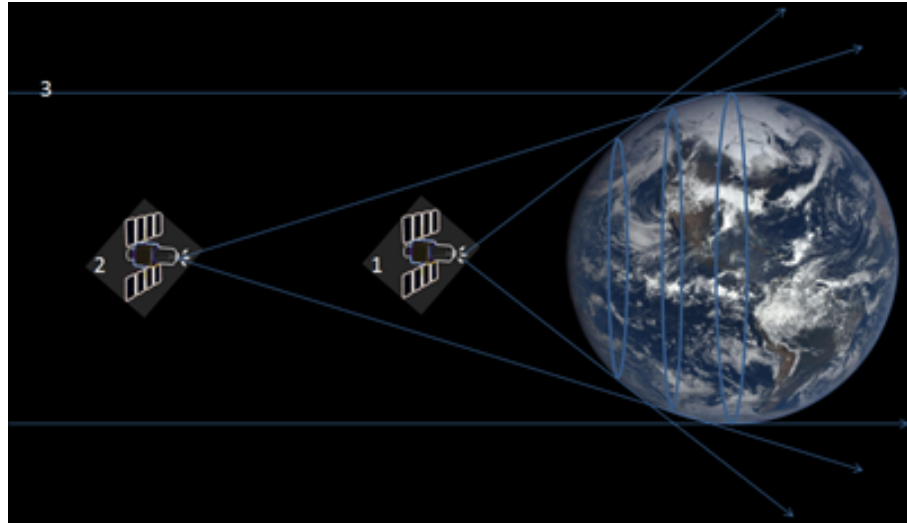
Figure 4.20: Representation of orthographic criteria

This enables us to treat the projection onto the focal plane as an orthographic
projection, and map the Earth's rectilinear coordinates onto the the image [Fig:
4.21]. Or conversly, map the image onto rectilinear coordinates [Fig: 4.27]
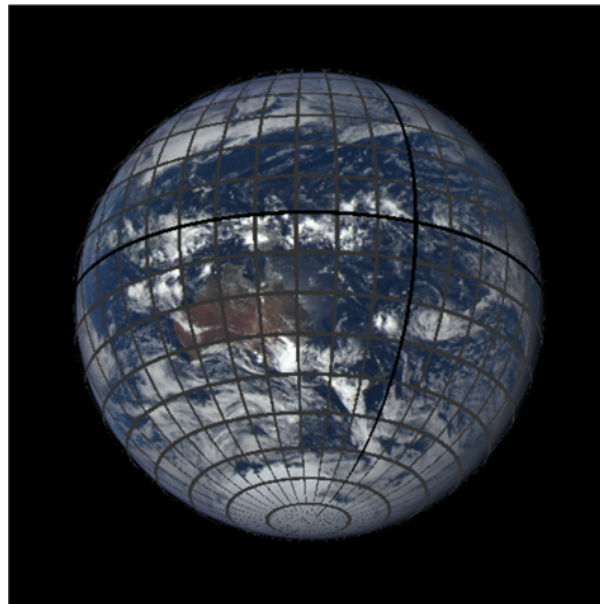


Figure 4.21: Lat/Lon orthographicly projected onto Earth image.
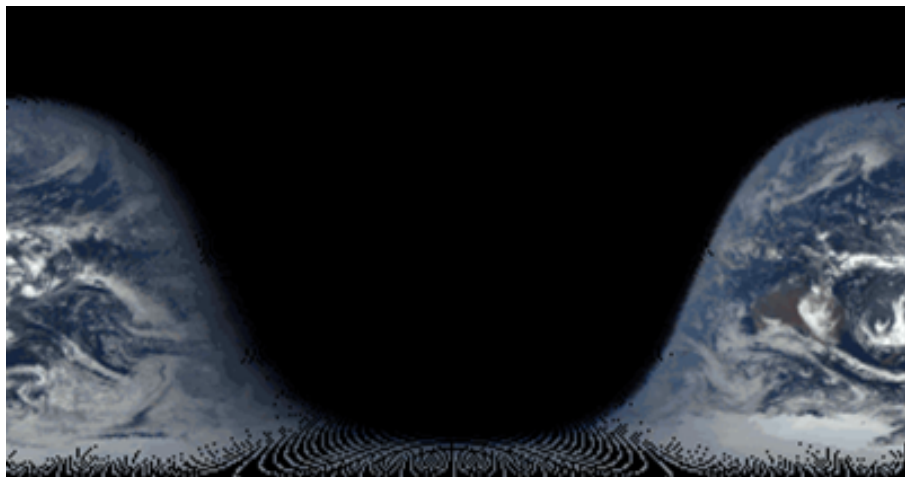
Figure 4.22: Earth image projected onto rectilinear Lat/Lon.

Once we have done this with both our images we need to determine some sample spots so we may set up a system of equations to solve for our unknowns. Because we are taking into account the difference in atmosphere thickness and we suspect it is close to homogeneous, the pixels do not have to match up perfectly between images, they just need to be the same material. Our approach is to sample several off nadir dark ocean pixels and several bright desert or cloud pixels in each image. Then we solve [Eq: 4.2], the over determined system for $\tau_{atm}$[Eq: 4.3] and $L_{UP}$ [Eq: 4.4.

$$\tau_{atm} = \sqrt{\frac{1}{L_{DIR}}(\frac{L_{EP}}{cos\theta} - \frac{L_{UP}}{cos^2\theta})} \tag{4.3}$$

$$L_{UP} = (L_{EP} - L_{DIR}\tau^2 cos\theta)cos\theta \tag{4.4}$$

After solving for $\tau$, if we assume that energy is conserved, we can solve for the extinction coefficient [Eq: 4.5].

$$\delta = \frac{-log(\tau)}{\Delta r} \tag{4.5}$$

where $\Delta r$ is the depth of the proposed atmosphere layer.

To fit an actual reflection model, we again turned to RossLi, this is because the RossLi model is the most robust model available to the DIRSIG user - able to approximate a wide variety of BRDF types. From the center to the outside edge of the Earth, the trend is that more and more light is being reflected by the atmosphere. When we get to the very edge (limb) of the Earth, the amount of light reflected should jump up dramatically because the thickness of the atmosphere from

the perspective of the observe doubles instantly, and then falls off. We can simply interpolate RossLi parameters to fit our atmospheric shell, but through interpolation it is really difficult to represent the edge effects. So some educated parameters are chosen by hand, and then put back into the feed back loop illustrated in the flow chart above, until the atmospheric shell is refined.

At face value, this method appeared to give us an atmospheric approximation that geometrically behaved well when compared to our ground truth imagery. Unfortunately, as we explored more obtuse SOO phase and got closer to our atmosphere, the parameters used to account for the increase towards the limb of the Earth contributed to an overly bright Earthshine component. In the face of this, we scrapped our RossLi atmosphere reflectance approximation. Several other things were tried, including using a very high temperature atmosphere with a very low emissivity, but ultimately went with no consideration for the atmospheric reflection of the Earth. This coupled with a decrease in height of the atmosphere (resulting in a decrease in optical depth), enabled a radiometrically consistent Earth object.
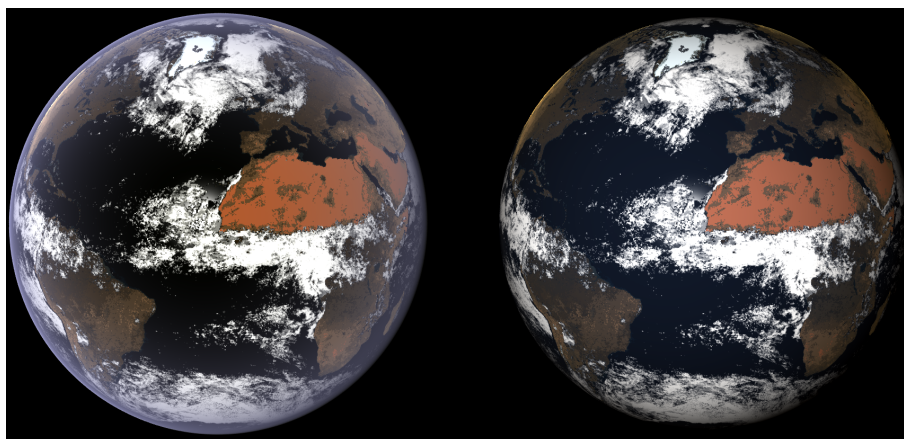


Figure 4.23: DIRSIG EPIC imagery simulation: With atmospheric reflection (left) and without atmospheric reflection (right)

## 4.2.4   Earth Object Radiometry

We now have a three shell model of the Earth. As mentioned in the Theory section [3.4], DIRSIG simulates radiative transfer using a ray tracing scheme. Rays are

cast into a scene and at each intersection with a scene object, material properties, geometry, and sampling scheme are taken into account to determine the attenuation of the ray. As mentioned, DIRSIG casts rays from observer to scene to source(s), opposite the direction of propagation, but radiometrically equivalent.

With the reflectance of the atmosphere set to zero, the total observed radiance ($L_{obs}$) is a sum of the sensor reaching reflected solar radiance from the cloud layer ($L_{cloud}$), and the sensor reaching reflected solar radiance from the surface layer($L_{surface}$).

$$L_{obs} = L_{cloud} + L_{surface} \tag{4.6}$$

The cloud radiance is given by:

$$L_{cloud} = L_{sun} * e^{-\delta(\Delta r_{down} + \Delta r_{up})} * \rho_{cloud} \tag{4.7}$$

where $L_{sun}$ is the solar radiance incident on the atmosphere, $\Delta r_{down}$ is the path length from an observed layer to the observed atmosphere layer, $\Delta r_{up}$ is the path length from an observed layer to the point of the atmosphere the ray intersects when traced to the sun , and $\rho_{cloud}$ is the diffuse reflectance of a cloud determined from the MODTRAN full cloud run scaled by the 0-1 fractional cloud map value at the observed cloud layer. The surface reflectance is given by

$$L_{surface} = L_{sun} * e^{-\delta(\Delta r_{down} + \Delta r_{up})} * \tau_{clouddown} * \tau_{cloudup} * \rho_{surface} \tag{4.8}$$

where $\tau_{clouddown}$ is 1 minus the fractional cloud map value at the observed cloud layer, $\tau_{clouddup}$ is the 1 minus the fractional cloud map value along the rays path towards the sun, and $\rho_{surface}$ is the BRDF of the observed surface of the Earth.

Figure 4.24: Representation of the ray tracing done by a single ray intersecting the Earth. The colors represent which simulation item the corresponding term is determined from. Blue represents platform profile, yellow represents the solar profile, orange represents the atmosphere layer, gray represents the cloud layer, and green represents the surface layer.

## 4.3 Real Data Comparison

In order to verify the validity of our model, MODIS and EPIC imagery were compared to DIRSIG simulations of our Earth object observed by virtual MODIS and EPIC systems with similar system, geometric, and radiometric parameters as used in collecting the real imagery.

### 4.3.1 MODIS Imagery Comparison

Our first real imagery comparison determines the statistical relationship between geographically similar Regions Of Interest (ROI) in a MODIS image taken on July 12th at 13:22 hrs [Fig: 4.25b] and an image taken by a virtual MODIS system [Fig: 4.25a].

(a) MODIS Simulation                    (b) MODIS
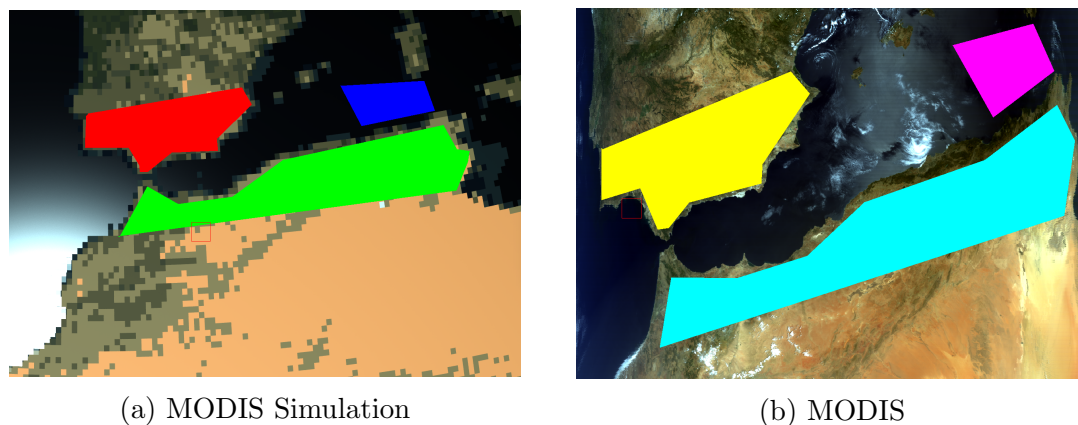
Figure 4.25: DIRSIG simulated MODIS (Left), MODIS (right) imagery, and their corresponding ROIs: red/yellow- Southern Spain, green/aqua - Northern Africa, and blue/pink - Mediterranean Sea

It can be seen from the figures that the MODIS imagery has some geometric warping that is unaccounted for in the simulation. This has little direct effect on the resulting radiance, but does make it more difficult to create geographically similar ROIs.

The corresponding spectral radiance mean of each ROI is determined. The means are used to determine the Root Mean Square Error (RMSE) using:

$$RMSE = \sqrt{\sum \frac{(L_{sim} - L_{ref})^2}{N}} \qquad (4.9)$$

where $L_{sim}$ is a simulated radiance, $L_{ref}$ is the real radiance, and $N$ is the number of samples of radiance [Table:4.28].

| Bands | South Spain | North Africa | Mediterranean Sea |
|---|---|---|---|
| | **Mean DIRSIG Spectral Radiance** [Watts/(m^2*sr*µm)] | | |
| 1  (620-670nm) | 85.31 | 125.39 | 22.47 |
| 4  (545-565nm) | 89.57 | 110.78 | 32.67 |
| 3  (459-479nm) | 85.75 | 96.88 | 49.30 |
| | **Mean MODIS Spectral Radiance** [Watts/(m^2*sr*µm)] | | |
| 1  (620-670nm) | 81.63 | 102.12 | 19.99 |
| 4  (545-565nm) | 113.75 | 126.57 | 46.29 |
| 3  (459-479nm) | 92.88 | 93.37 | 68.17 |
| | **Root Mean Square Error** [Watts/(m^2*sr*µm)] | | |
| RMSE | 14.71 | 16.36 | 13.51 |

Figure 4.26: Table of statistical relationship between regions of interest

This makes a mean RMSE of $\pm 14.86[\frac{watts}{m^2 sr \mu m}]$ across all the ROIs chosen. This is good considering the our RossLi parameters are created using an average over 8 days of imagery, while our simulation is of a single day. The potential variation within that time period, while beyond the scope of this paper quantitatively, is much greater. It stands to reason that the water would have the greatest error as well. The BRDF of water is a function of the local wind speed, which was not considered in attributing BRDF properties.

This comparison gives some insight into the viability of approximating our heterogeneous Earth as a collection of several homogeneous materials. But ultimately what we seek is some measure of error for visible RSO Earthshine apparent magnitude signatures. For that we turn to EPIC imagery.

## 4.3.2 EPIC Imagery Comparison

Our second real imagery comparison determines the accuracy which our Earth object was modeled and then extrapolates to expected visible Earthshine apparent magnitude signature error from our different RSOs using real and simulated 1024x1024 EPIC imagery over the bands 443nm, 551nm and 680nm bands.
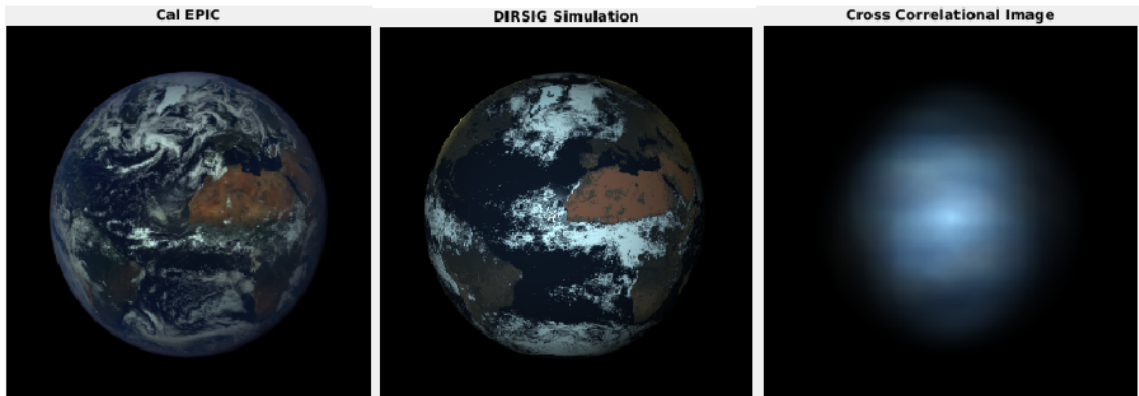


Figure 4.27: Epic image (Left), DIRSIG simulation of EPIC image (middle), cross correlation Images

There are some clear geographical regions that appear wrong, in particular the equatorial region of Africa. Here, the cloud map used has dense clouds, meanwhile the EPIC image shows sparse clouds. Of the three layers of the Earth, our

cloud layer is the most sensitive to real Earth temporal variations in reflectance.
The sampling is temporally the same for both the cloud map and surface reflectance
map. However, over the coarse of a few days the surface of the Earth might not
change significantly, the clouds on the other have can change dramatically. This
makes a spatially incorrect cloud layer model likely.

We explore the some statistical relationships between our Earth object and
the EPIC imagery to try and infer error. We first determine the image to image
mean difference, total radiance RMSE, the cross-correlation coefficient ($XC$) using:

$$XC = \frac{\sum_{i=1}^{n}(x(i) - \bar{x})(y(i) - \bar{y})}{\sqrt{\sum_{i=1}^{n}(x(i) - \bar{x})^2 \sum_{i=1}^{n}(y(i) - \bar{y})^2}} \tag{4.10}$$

where $i$ is the pixel index, $n$ is the number of pixels, $x(i)$ is the value of image one at
pixel index $i$, $\bar{x}$ is the mean value of the pixels of image 1, $y(i)$ is the value of image
two at pixel index $i$, and $\bar{y}$ is the mean value of the pixels of image 2.

We find a mean radiance for the EPIC image of $105.28[\frac{watts}{m^2 sr/mum}]$ and
a simulated mean radiance of $108.01[\frac{watts}{m^2 sr/mum}]$, making our for a mean radiance
difference of $+2.73[\frac{watts}{m^2 sr/mum}]$. We find a pixel for pixel RMSE of $\pm 66[\frac{watts}{m^2 sr/mum}]$ and
a cross-correlation coefficient of 0.655. While the RMSE is relatively large, it is not
actually emblematic of the error to be expected onto several of our RSOs.

Our ultimate goal is to determine the RSO Earthshine apparent magnitude
signatures from four characteristic RSOs with an altitude of 1000km: diffuse spheres,
specular spheres, diffuse flat plates, and specular flat plates. For the first three
RSOs, the reflected Earthshine signature is going to come from the entirety of the
observable Earth from the perspective of these RSOs, referred to as macro-regions.
For the final RSO, the reflected Earthshine signature will be a function of only
the region of Earth which is reflected towards the observer, referred to as a micro-
region. To approximate the radiance RMSE due to macro regions, we do a rebinning
of the images so that the new GSD approximately matches half the distance of the
macro-region. This corresponds to rebinning the images to 8x8.

Figure 4.28: 8x8 binning of imagery and corresponding difference image

From these new images we find an RMSE of irradiance ($\delta L$) of $\pm 28.3453 [\frac{watts}{m^2 sr/mum}]$ and a cross-correlation coefficient of 0.89. We take the RMSE and cross correlation values calculated with the unbinned images to approximate the micro-region error.

There is no standard measure for error for reflected Earthshine, and the difficulty determining one is compounding by not having real measurements of an Earthshine illuminated RSO. The error is to an unknown degree related to cross-correlation coefficient, but it is beyond the scope of this paper to derive by just how much, so that is reported separately. Since our coming treatment explores Earthshine apparent magnitude signatures, we propagate our radiance RMSE to observed RSO apparent magnitude error ($\delta m$).

First we convert our Earthshine radiance to exitance from the RSO:

$$M = L * \Omega_{RSO} * \rho_{RSO} \tag{4.11}$$

where $\Omega_{RSO}$ is the solid angle and $\rho_{RSO}$ is the reflectance of the RSO. Then using the error equation:

$$\delta F = \frac{\partial F}{\partial x} \delta x \tag{4.12}$$

where $F$ is some function, $\delta F$ is that function's error, $x$ is some variable which that function is dependent, and $\delta x$ is that variables error, we find an exitance error ($\delta M$) of:

$$\delta M = \delta L * \Omega_{RSO} * \rho_{RSO}. \tag{4.13}$$

Propagating that through the apparent magnitude equation we find an apparent magnitude error of:

$$log_{10}(e) * \frac{1}{M} \delta M = -1.0857 * \frac{\delta M}{M}. \tag{4.14}$$

63

Since $\frac{M}{\delta M}$ equals $\frac{L}{\delta L}$, our apparent magnitude error is given by:

$$\delta m = -1.0857 * \frac{\delta L}{L}. \tag{4.15}$$

Applying this **we find an Earthshine apparent magnitude signature error
of $\pm 0.28$ for reflected macro-regions and $\pm 0.68$ for reflected micro-regions.**

# Chapter 5

# Employing Models for Earthshine Analysis and Results

Using images of RSOs simulated with DIRSIG, this chapter does a quantitative and qualitative exploration comparing Earthshine to Sunshine as a source of illumination for RSOs and then using that to characterize visible RSO Earthshine apparent magnitude signature variability. Section 5.1 discusses quantitative analysis using our models. Section 5.2 & 5.3 use the DIRSIG model to explore a robust series of parameterizations for our scene and imaging systems. Section 5.4 summarizes quantitative results applicable to the variability in RSO Earthshine signatures.

As alluded to in the background [Ch: 2.1.1], exoatmospheric objects that are unresolvable are typically discussed in terms of apparent magnitude [Eq: 5.6]. Our examination is based on calculated apparent magnitudes, although there are many more system and environmental factors to consider when determining detectability of an object.  Fortunately, given our exploration into other systems, we know what apparent magnitude translates to in terms of detectability for the optical systems of the SSN.

Three topics are considered in our running analysis: the artifacts that arise in our simulations, the geometric and radiometric relationship of Earthshine to Sunshine, and insight that may be drawn from the Earthshine component of our simulations. Our exploration into characterizing Earthshine signature variability introduces a suite of simulations significantly removed from the typical implementation of DIRSIG. Throughout this analysis we run into a number of errors and artifacts, most of which do not stand in the way of our goals, but are explored to solidify confidence in our findings. Relating RSO Earthshine to the Sunshine component is used as a natural way for us to contextualize our Earthshine discussion and relate our research to some previously done work. Ultimately, only what can be related back to RSO Earthshine signature variability is drawn upon for our conclusion of this section and this thesis.

There are four regularly used terms to describe the angular displacement of our RSO, the surface normal, and the observatory. In our treatment: phase refers to the angular dispacement of physical objects and angle refers to the angular displacement in a local coordinate system.

### *Geometric Convention*



(a) SEOPhase



(b) SOOPhase



(c) Observation Angle



(d) Orientation Angle
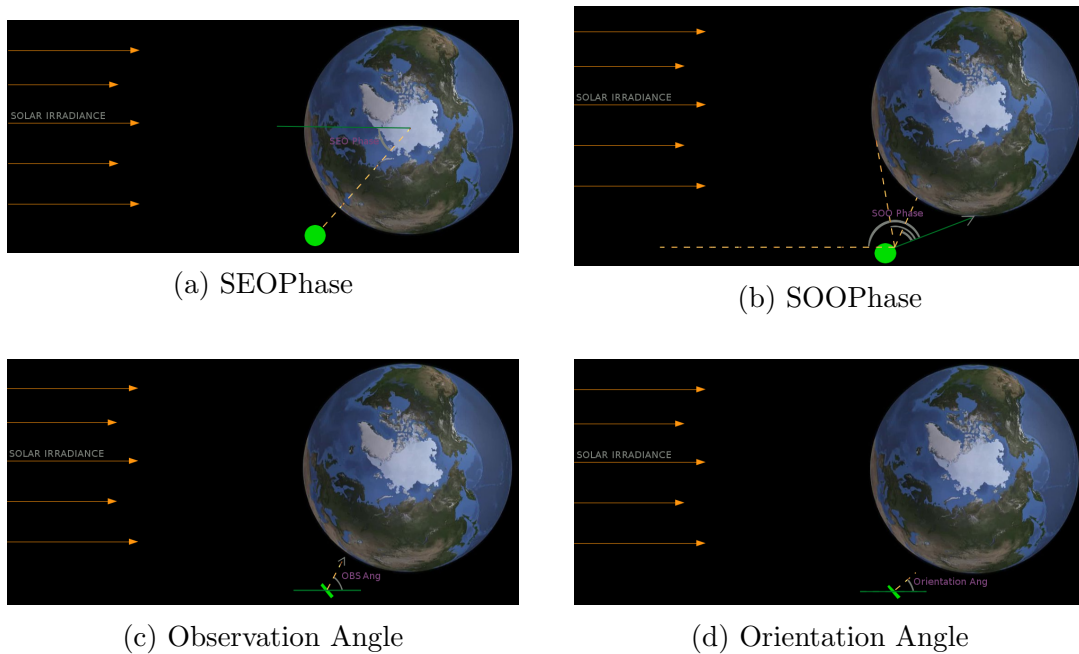
Figure 5.1: Geometric convention

- Sun Earth Object Phase (SEO): The angular displacement between a direction vector pointing from the center of the Earth at the sun and towards an RSO.

- Source Object Observatory Phase (SOO): The angular displacement of a direction vector pointing from the RSO towards the source of irradiance and the observatory. This is used liberally and depending on cotext can be reffering to a source direction vector pointing towards the sun, at location on the Earth, or the center of the Earth.

- Observation angle (OBS Ang): The angular displacement of an observatory off an axis defined as positive facing away from the sun. OBS ang can be used to calculate the SOO, but due to ambiguity of SOO convention, is kept separate for most of the analysis.

- Orientation angle (Orientation Ang): The angular displacement of the normal of the surface off an axis defined as positive facing away from the sun.

## 5.1 Quantitative Analysis with DIRSIG

Our first series of simulations use a diffuse Earth approximation to provide a basis from which to compare the results from our heterogeneous Earth model. As previously discussed [Ch: 3.4], the ray tracing technique does not take into account the geometry of the scene when sampling, but instead a predetermined sampling based on user input and BRDF shape. This has the potential for over sampling regions of little contribution and under sampling regions of major contribution. Another consideration is the geometric rendering capabilities of DIRSIG. This presents itself in our analysis of spherical geometries; instead of being approximated as a facetized object, the spheres of DIRSIG are interpolated based on the angle of incidence of the sampling ray.

The outputs of our DIRSIG simulations are spectral radiance images $[\frac{watts}{cm^2 sr \mu m}]$ of the entire scene. Our images can have 4 sources of light: background Sunshine (SS), background Earthshine (ES), reflected Earthshine (RE), and reflected Sunshine (RS) [Fig: 5.2].
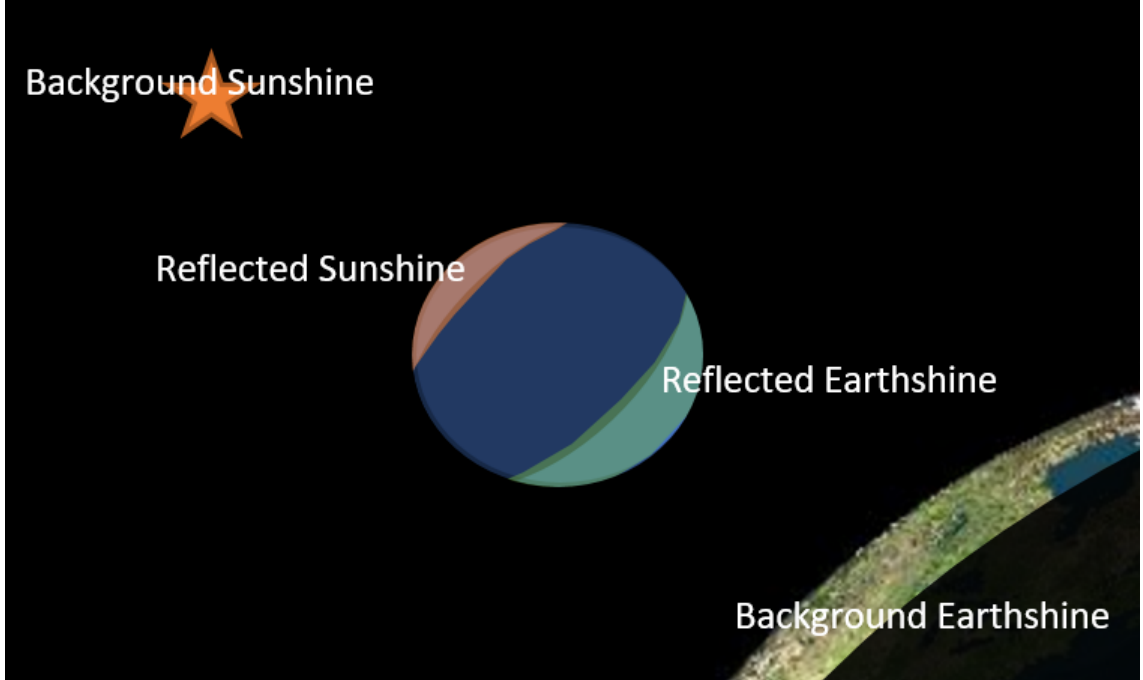
Figure 5.2: Representation of a simulated image of a spherical RSO with all the
potential sources of light. Liberties are taken with scale to aid in illustration.

What we seek is isolated measurements of reflected Earthshine (RE), Sunshine (RS),
and the total RSO illumination (RE+RS). To get these quantities, four versions of
each simulation are created: full scene (SS+ES+RE+RS), all dark objects scene
(SS), dark Earth scene (SS+RS), dark sat scene (SS+ES). These are then linear
combined to create our 3 quantities.

$$IM_{RSOtotal} = IM_{FullScene} - IM_{DarkSatScene} \tag{5.1}$$

$$IM_{SunShine} = IM_{DarkEarthScene} - IM_{AllDarkScene} \tag{5.2}$$

$$IM_{EarthShine} = IM_{RSOtotal} - IM_{SunShine} \tag{5.3}$$

Visual inspection of the resulting images allows for a reality check on our
simulations, making sure the Earthshine and Sunshine contributions are incident as
expected. Our quantitative analysis considers the sum total of the radiance image
related back to the apparent magnitude. To get our image into apparent magnitude
we need first make the radiance image into a total irradiance $E_{RSO}$.

$$E_{RSO} = \Omega * Bandwidth \sum_i \sum_j Im(i,j) \tag{5.4}$$

69

$$\Omega = \left(\frac{P}{fl}\right)^2 n_x n_y \tag{5.5}$$

where $\Omega \equiv$ total solid angle, P$\equiv$ pixel pitch, fl $\equiv$ focal length, $n_x \equiv$ number pixel rows, $n_y \equiv$ number pixel columns, and Bandwidth is the largest wavelength sampled minus the smallest. Next that value is put into a generalized apparent magnitude given by:

$$m_{obj} = -26.74 - 2.5 * log_{10}\left(\frac{E_{RSO}}{E_{Sun}}\right) \tag{5.6}$$

where $E_{Sun}$ is the sum of the incident solar radiation onto the Earth over the same bandpass as the imaging system.

DIRSIG simulation speed inversely scales with the number of spectra samples used, so we try and minimize the number of samples. Unfortunately, that comes with some error. DIRSIG takes a spectrum sampling based on a user defined sampling interval. Since the Solar Irradiance spectrum is not smooth, this can cause some discrepancies between the actual radiation and the simulated radiation [fig:5.3].
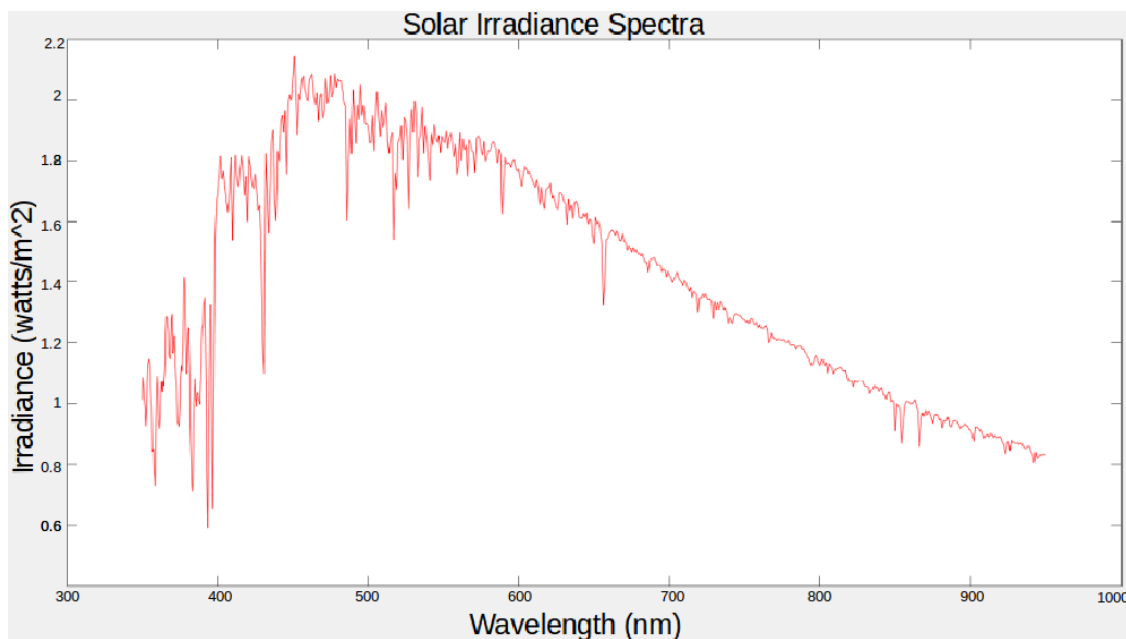


Figure 5.3: Solar Earth reaching irradiance

Along the same lines, DIRSIG does not allow for a user to simply use a response $R(\lambda)$ of 1 for a bandpass of consideration. It instead takes into account the sampling and interpolates. A RECT function defining the desired bandpass is sampled with a COMB function and then convolved with another RECT function [FIG: 5.4].

$$R_\lambda = RECT(\frac{\lambda}{d\lambda}) * (RECT(\frac{\lambda - mdpt}{\Delta\lambda}) \cdot COMB(\lambda - d\lambda)) \qquad (5.7)$$

where $\lambda$ is an arbitrary wavelength, mdpt is the middle wavelength of the bandpass, $d\lambda$ is a user defined sampling interval, and $\Delta\lambda$ is half width of the bandpass.
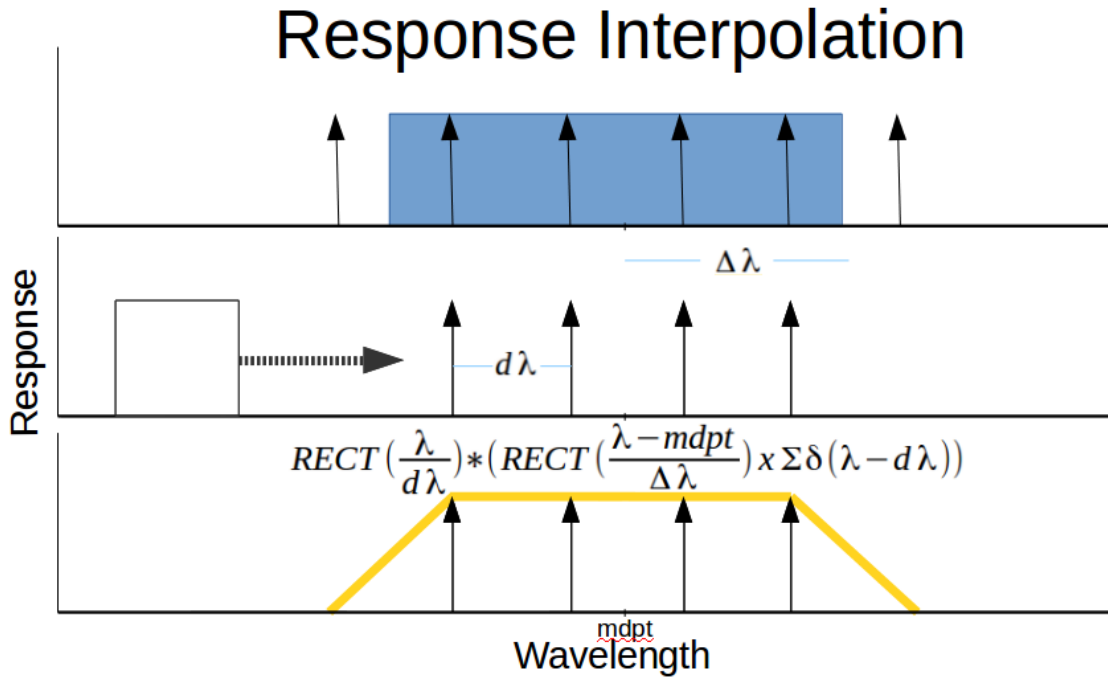


Figure 5.4: Sampling a RECT response with a COMB, then interpolating by convolving with a RECT

This all is taken into account when calculating the irradiance of the sun for the apparent magnitude. The irradiance of the sun must be the same irradiance propagated through the scene.

71

A scale factor (SclF) can be added into the RSO irradiance calculation
to change the size (R') of the RSO as long as the size stays under several orders
of magnitude of the radius of the Earth. Also the same thing can be done with
the observation distance (Obs') without the introduction of too much error if the
distance stays several orders of magnitude above the radius of the RSO.

$$SclF = \frac{R^2}{R'^2} \frac{Obs'^2}{Obs^2} \tag{5.8}$$

where the prime indicates the desired value and not prime indicates the actual value.

## 5.1.1   Data Simulation and Representation Convention

Here we describe the conventions we used to describe the multiple angular depen-
dence of the RSO images.

**Spherical RSO Convention**
The sphere RSO simulations use DIRSIG 'waypoints' to flesh out the two angular
dependencies which the measured reflected RSO radiation is dependent: SEO phase
and Observation angle. This amounts to a list of ENU coordinates matched with
times. Because DIRSIG interpolates between points using the time derivative of the
spatial change vectors, we made every desired point between two points in the same
locations with a higher and lower time; this makes the time derivative zero and gets
rid of motion blur.

For the homogeneous diffuse Earth object, the sun is incident on the Earth
object at Lat 0 Lon 0. The RSO is maintained on the equatorial plane while being
iteratively located at 13 geographical locations between longitude 0 and longitude
180 for steps of 15 degrees. At every geographical location, a platform maintained
on the equatorial plane is iteratively located at 31 locations 360 degrees around the
RSO for steps of 12 degrees . At every iteration of platform motion two images are
simulated, an image of the Sunshine reflected from the RSO, and an image of the
Earthshine reflected from the RSO [fig: 5.8]. The real Earth object differs by moving
the RSO iteratively around the entire Earth 360 degrees. Starting and ending at Lon
180. These simulations are characterized with resolved and unresolved individual
normalized double phase plots, combined double phase plots, and as an Apparent
Magitude as a function of simulated image.
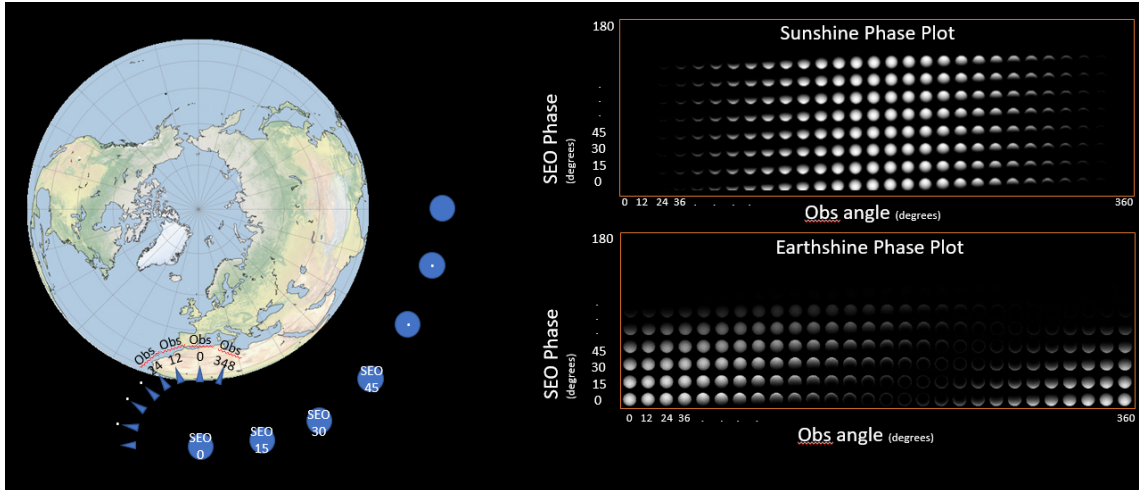
Figure 5.5: Representation of the resolved double phase plot convention using equatorial orbit example.

Each image is converted into apparent magnitude, and then a plot of apparent magnitude as a function of simulated image is created. The apparent periodicity of the plot corresponds to the iterative change of the RSO position, while the structure in between the peaks corresponds to the iterative change of the observatory.
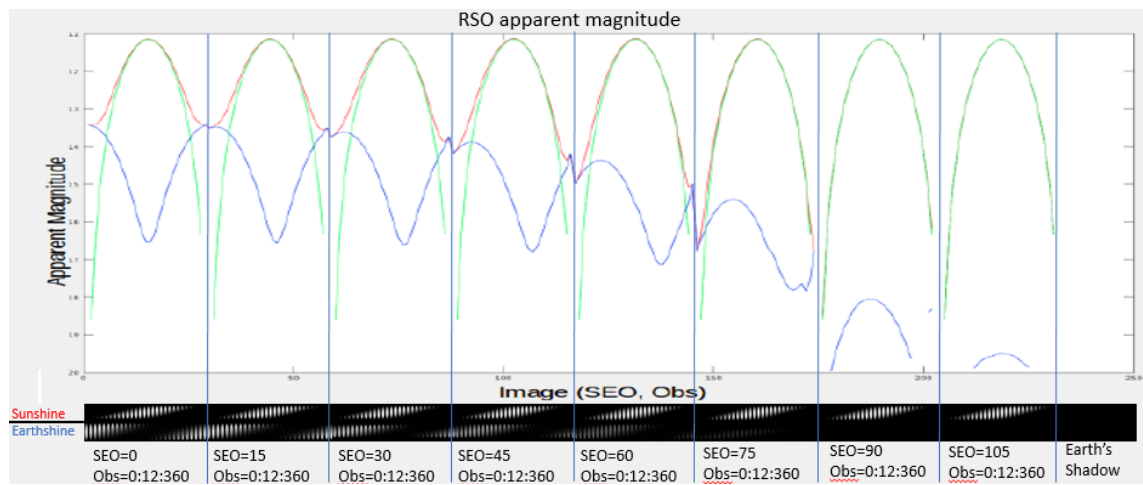


Figure 5.6: Representation of the spherical RSO apparent magnitude plot and how it related back to the double phase plots.

**Flat Plate RSO Convention**
The flat plate RSO simulations use DIRSIG 'motion' to flesh out 1 of the 3 phases

which the measured reflected RSO radiation is dependent, the off normal flat plate
orientation angle. The RSO is rotated about it's Geospatial location iteratively each
degree of a complete rotation. The observation angle is only fleshed out by having
a simulation of observation angle of 0 (shared lat/lon as RSO) and a subsequent
simulation of 90 degrees out of phase, and not in every case. The third phase of
dependence, SEO phase, is captured with subsequent simulations which use shifted
DIRSIG 'waypoints'.

The sun is incident on the Earth object at Lat 0 Lon 0. For each flat plate
simulations the observatory is fixed at a indicated observation angle. The object
is maintained at an indicated geographical location while being iteratively rotated
about it's local z-axis, which is parallel with the Polar axis of the Earth. At every
iteration of rotation two images are simulated: an image of the Sunshine reflected
from the RSO, and an image of the reflected Earthshine from the RSO. The resulting
images are represented with a phase plot, with the first (from left to right and top
to bottom) being representative of an orientation angle of 0, the second an angle of
1, all the way to the last being an angle of 359 [Fig: 5.7]. There is no difference for
conventions between the real Earth and diffuse Earth simulations. These simulations
are characterized with resolved individual normalized double phase plots, combined
double phase plots, and as an apparent magnitude as a function of simulated image.
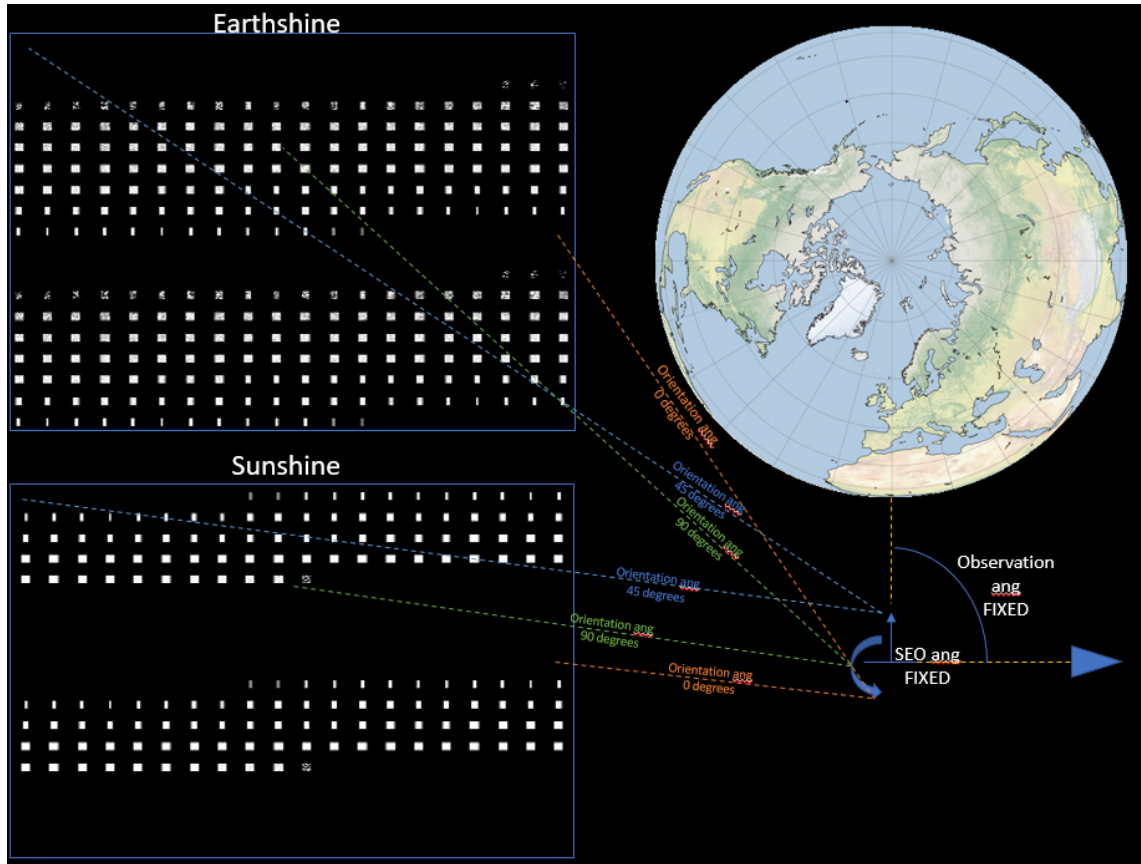
Figure 5.7: Representation of the resolved phase plot convention using Lat 0 Lon 0
Obs 90 example.

Each image is converted into apparent magnitude, and then a plot of apparent
magnitude as a function of simulated image is created. In this case, it can just as
easily be considered a function of orientation angle as it is simulated image.
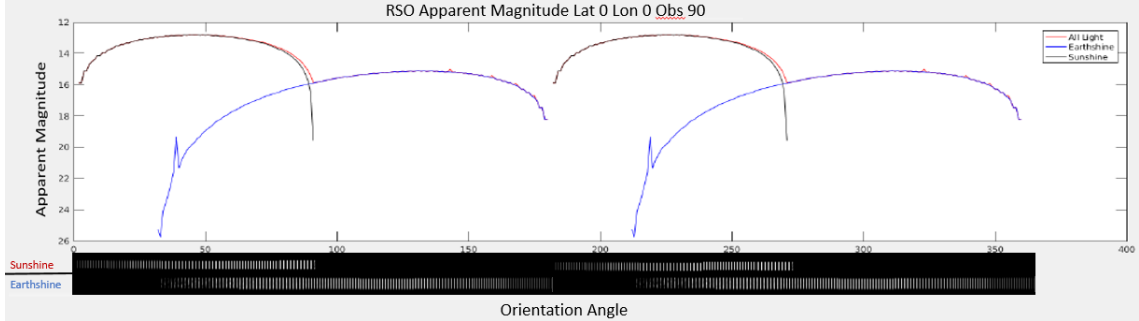
Figure 5.8: Representation of the flat plate RSO apparent magnitude plot and how it related back to the single phase plots.

## 5.2 DIRSIG - Diffuse Earth Analysis

In this series of simulations we analyze the Earthshine which would emanate from a homogeneous diffuse Earth approximation incident onto two characteristic RSO geometries: a flat plate and a sphere, with two characteristic RSO reflectances: diffuse and near specular. The reflectance of the Earth object is set to 0.3, based on the previously mentioned Earthshine measurements [Ch: 2.1.2]. The total albedo of both the specular and diffuse RSO objects is set to 0.15, as to follow the convention of previous analyses done into detecting RSOs using Sunshine [17]. All scenarios are done with an RSO object located 1,000 km above the Earth's surface with an imaging system located 1,000 km away from the RSO. Spherical objects are given a radius of 200m and planes are given a square side length of 200m. A scale factor (SclF) is used to rescale the RSO objects size parameters to 10cm as opposed to using a 10cm object because limits posed by DIRSIG's interpolation capabilities.

### 5.2.1 Diffuse Sphere RSO

For this simulation, several plots are derived from the simulated imagery: A double phase normalized RSO image plot, a normalized combined RSO image plot, and an apparent magnitude plot of our three quantities. The first phase plots are for a qualitative understanding of how light changes with the two phase angles respectively. The final is for quantitative analysis of Earthshine vs Sunshine, and is later used in comparison with the Real Earth object simulations.

76
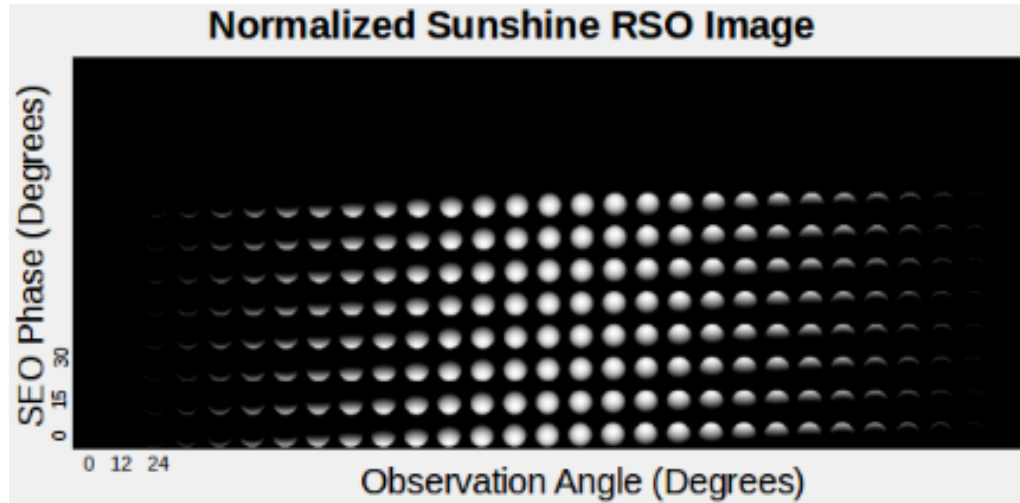
Figure 5.9: Diffuse Earth object and diffuse sphere RSO double phase relation from
Sunshine
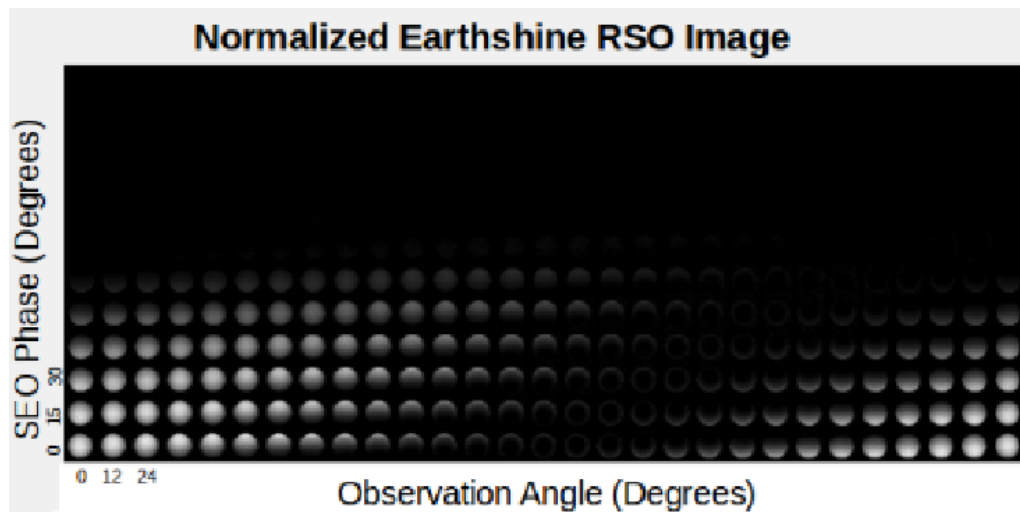


Figure 5.10: Diffuse Earth object and diffuse sphere RSO double phase relation from
Earthshine
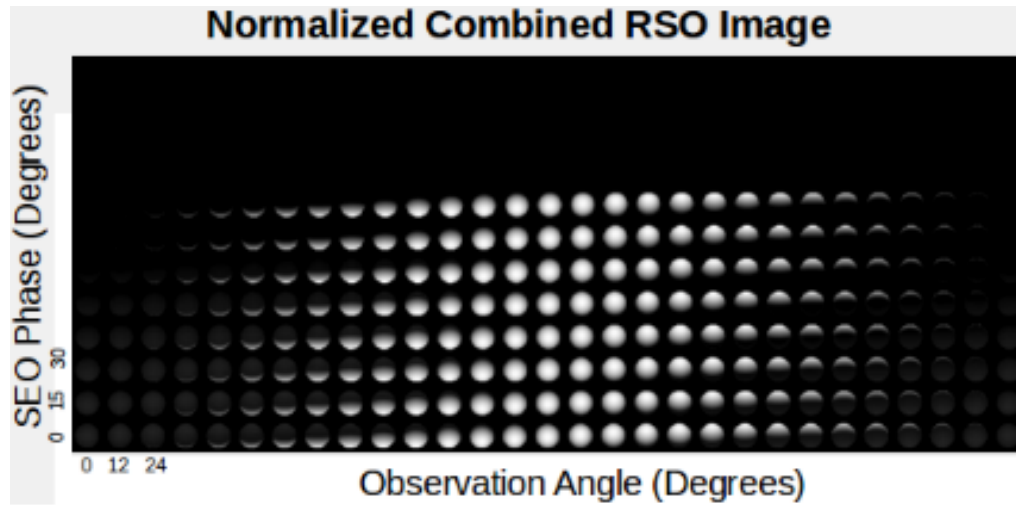
Figure 5.11: Diffuse Earth object and diffuse sphere RSO adjusted double phase relation from Sunshine and Earthshine
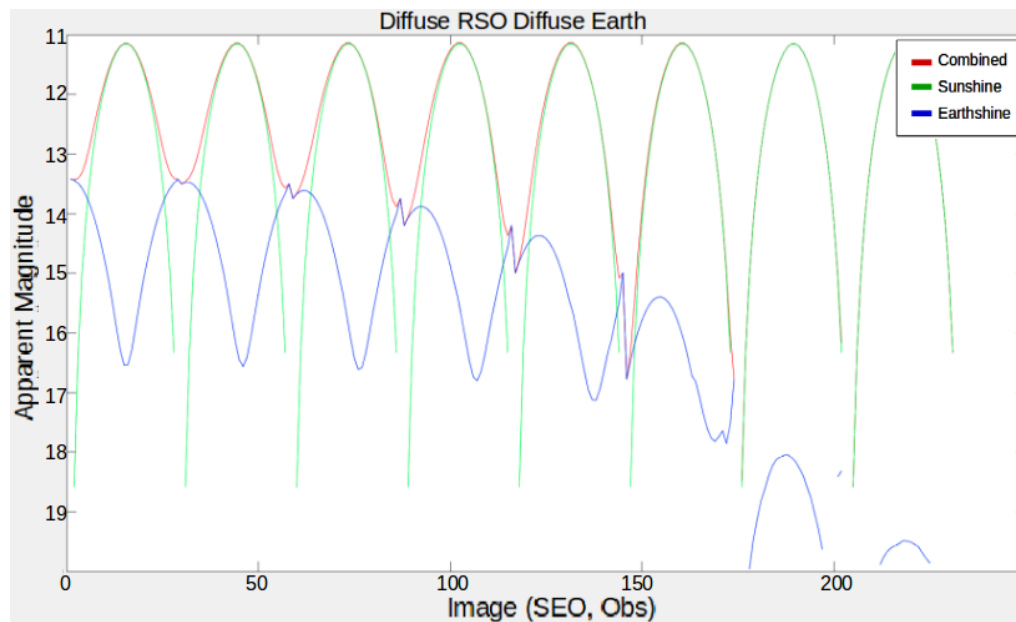


Figure 5.12: diffuse Earth object and diffuse sphere RSO apparent magnitude plot from Sunshine, Earthshine, and the sum.

There is symmetry in the SOO phase of the Sunshine intensity while the Earthshine intensity shifts as it orbits about the Earth. This make sense due to

the counter shifting of the distribution of illumination on the Earth with the SEO
phase. The max apparent magnitude of Earthshine is 13.5 while the max Sunshine
is 11.2, a radiance ratio of 8.3.

## 5.2.2 Specular Sphere RSO

In this simulation we replace the diffuse BRDF material property of the spherical
RSO with a near specular BRDF created with a wardBRDF [Eq: 3.5] with roughness
parameters of 0.01 and the same albedo of 0.15. The reason a specular lobe was
chosen over a purely specular materials was to increase the observable size of the
reflected solar radiation and to improve likely hood of intersection with a secondary
specular reflection from the Earth in later simulations. The geometric configurations
and the output structure are the same as obtained with the diffuse RSO diffuse Earth
simulations.
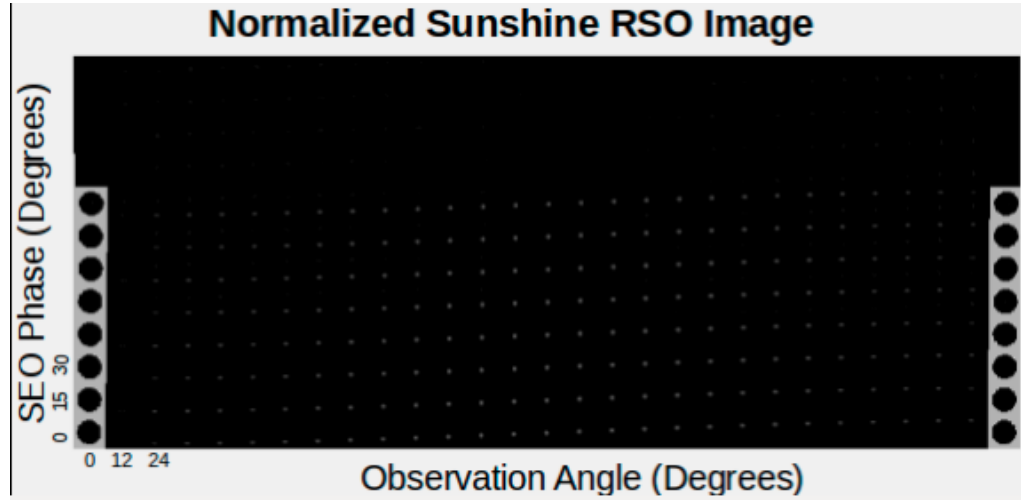


Figure 5.13: Diffuse Earth object and specular sphere RSO double phase relation
from Sunshine
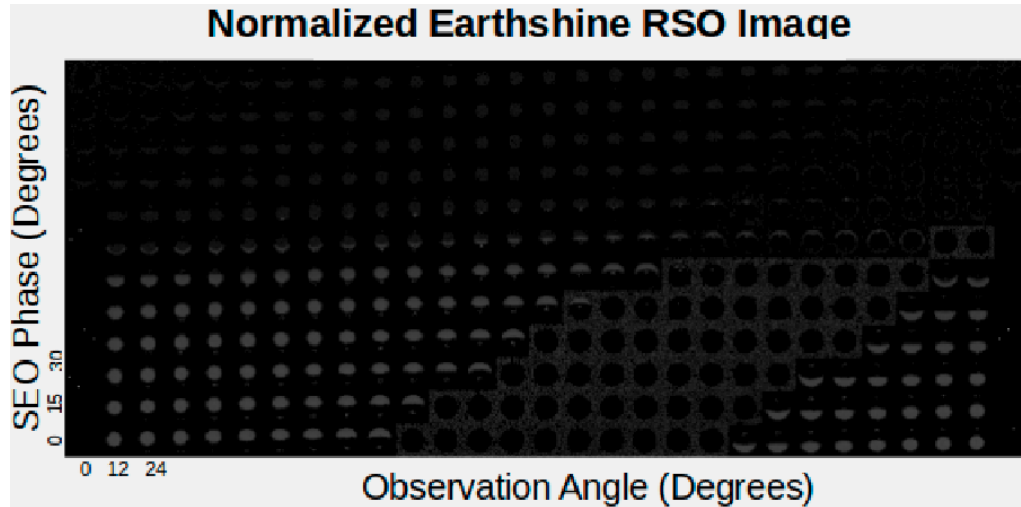
Figure 5.14: Diffuse Earth object and specular sphere RSO double phase relation
from Earthshine
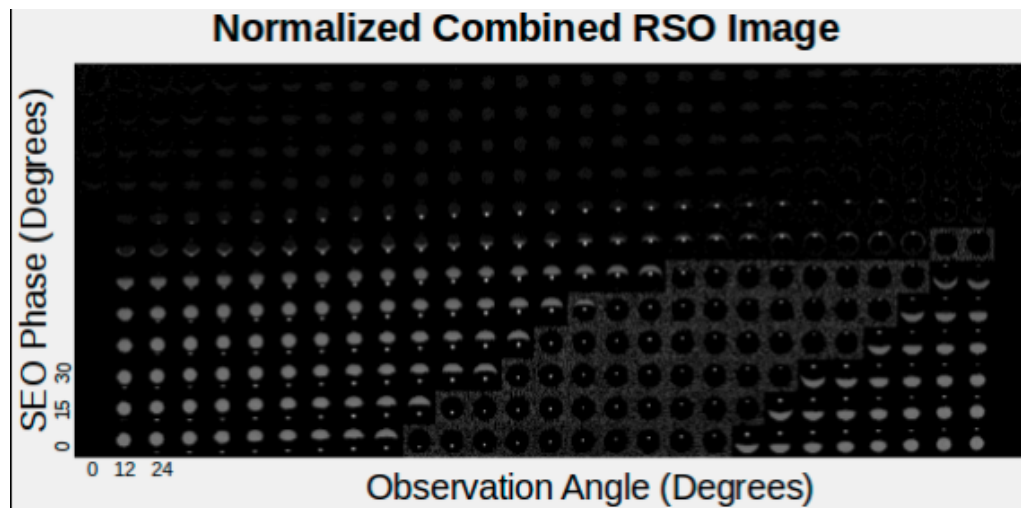


Figure 5.15: Diffuse Earth object and specular sphere RSO adjusted double phase
relation from Sunshine and Earthshine
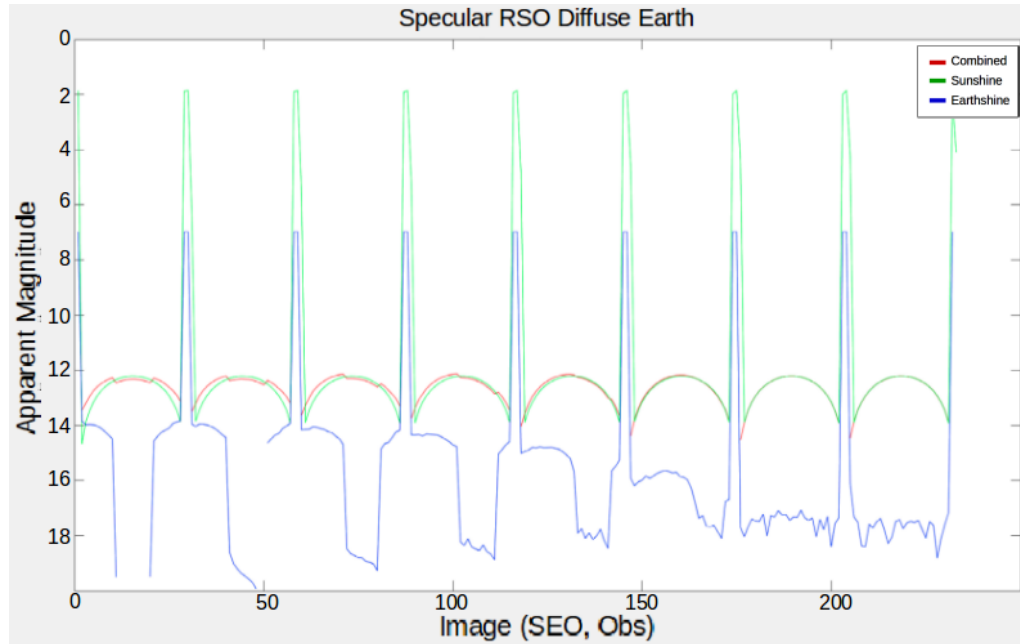
Figure 5.16: Diffuse Earth object and specular sphere RSO apparent magnitude
plot from Sunshine, Earthshine, and the sum.

For starters, there appears to be some degree of error when linearly com-
bining our quantities.
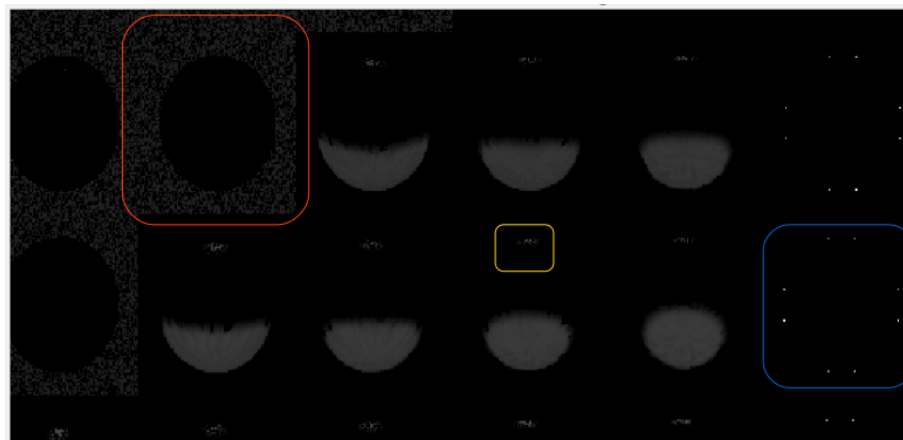


Figure 5.17: Zoomed in Earthshine double phase depiction of places of errors. Red -
background Earthshine, Yellow - residual reflected Sunshine, and blue - background
Sunshine

There are three visible artifacts in the Earthshine phase imagery [Fig: 5.17]: background Earthshine (red), residual reflected Sunshine (yellow), background Sunshine (blue). All of these artifacts stem from inconsistencies between the images when linearly combining them to get our desired quantities. The background Earthshine, reflected Sunshine, and background Sunshine is different in the $IM_{RSOtotal}$ image as it is the $IM_{Sunshine}$, so when combined the resulting $IM_{EarthShine}$ has the difference in quantities included.

Understanding exactly what is going and midigating these errors is a subject of ongoing research. One source comes from the nature of the sampling of reflected beams using a WardBRDF. The rays cast have a distribution based on the shape of the BRDF, some user defined hemispheric angular quantization, and is random there in; that is to say, there are multiple solutions that satisfy the BRDF distribution criteria and DIRSIG quasi-randomly picks one for each run. Fortunately, the artifacts are apparent and analysis can be done *around* them. The smooth curved surfaces are what we expect for the shape of the local peaks, the sharp peaks in the above Specular RSO apparent magnitude plot are actually background Sunshine. The other artifacts found in the phase images have a negligible contribution to the apparent magnitude plot.

The rounded shape of the Sunshine is to be expected. A specular sphere will reflect radiation emanating from a point source in all directions except exactly 180 degrees out of phase with the incidence. The max Earthshine is 13.84 while the Sunshine is 12.10, a radiance ratio of 5. This is reasonable though may be a little low considering the artifacts.

## 5.2.3 Diffuse Flat Plate RSO

This set of simulations are initial efforts to analyze the orientation dependence of the apparent magnitude of a surface. The sphere of the previous simulations has no orientation, but serves as a viable tool for analyzing the other angular dependencies: SOO phase and SEO phase. Our focus is limited to rotations about the Y-axis of a square flat plate defined by $[x_{min}, y_{min}, z_{min}] = [-100m, -100m, -.001m]$ & $[x_{max}, y_{max}, z_{max}] = [100m, 100m, .001m]$ in an ENU coordinate system, shifted in the global ENU system in subsequent simulations. To get some degree of understanding of the other phase parameters of the flat plate, one simulations changes the SOO phase by 90 degrees, and another changes the SEO phase by 90 degrees. The RSO and Earth material properties are consistent with the previous simulations'

materials. There are four plots derived for each simulated imagery set: an apparent
magnitude plot for our quantities and a normalized orientation phase magnitude
map for Sunshine, Earthshine, and the total.

## Rotating Flat Plate Lat 0 Lon 0 Obs 0
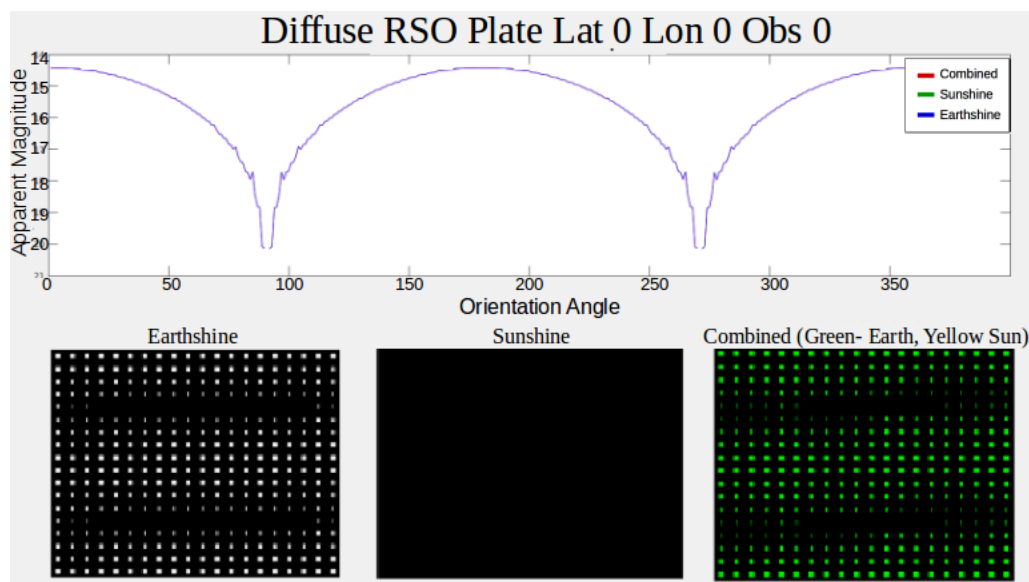


Figure 5.18: Representation of a diffuse flat plate rotating at an altitude of 1000km
above Lat 0 Lon 0 with an observing phase of 0 degrees. Top - Sunshine Earthshine
and Total plotted on Magnitude plot. Bottom left - Normalized Earthshine phase
plot. Bottom middle - normalized Sunshine Phase plot. Bottom right - combined
phase plot.

Here we see that there is no contribution from the Sunshine. This is because
the sun is 180 degrees out of phase with the observatory. This results in the flat
plate RSO never having a Sunshine illuminated side that has a normal less the 90
degrees out of phase with the direction of the imaging system. The Earthshine
behaves exactly as we would expect, falling off only with the geometry of the Earth.

There is a smaller measured maximum of 14.43 for the flat plate verses
the 13.43 for the sphere, a radiance ratio of 2.511 which stems from two places.
First, and the largest contributer is the difference is projected area; the sphere has

a projected area of a factor of $\pi$ larger then flat plate. Secondly, is how the two spherical geometries relate with each other; Every SOO of the Earth has a point on the sphere where there is no geometric fall off due to surface orientation and another part where it falls off to zero, where as the flat plate has the same geometric fall off across its surface for each SOO. In our case this works to make the ratio $\frac{2.5}{\pi}$ less then a pure projected area discrepancy. If the Earth was flat and had infinite area of extent, the values would be the same except for projected area discrepancies.

## Rotating Flat Plate Lat 0 Lon 0 Obs 90
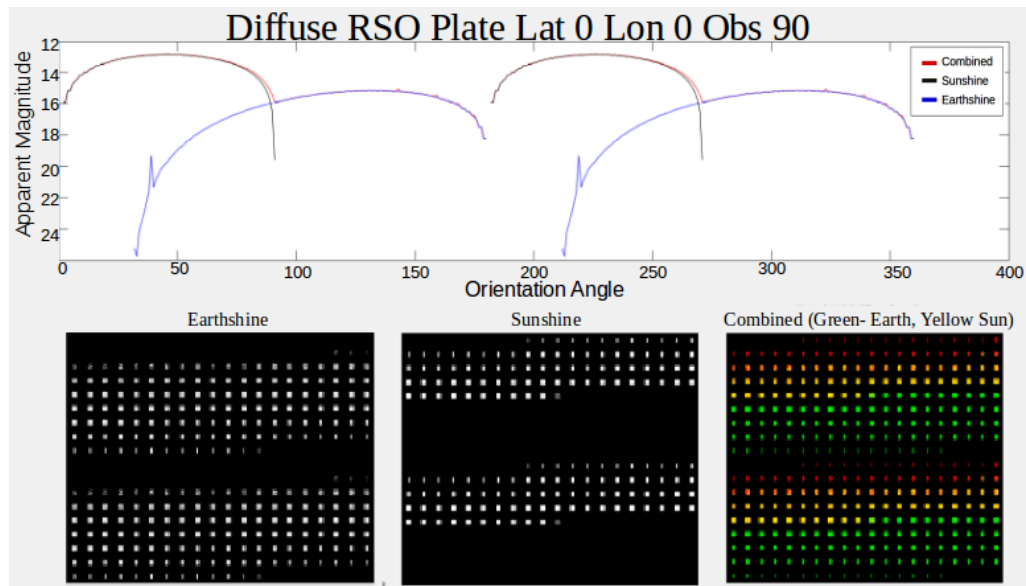


Figure 5.19: Representation of a diffuse flat plate rotating at an altitude of 1000km above Lat 0 Lon 0 with an observing phase of 90 degrees. Top - Sunshine Earthshine and total plotted on apparent magnitude plot. Bottom left - normalized Earthshine phase plot. Bottom middle - normalized Sunshine phase plot. Bottom right - combined phase plot.

By placing the observatory 90 degrees out of phase we get our best look at how Sunshine and the Earthshine change relative to one another based on Orientation angle. At an orientation angle of 45 degrees, the sun peaks at 12.85, at 135 degrees the Earth peaks at 15.15. The Sun can be seen throughout 90 degrees of

orientation, while the Earth can be seen closer to 150 degrees. Their illumination comes from entirely different directions, that means the Earthshine exists and is maximal at an entirely different gamuts of the orientations.

## Rotating Flat Plate Lat 0 Lon 90 Obs 90
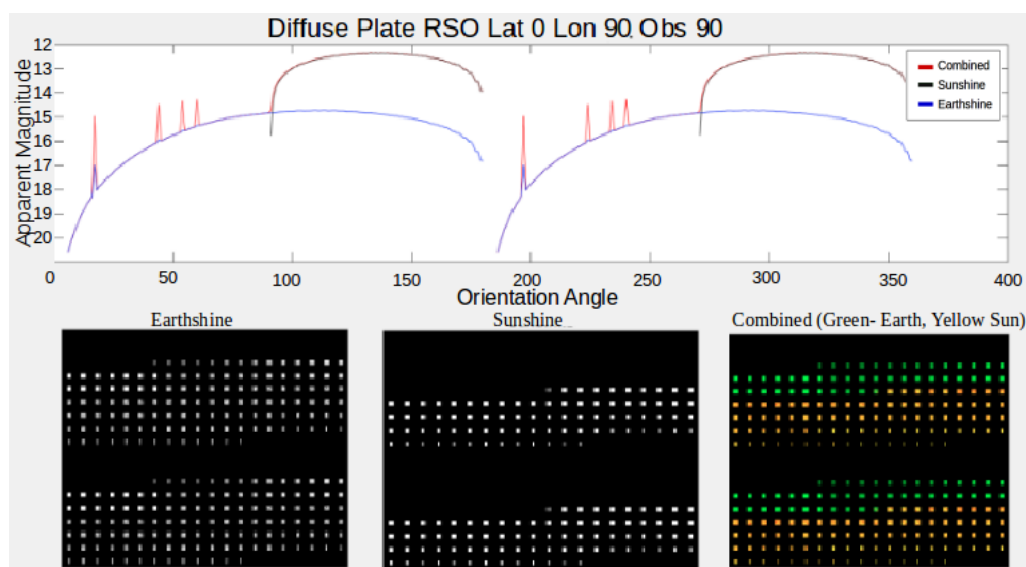


Figure 5.20: Representation of a diffuse Flat Plate rotating at an altitude of 1000km above Lat 0 Lon 90 with an observing phase of 90 degrees. Top - Sunshine Earthshine and total plotted on apparent magnitude plot, bottom left - normalized Earthshine phase plot, bottom middle - normalized Sunshine phase plot, bottom right - combined phase plot.

The red spikes seen in this simulation are artifacts whose origin are beyond the scope of this paper. This simulation offers little more insight then previously explored. As we get more towards the limb of the Earth, the Earthshine contribution diminishes and shifts relative to the Sunshine contribution. Their incident vectors become closer. This can be seen in the spherical RSO analysis as well.

### 5.2.4 Specular Flat Plate RSO

The specular flat plate RSOs serve as a tool for analyzing the directional dependence of Illumination. For a homogeneous diffuse Earth object, there is little to be observed except for the geometric fall off of the Earth. The geometric configurations and output structure are the same as obtained in the diffuse flat plate RSO diffuse Earth simulations.

## Rotating Flat Plate Lat 0 Lon 0 Obs 0
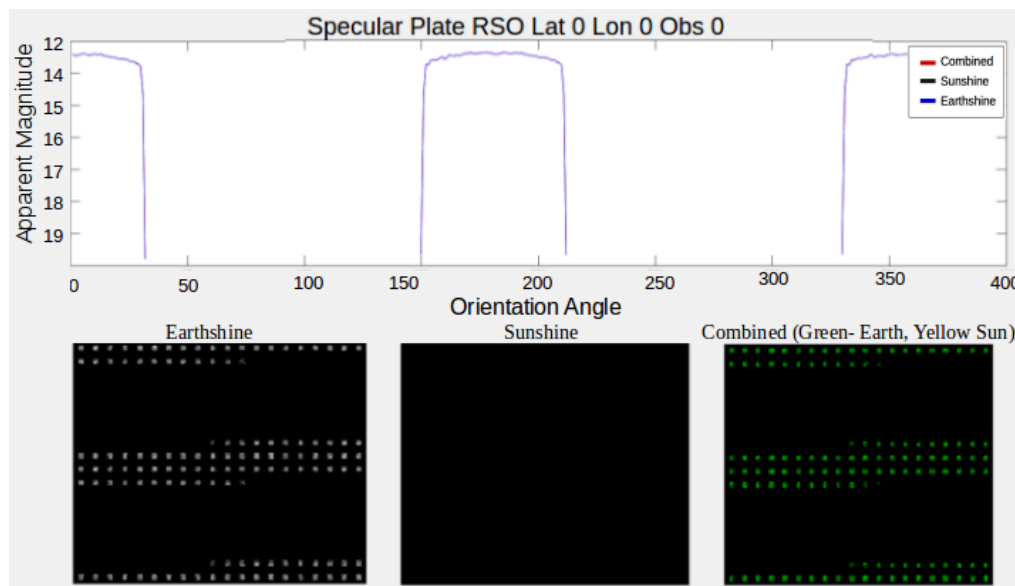


Figure 5.21: Representation of a specular flat plate rotating at an altitude of 1000km above Lat 0 Lon 0 with an observing phase of 0 degrees. Top - Sunshine Earthshine and total plotted on apparent magnitude plot, bottom left - normalized Earthshine phase plot, bottom middle - normalized Sunshine phase plot, and bottom right - combined phase plot.

The max apparent magnitude is 13.38. The results obtained from this simulation make sense. The increase in brightness from the diffuse RSO of 1 speaks to the nature of diffuse reflectance. Instead of being reflected in all directions, a portion of it is reflected in one direction. The result is that it cannot be seen at as many orientations, but it is brighter at the ones it can be seen at. If the Earth was instead flat with an infinite angular extent, they would have the same value.

## Rotating Flat Plate Lat 0 Lon 0 Obs 90
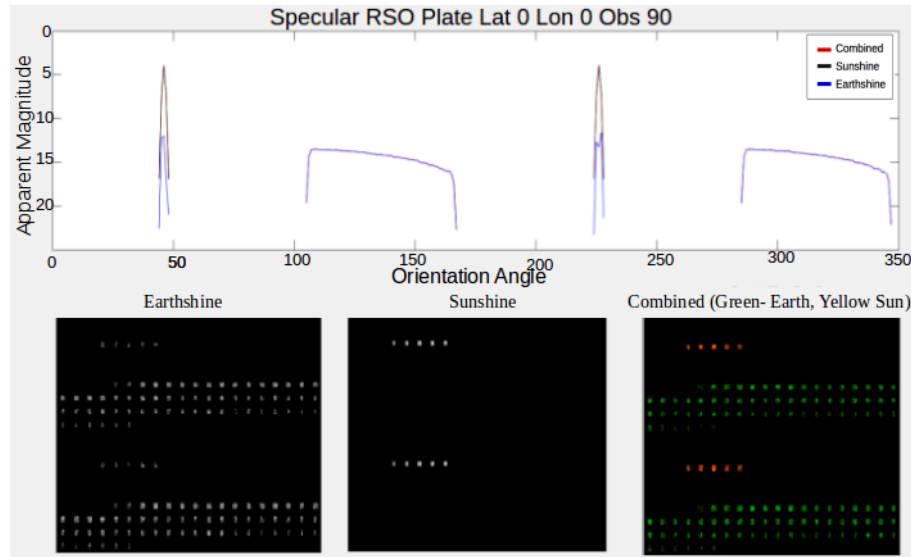


Figure 5.22: Representation of a specular flat plate rotating at an altitude of 1000km above Lat 0 Lon 0 with an observing phase of 90 degrees. Top - Sunshine Earthshine and total plotted on apparent magnitude plot, bottom left - normalized Earthshine phase plot, bottom middle - normalized Sunshine phase plot, and bottom right - combined phase plot.

Here we can see a reflected apparent magnitude of 4 from the Sunshine. This peak was to be expected, and due to the size of the specular lobe is actually a bit smaller then a true specular reflectance. The Earthshine does not change much except to shift the plot by the shift in orientation angle, and to incorporate the new fall off. The max apparent magnitude is 13.5

## Rotating Flat Plate Lat 0 Lon 90 Obs 90
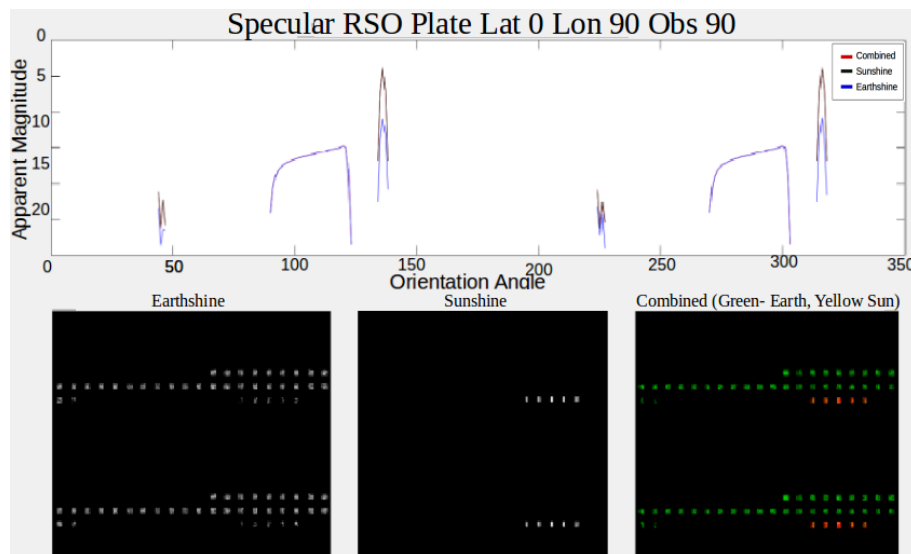


Figure 5.23: Representation of a specular flat plate rotating at an altitude of 1000km above Lat 0 Lon 90 with an observing phase of 90 degrees. Top - Sunshine Earthshine and total plotted on apparent magnitude plot, bottom left - normalized Earthshine phase plot, bottom middle - normalized Sunshine phase plot, and bottom right - combined phase plot.

At a SEO angle of 90, the Earthshine's angular extent is cut in half, as is the Orientations angles at which it can be observed. The max apparent magnitude is 14.81.

### 5.2.5 Diffuse Earth Discussion

The diffuse Earth approximation captures the average expected apparent magnitude of RSOs illuminated by it pretty well, but not the extremes. It serves as a good reference for understanding the general geometric relationships between the Earth, RSOs, and Observatories, but lacks the refinements needed to really quantify the potential 'relevance' of Earthshine in RSO detection. In reality an Observer may try to do their best to Utilize Sunshine and the best cases of Earthshine. While we did get results that showed Earthshine had a comparable contribution to RSO

illumination as Sunshine while the RSOs were located towards the low SEO phase angles, currently the Optical SSN is comprised completely of Earth based telescopes. This means that the objects will likely be closer to a 90 degrees SEO phase when observed to minimize the brightness of the sky, which means an apparent magnitude difference of 1.25 or $\frac{1}{3}$ the radiance of peak measurements. This may still be enough for some applications.

One interesting thing that came from this analysis was the similarity in apparent magnitude for the specular and diffuse spheres and flat plates. Because of the large solid angle they all had similar maximums proportional to their projected areas. Had the Earth had a 180 degree angular extent, they would have all proportionally had the same maximums. So the closer you get to the Earth, the more similar spheres and flat plates appear. This is simply not the case for the sun. This lends it's self to the potential for insights into RSO's material properties and geometries being pulled from the contrast of the measured reflected Sunshine and Earthshine.

## 5.3    DIRSIG - Real Earth Object Analysis

This suite of simulations utilize our Real Earth object built using our DIRSIG work flow [Sec: 4.2] to explore the geo-spatial variability of Earthshine. The Earth object used in this suite is much more complex then the Earth object previously explored, and as such, presents more opportunities for errors to arise.  The Earth object material file is a compilation of more then 25 materials, representative of the variation of the Earth's reflectance.  While the previous Earth object relied solely on a single diffuse BRDF to account for the total geometric variation in the BRDF across the entire spectrum, our Real Earth object uses spectrally varying RossLi parameters for the surface reflectance of the Earth, spectrally varying WardBRDF parameters for the cloud layer, and spectrally varying optical depth parameters for the atmosphere.

As described in the DIRSIG work flow [Sec: 4.2], our atmosphere was created using a hybridized ELM comparison between the EPIC imagery and a two layer simulations of our Earth object.  Unfortunately, there was an assumption made which turned out not to be a good assumption.  Our EPIC imagery is near bi-static, that is to say, the solar incidence angle and the measured exitance angle of the Earth is near equal. What was assumed was that if we derived RossLi parameters for the atmosphere using near bistatic ground truth, then the non-bistatic measurements of the Earthshine would still be viable - this was wrong.

The BRDF we sought to recreate was driven by a phenomenon called internal reflection.  Internal reflection is inversely analogous to what happens with transmission, the further a ray travels through a medium, the more of that ray is scattered. The effect is a growing reflectivity with depth. [Fig: 5.24].
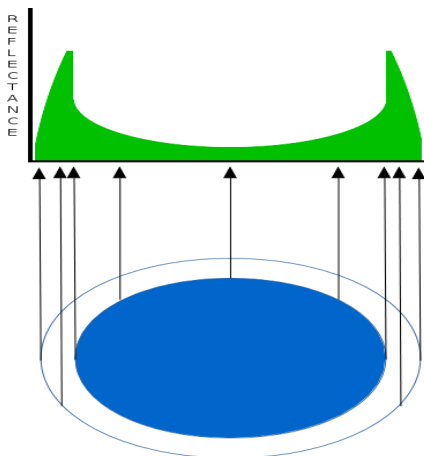
Figure 5.24: Representation of atmospheric internal directional reflectance model

The RossLi Parameters gave the illusion of doing an alright job of approximating the internal reflection of the atmosphere when compared to the EPIC ground truth. It wasn't until the RSO was moved around that it became apparent that non-bistatic reflectances were much too bright to be Earthshine. Other atmosphere reflectances were tried along with an augmentation to the emissivity profile to create an solar incident independent atmosphere, but ultimately we found ignoring the reflectance of the atmosphere worked best.

These experiments use the same characteristic RSO scenes as previously explored with the addition of Polar orbits along the Prime Meridian for the spherical RSOs, a Lon 45 flat plate RSO simulation, along with a few more out of phase flat plate RSO simulations. In addition, RSO relative views are included. One is an orthographic image of the Earth taken from an EPIC like system that shares a Latitude and SEO phase with our RSO. The other is a relative horizon to horizon wide field of view image of the Earth taken from the perspective of the RSO. These relative views are intended to give the reader an idea of how the underlying geography relates to the Earthshine. One thing to note is the horizon to horizon Earth perspective image is stretched towards the edges. This means the bump in the specular flat plate apparent magnitude plot that signifies Earthshine illumination would not directly correspond to the spatial variability of the RSO Earth Perspective Image.

The prime thing we seek to pull from this model is some insight into the RMSE of the diffuse Earth model. Because we have limited our focus to the Prime Meridial hemisphere with nadir solar irradiance incident on Lat 0 Lon 0, our determined RMSE really should not be considered a RMSE for the homogeneous Earth approximation as a whole. There are a lot of free variables not explored in this treatment: time of day dependence, seasonal dependence, weather dependence, variable

wind speed dependence (which drives variability in the ocean BRDF), and the variability in atmosphere, to name a few. At the same time, a lot of free variables are explored. We broached what we could, and maintained an expandable platform for what we could not.

### 5.3.1 Diffuse Sphere RSO

The diffuse sphere RSO serves as a look into the distribution of radiance incident into a Hemisphere. We can qualitatively tell the environmental relation between Earthshine and geography by analyzing the relation between the magnitude plot and the RSO Earth perspectives. These simulations do a full orbit about the Earth, where as, due to symmetry in the previous simulations, we only did a half rotation about the diffuse Earth approximation.

# Polar Orbit along Prime Meridian

This simulation is the first look into the variability in Earthshine for an object in a Polar orbit, more specifically in terms of coordinate locations used on July 12, 2016. For the homogeneous Earth approximations, the Equatorial and Polar orbits would have had identical solutions. The Earth on the other hand varies differently with longitude as it does with Latitude. The Earth has bright diffuse poles, and the equator is mostly dark specular water. The cloud map used in our simulations also appears to have a lot of clouds in the southern region of the Earth.
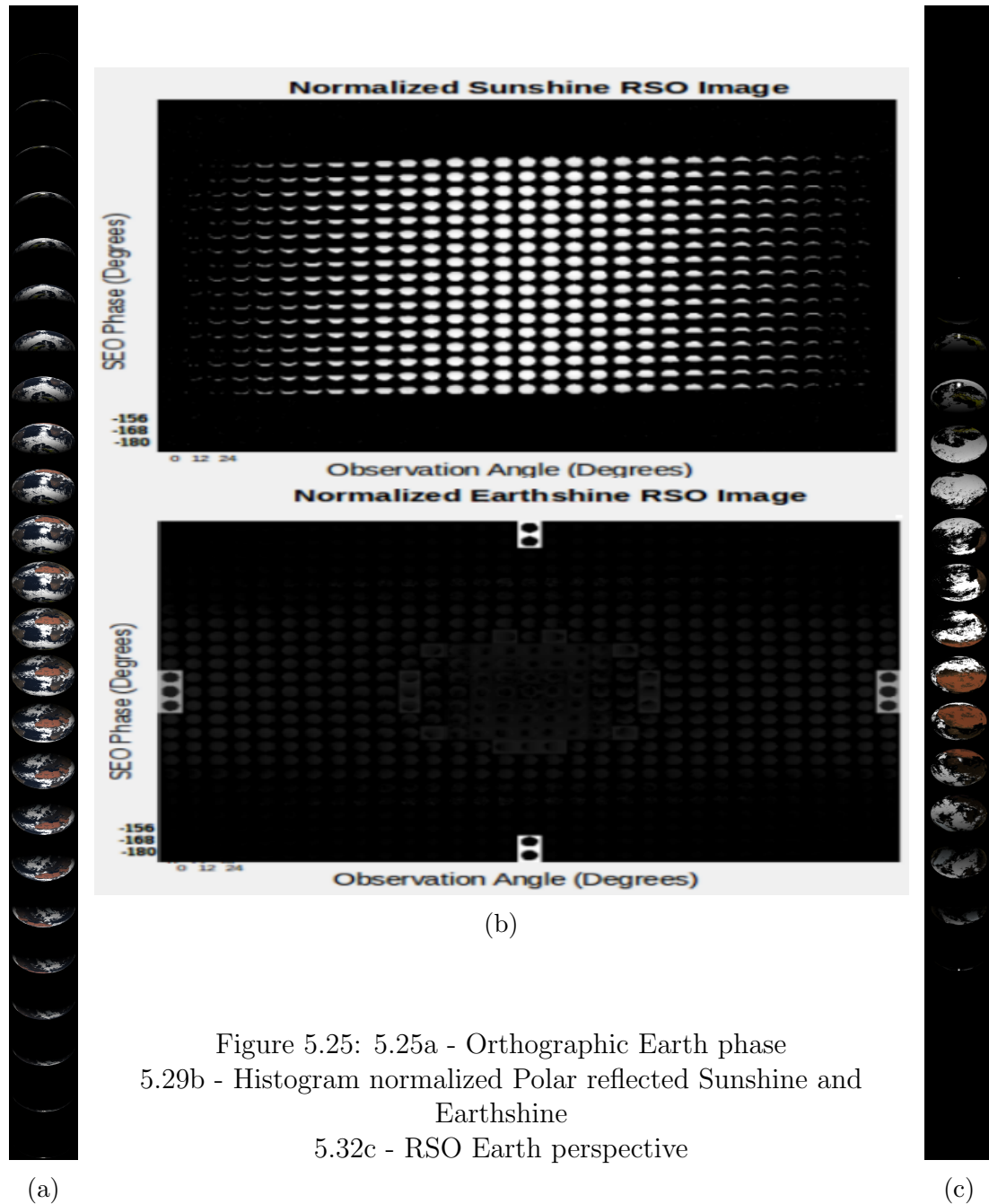
Figure 5.25: 5.25a - Orthographic Earth phase
5.29b - Histogram normalized Polar reflected Sunshine and
Earthshine
5.32c - RSO Earth perspective
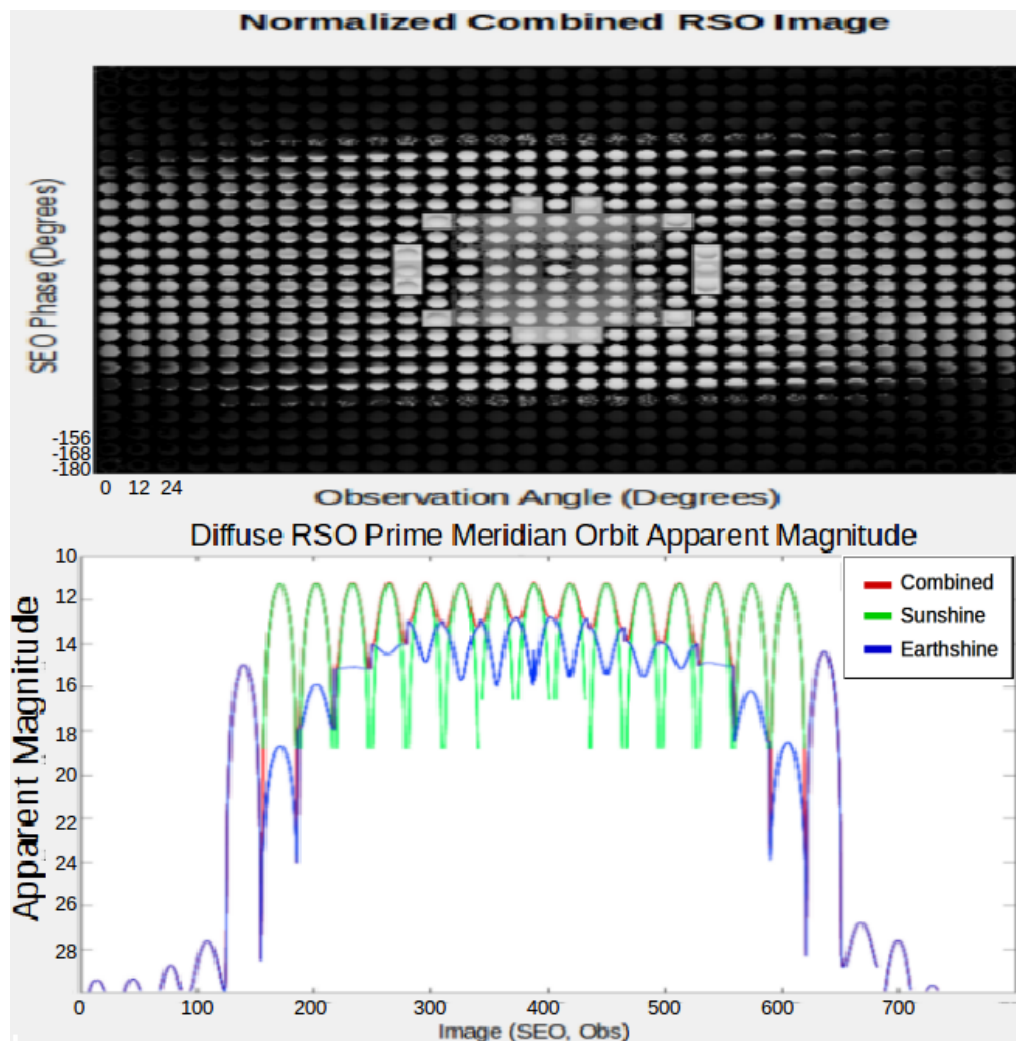
Figure 5.26: Real Earth object and diffuse RSO Polar double phase combined sources
(Top) apparent magnitudes (Bottom).

Some results of this simulation appear to indicate an issue with the Earth-
shine calculation as the RSO enters the backside of the Earth. One potential source
of error is that we have a semi transparent atmosphere, but when we subtract out
the dark Earth object, we treat the dark Earth object as large as the Atmosphere.
If the RSO geometry lines up in such a way such that solar radiation is passing
through the limb of the atmosphere and hitting our RSO, then the radiation will
appear as Earthshine in our work flow. This is of little concern to us though. The
region of space obscured by the Earth are easily identified with the Sunshine portion

of the apparent magnitude plot, and are not of any interest in our analysis.

This simulation shows a max Earthshine apparent magnitude of 12.8, this is 0.7 higher then that of the diffuse Earth model, a radiance ratio of 1.9. Checking the symmetrical relation within +/- 90 degrees Lon by matching the corresponding points from both sides of the equator, there is a RMSE of ±0.165. Matching those points to our diffuse Earth model we find a RMSE of ±0.4.

One thing that differs from the diffuse model is the distribution of magnitudes as a function of SEO angle. As the RSO comes from the South, it appears maintain a consistently brighter Earthshine then as it goes North. This is because of the cloudy southern hemisphere for the Earth object, and because there are more reflections in the Ocean. At solar incident angles close to zero there are bright objects such as clouds and the Sahara, meaning these objects are less inhibited by geometric fall off of solar incidence. The orbit also appears to go over a lot of clouds, a much brighter then average surface. Lastly, by chance, there happens to be a lot of specular reflections of the sun in the oceans. This makes for a vary large deviation in Earthshine from the diffuse Earth object approximation.

# Orbit along Equator



5.27a - Orthographic Earth phase
5.27b - Histogram normalized Equatorial reflected Sunshine and
Earthshine
5.27c - RSO Earth perspective
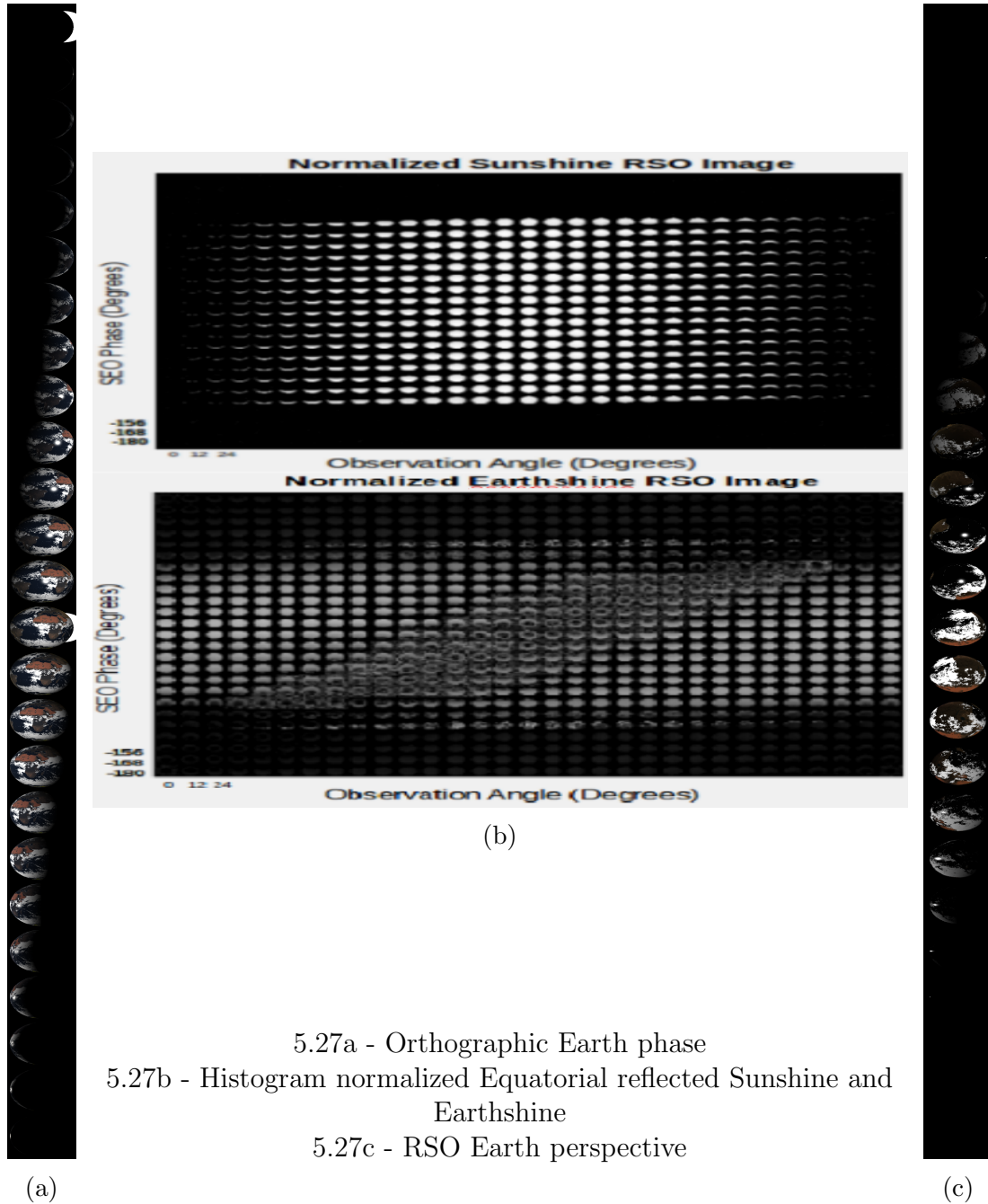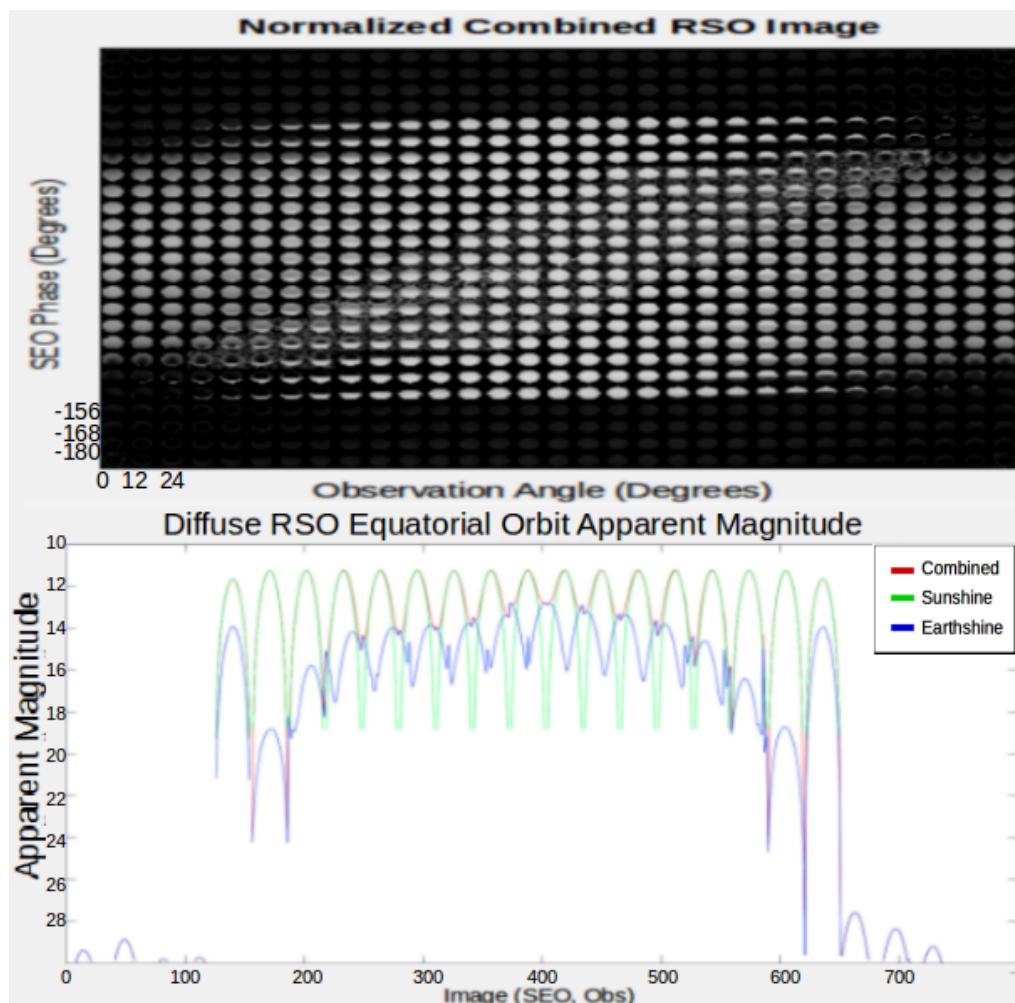
Figure 5.28: Real Earth object and specular RSO Equatorial double phase combined
sources (Top) apparent magnitudes (Bottom).

This simulation has a unique artifact, the region emblematic of past the
limb of the Earth but not in the shadow shows a smaller Sunshine peak coupled with
a regionally large Earthshine peak. This indicates that a portion of the Sunshine is
hitting the RSO through our atmosphere shell and a portion is not. This shines a
light on the relationship between the refinement of a model and the refinement of
an analysis. Our model obviously breaks down in the near Earth shadow region of
the Earth for our diffuse RSO, but because we decided this to be inconsequential
for our analysis, we accept it.

Because the RSOs both go over Lat 0 Lon 0, in our case, the brightest

spot on Earth, the model shows the same peak deviations as explored in the Prime Meridian case. The symmetric RMSE across the Prime Meridian is $\pm 0.43$. The RMSE from the diffuse Earth model is $\pm 0.4160$. In this case, a closer approximation to the Earthshine then assuming symmetry about the Prime Meridian is assuming a diffuse Earth. Another interesting thing is that the RMSE between our real Earth model and our diffuse model changes only by 0.016, the symmetric approximation on the other hand changes by 0.375.

## 5.3.2   Specular Sphere RSOs

The heterogeneity of the real Earth can cause a much different relationship between diffuse and specular RSOs then in the homogeneous model. Because the RSO is spherical, the same portion of the Earth is reflected towards the imaging systems as would be with the diffuse. Though, using the specular sphere, only directional radiance is reflected towards the system, where as the diffuse RSO has a cosine weighted averaging. We can expect solar glints in the ocean to add a significant amount of error. Though, it may prove difficult to distinguish them in the apparent magnitude plots because the all of directional radiance presents itself with a similar issue.

# Polar Orbit along Prime Meridian



(b)

5.29a - Orthographic Earth phase
5.29b - Histogram normalized Polar reflected Sunshine and
Earthshine
5.32c - RSO Earth perspective

(a)

(c)
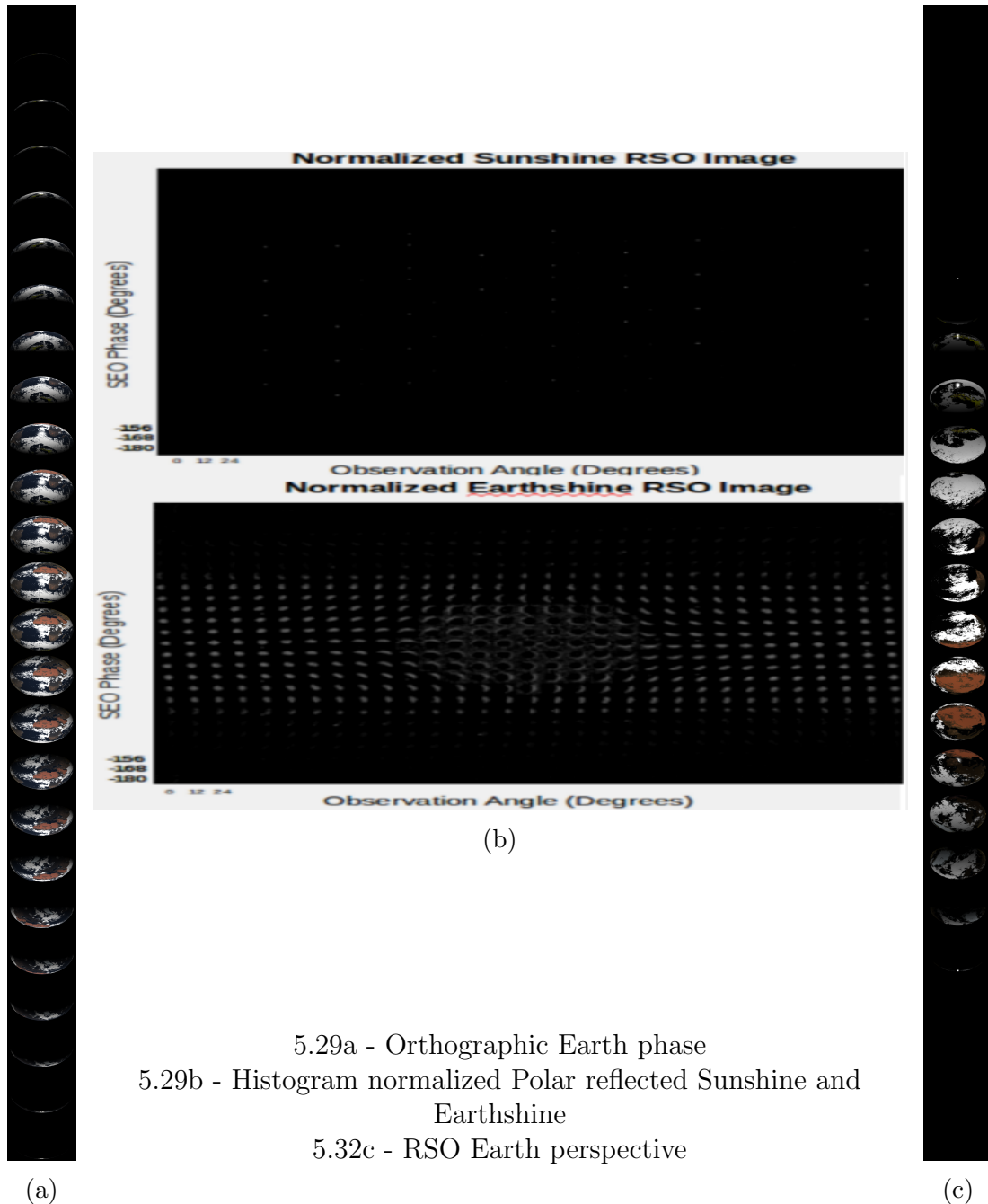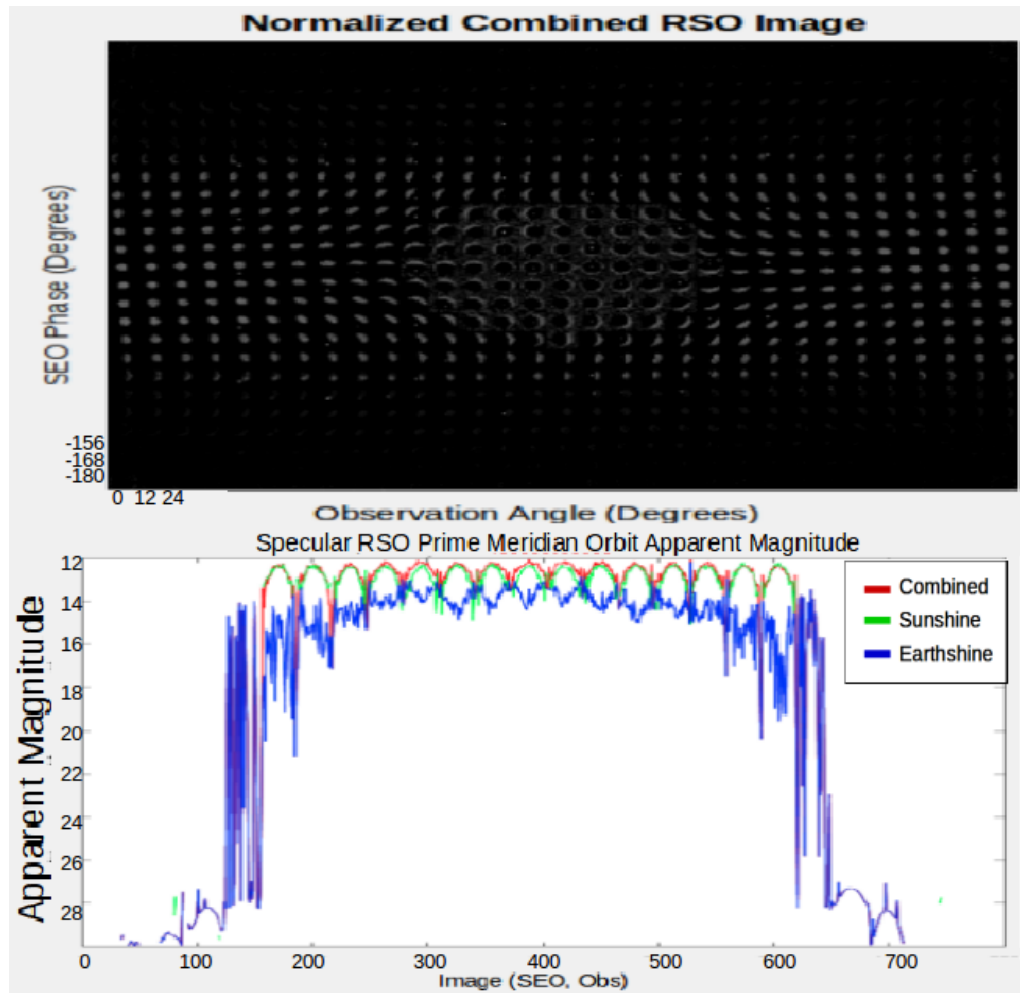
Figure 5.30: Real Earth object and specular RSO Earth Polar double phase combined sources (top) apparent magnitudes (bottom)

The first thing that should be evident is the apparent increase in noise in this simulation when compared to the previous simulation or even the specular RSO diffuse Earth model.  This is because of the we are now analyzing the directional radiance of Earthshine.  There is still evident structure in our results.  The periodicity is observable and the approximate peaks can be determined.
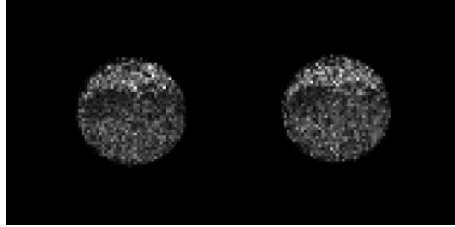
Figure 5.31: Simulated images 405 and 406 Earthshine illumintated specular RSO
compare

As can be seen in our consecutive images [Fig: 5.31], there is a macro distribution
difference consistent with the change in the SOO, but the micro distribution is not
quite consistent with this. This brings us back to approximating surfaces with micro-
heterogeneity as macro-homogeneous surfaces or FOHS, which is what the diffuse
Earth model does. Because the reflected GSD of our system is very small, the micro
heterogeneity shows through.

Ignoring outliers, we get a max apparent magnitude of 12.85, just 0.05
dimmer then that of the diffuse sphere model. Though, in this case the max is
15° off nadir, showing an instance when a sampling of directional radiances did not
match mean radiance. Comparing the same peaks as explored in the diffuse RSO
simulation we find a RMSE of ±0.306 across the equator. This is based solely on
the local peak maximums and are not necessarily spatially correlated to the same
SOO angle, where as the diffuse model has that inherently the case. The maximum
apparent magnitude deviation between the diffuse Earth model and the real Earth
model is 1.09. This amounts a radiance ratio of 2.73. This not only points out the
potential importance of a heterogeneous model, but also in the difficulty in making
one using DIRSIG.

# Orbit along Equator
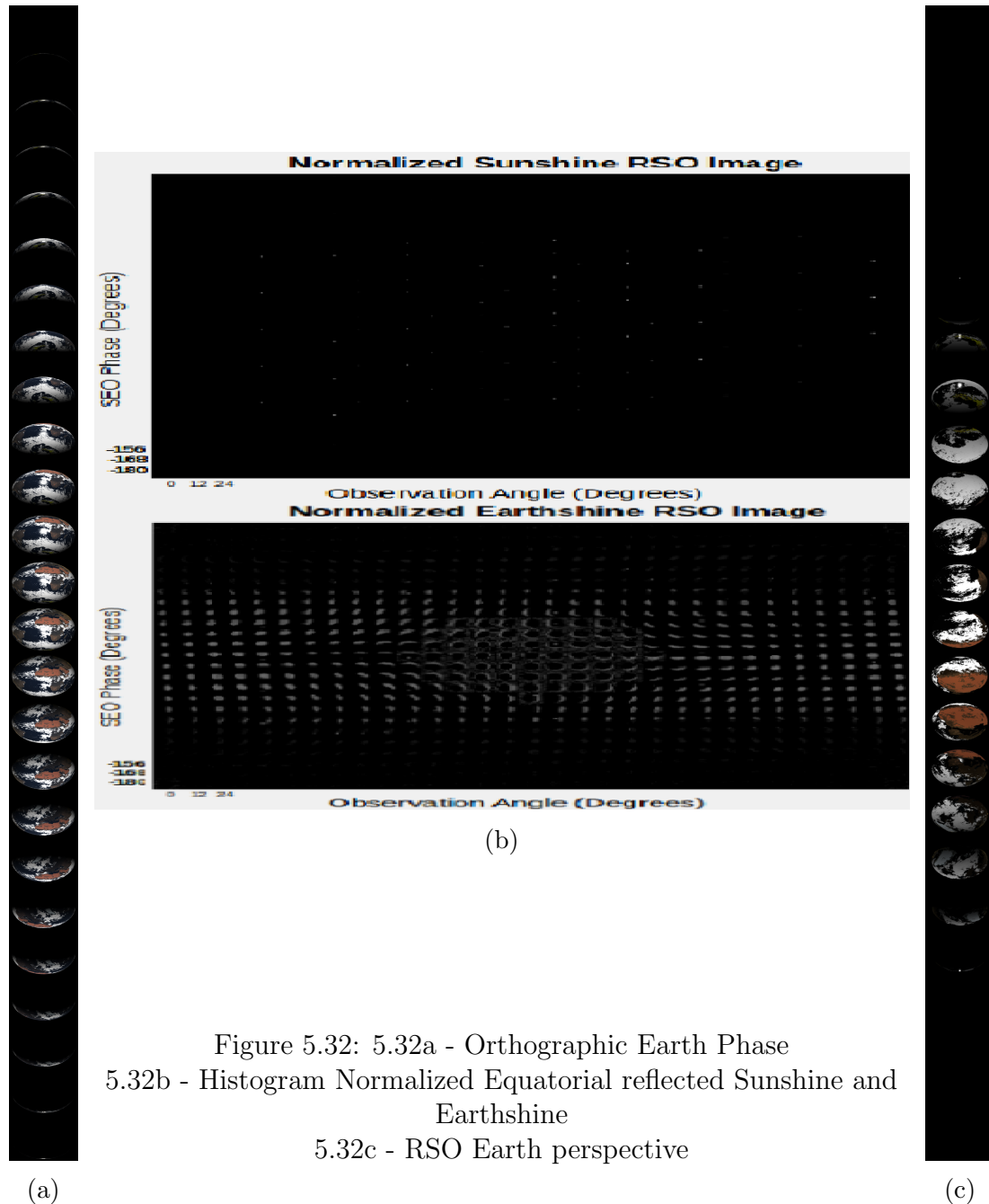


Figure 5.32: 5.32a - Orthographic Earth Phase
5.32b - Histogram Normalized Equatorial reflected Sunshine and
Earthshine
5.32c - RSO Earth perspective
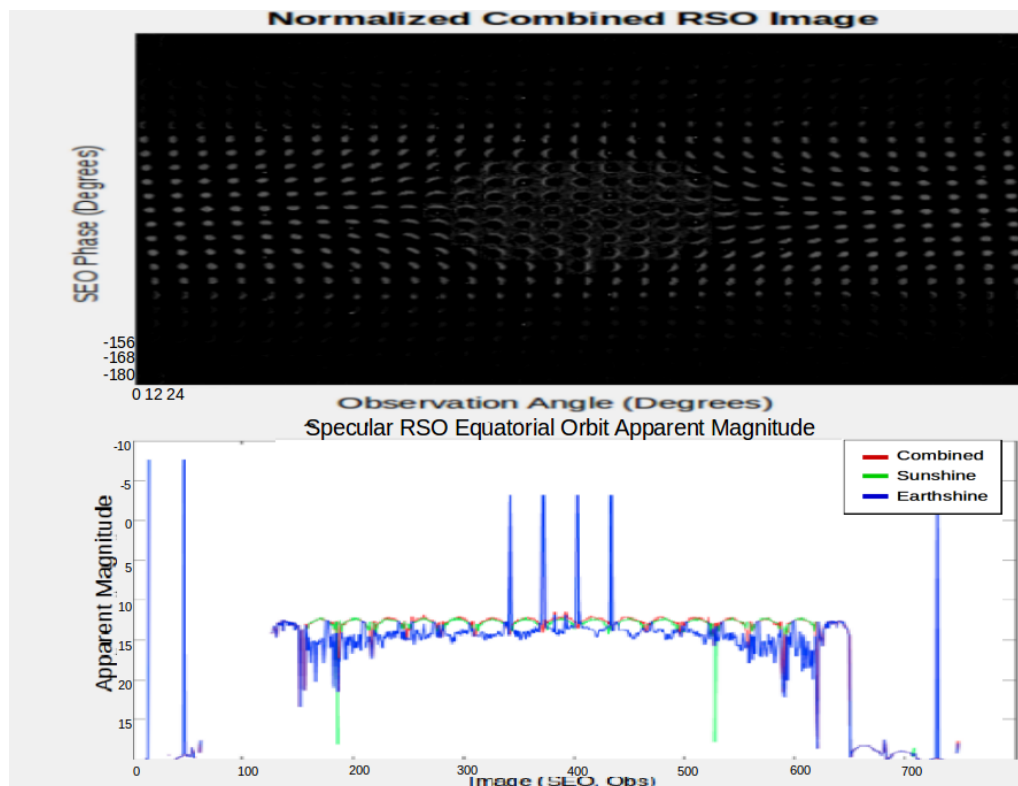
Figure 5.33: Real Earth object and specular RSO Earth Equatorial double phase
combined sources (left) apparent magnitudes (right)

A reoccurring error throughout the implementation of our Real Earth
model is that often entire swaths of images would not generate. Exactly where
this bug stems from is still being explored. For this result we were able to create the
double phase plots, but were unable to get the values for a portion of the RSOs orbit
in the shadow of the Earth. Fortunately because we have limited our spherical RSO
analysis to +/- 90 degrees, it does not effect out results. As can be seen, there is the
same sort of noise as in the previous simulation. More interesting is the total solar
Irradiance in the near Earth shadow limb is completely calculated as Earthshine,
while prior it was mostly calculated to be Sunshine. This is because the portion of
the RSO that is sun illuminated is being reflected away from the observatory.

In order for an observatory to see a ray cast by a source on a specular
spherical RSO, the incident and exitant rays need to be equal relative to the normal
of a surface of the RSO (Specular Sphere Criteria). The ray is only scaled by
the projected area and a portion of the RSO unable to be seen due to the small
area that meets the specular sphere criteria. The result is that more oblique SOO

contribute more to the apparent magnitude then it's diffuse counterpart, where the ray is scaled by geometric fall off and projected area. At small SOO the diffuse RSO is brighter because the directional radiance that doesn't meet the specular sphere criteria still contributes to the apparent magnitude of a diffuse RSO. But as the SOO become more oblique, the geometric fall off coupled with the projected area dominates. Though this is a double edged sword.

Ultimately, it is shown that for specular spherical RSOs, Earthshine is going to not contribute much. This is because, except at very small SOOs, the sun is going to be able to be seen in the reflectance of the RSO with only geometric fall off. Since Sunshine and Earthshine are typically out of phase, the same time the diffuse sphere is brightest the solar radiation is mitigated by the double fall off.

Ignoring outliers, we get a max apparent magnitude of 13.57. This is 0.72 dimmer then the previous simulation. The symmetric RMSE about the Prime Meridian is ±0.53 and the RMSE from the diffuse model is ±0.416. This model appears to have been more consistent with expectation. It was much dimmer then the other model, which indicates a much dimmer distribution of direction radiance along the equator. Both models maintained the consistency of falling off much slower on the limbs then their diffuse counter part. Ultimately, the specular spherical RSO simulations are a little too noisy between measurements to try and make conclusive extrapolations as refined as their diffuse counterparts. It does seem, judging by the inherent structure, that the plot would quickly smooth out with an increase in sampling. However, this is beyond the scope of this paper.

### 5.3.3 Diffuse Flat Plate RSO

This suite of flat plate simulations allows use to examine how facet illumination changes with orientation. One of the benefits of the flat plate simulations is heterogeneity of the facet projection onto the focal plane. That is to say that the flat RSO allows for more consistent ray tracing. The diffuse flat plates makes the heterogeneity of the Earth much less apparent, and should result in a smooth relationship between orientation and apparent magnitude, and a small RMSE between our diffuse Earth model and our real Earth model. For our specular RSO we expect a much less smooth relationship and a large RMSE.

Our results are presented in a similar fashion as is presented in the diffuse Earth models, with the addition of orthographic phase images and RSO perspective plots. The approximately 180 degrees that make up a cycle of the Earthshine curve from left to right corresponds to the normal of the flat plate being 90 to -90 degrees out of phase with the center of the of the RSO perspective image from right to left. This is not apparent with the diffuse RSOs, but is with the specular.

**Rotating Flat Plate Lat 0 Lon 0 Obs 0**
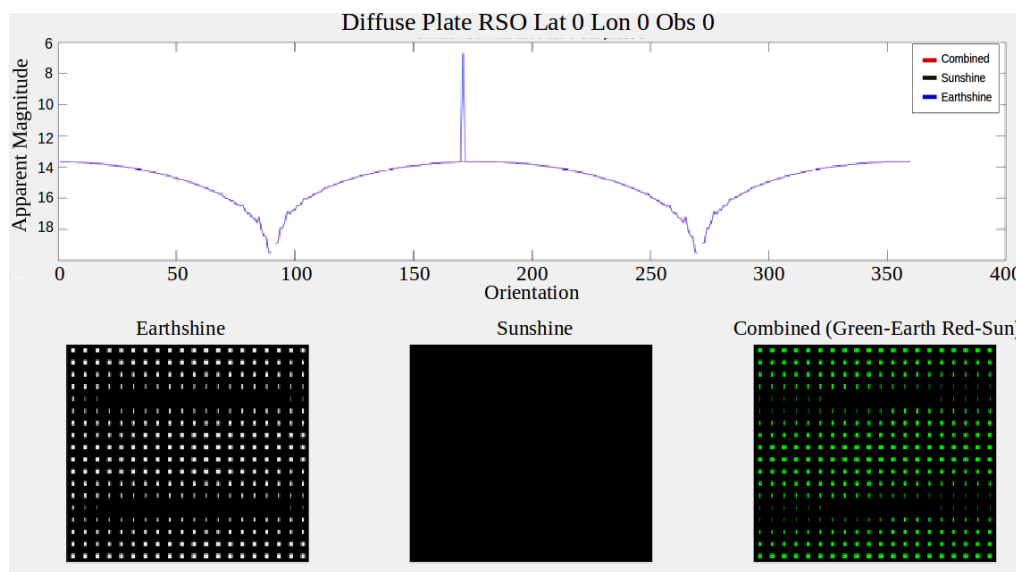


Figure 5.34: Real Earth diffuse flat plate Lat 0 Lon 0 Obs 0

## Rotating Flat Plate Lat 0 Lon 0 Obs 90
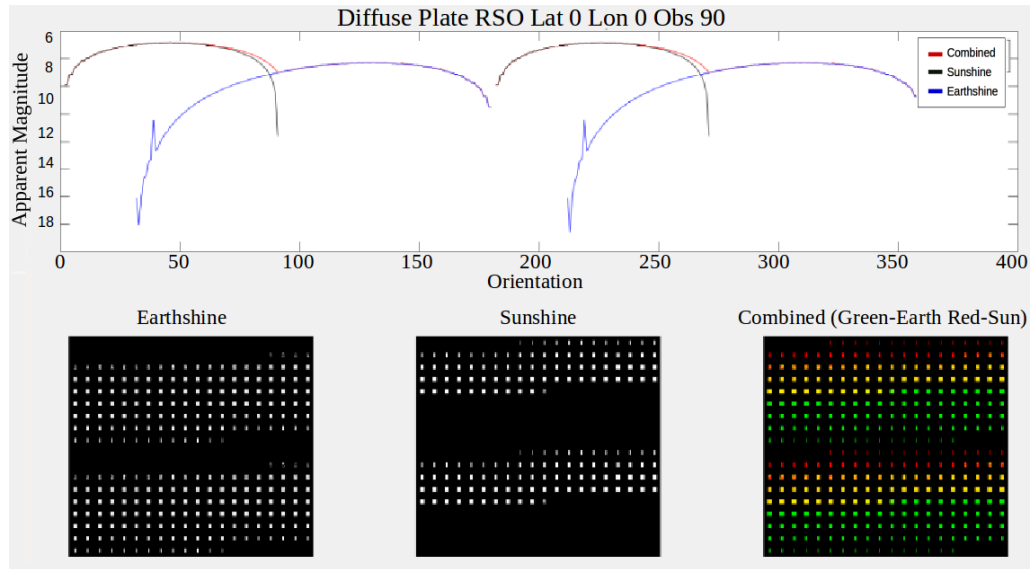


Figure 5.35: Real Earth diffuse flat plate Lat 0 Lon 0 Obs 90

## RSO Relative Earth Views
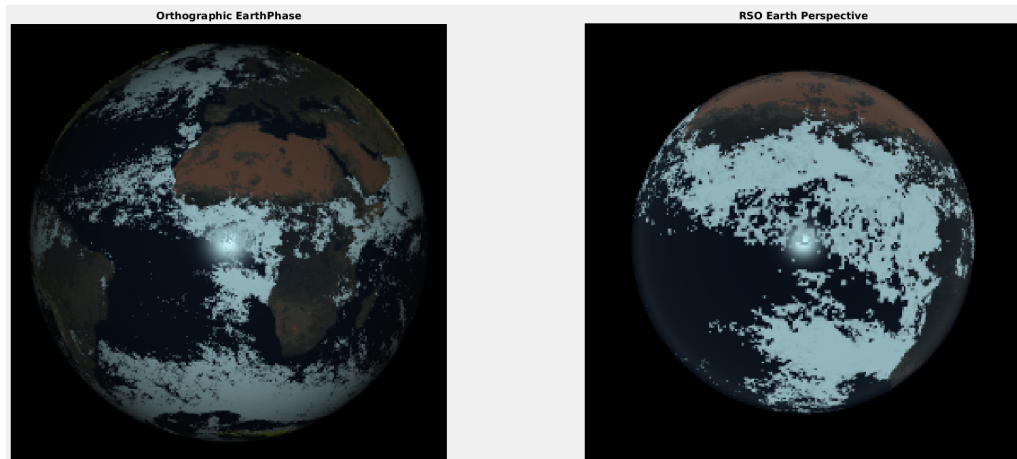


Figure 5.36: Lat 0 Lon 0 Obs 90 orthographic perspective view (left) RSO perspective view (right)

With our observatory on the solar axis, we see a peak emblematic of the
background Sunshine with an SOO of 90 degrees. Other then that it behaves like
we'd expect in both cases.

For an SOO of 0 degrees we find a max apparent magnitude of 13.69,
compared to our max of 14.427 for our diffuse model. This is a radiance ratio of 2.
While this does seem high, it is possible. The reflectance of our clouds at their max
is nearly 0.9, three times that of the diffuse model. Given that the RSO perspective
has a lot of dense clouds in it, coupled with a solar reflection off the ocean, this value
is possible. Given a lower altitude it is easy to imagine how the radiance ratio could
be closer to 3 in extreme conditions. We find a RMSE of ±0.74 between the diffuse
Earth model and the real Earth model. This seems consistent with the separation
of the max.
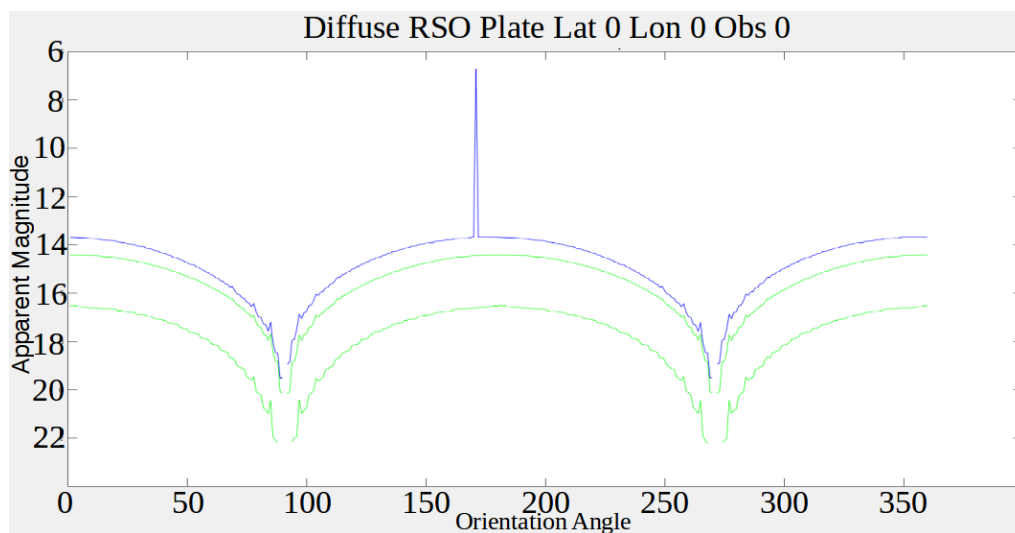


Figure 5.37: Comparison between SOO-0 Lat 0 Lon 0 of diffuse Earth model (mid-
dle), specular Earth model [Not included in analysis] (bottom) , and real Earth
model (bottom).

With the SOO of 90 degrees we see a maximum apparent magnitude of
14.22, compared to a apparent magnitude of 15.12 for the diffuse model. This is a
radiance ratio of 2.1, consistent with the last observation. The RMSE between the
two models is ±0.82%.
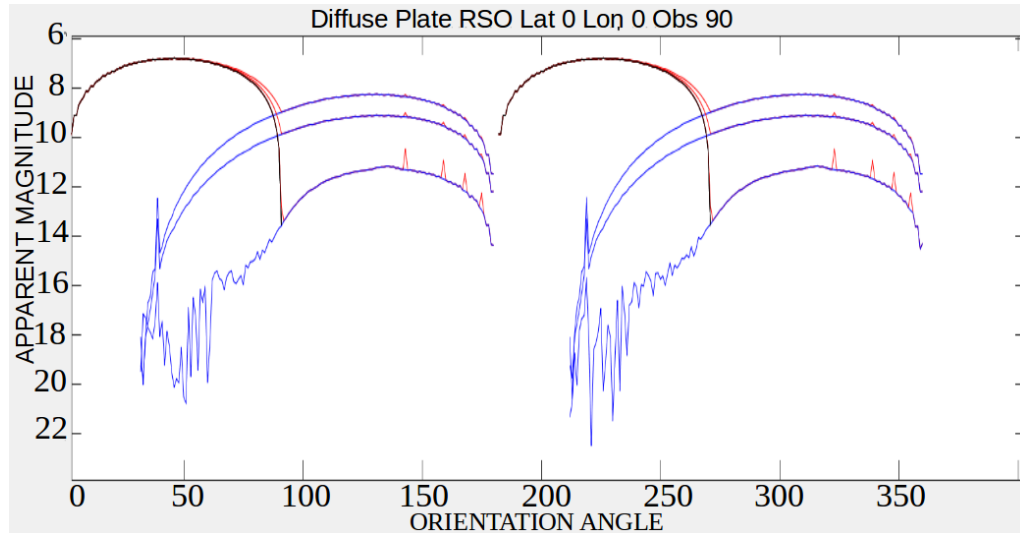
Figure 5.38: Comparison between SOO-90 Lat 0 Lon 0 of diffuse Earth model (Top), specular Earth model [Not included in analysis] (bottom), and real Earth model (middle).

We expected for the diffuse flat plate RSOs less error because of the cosine weighted averaging that happens with the diffuse materials. But in our case, the averaging is only occurring in a small region, in which we have a population of brighter then average Earth surfaces.

## Rotating Flat Plate Lat 0 Lon 45 Obs 45
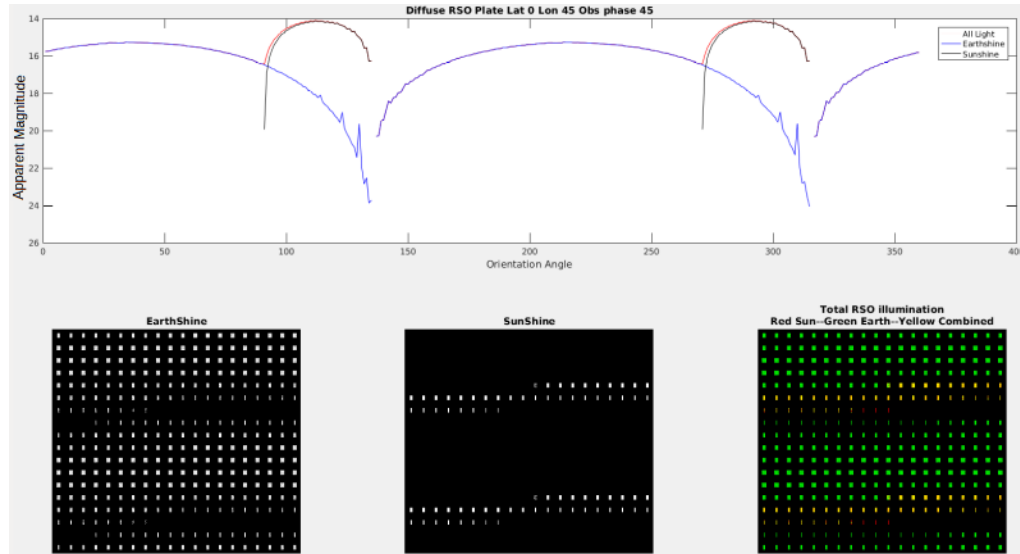


Figure 5.39: Real Earth diffuse flat plate RSO Lat 0 Lon 45 Obs 45

## RSO Relative Earth Views
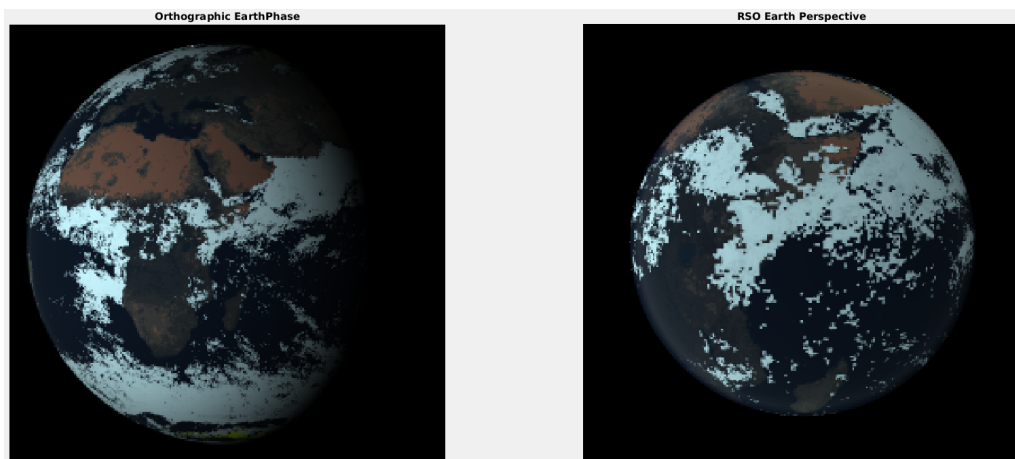


Figure 5.40: Lat 0 Lon 45 Obs 45 orthographic perspective view (left) RSO perspective view (right)

## Rotating Flat Plate Lat 0 Lon -45 Obs -45
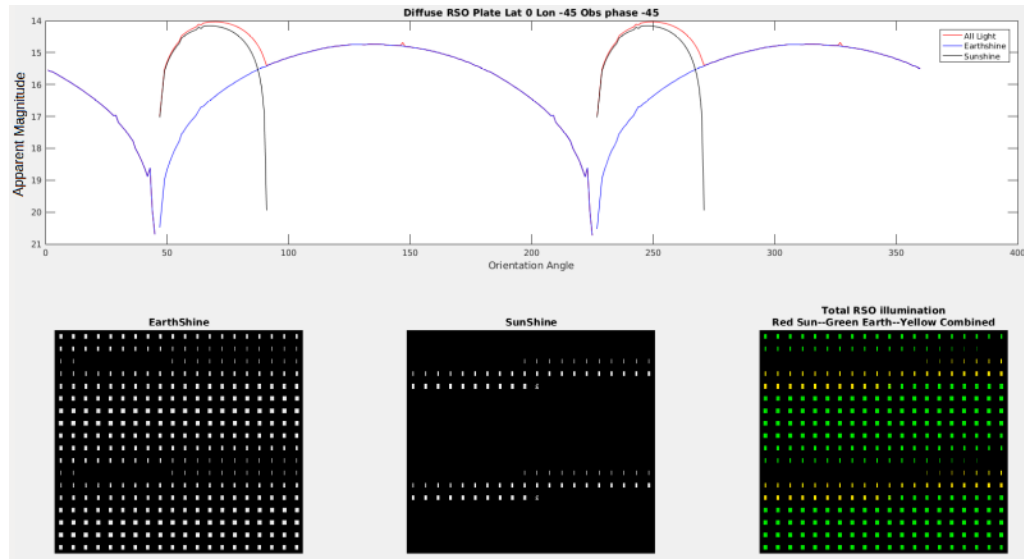


Figure 5.41: Real Earth diffuse flat plate RSO Lat 0 Lon 45 Obs 45

## RSO Relative Earth Views
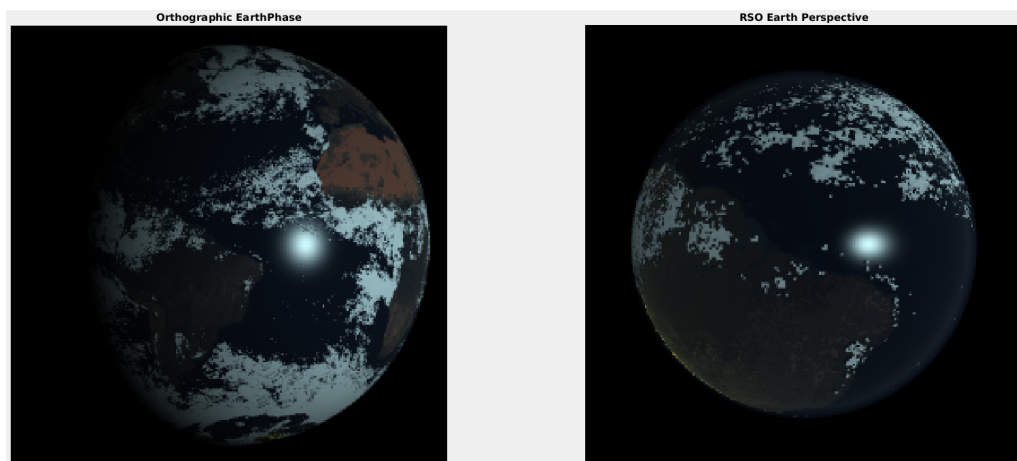


Figure 5.42: Lat 0 Lon -45 Obs -45 orthographic perspective view (left) RSO perspective view (right)

These simulations lack a diffuse Earth analogy and were incorporated for
an understanding of the longitudinal dependence. One thing to note is that while the
orthographic phase image shows a portion of the Earth dark, the RSO perspective
image shows only an illuminated Earth subsample.
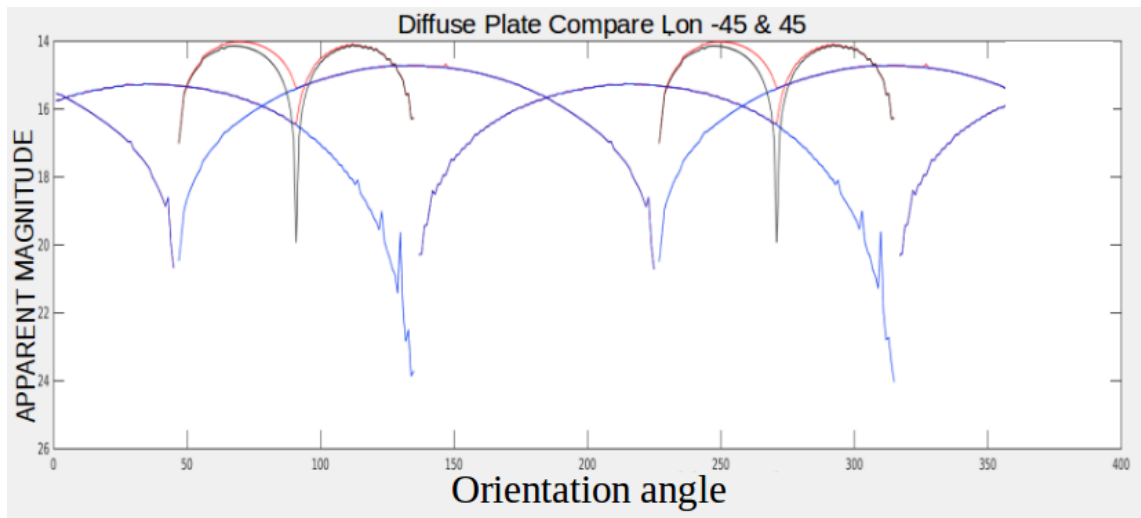


Figure 5.43: Real Earth flat plate comparison Lon 45 (dimmer curve) to -45 (brighter
curve) comparison

With the Lon of 45 we see a max apparent magnitude of 14.73, compared
to the Lon of -45, where the apparent magnitude is 15.25. This is a radiance ratio
of 1.58%. This seems to be somewhat consistent with what the RSO perspectives
show. While we have no direct homogeneous model examples to compare it to,
the Earthshine from a diffuse object scales with the cosine of the solar incidence.
A rough approximation is scaling the radiance by cosine of the Lon, giving us an
apparent magnitude of 15.01. This amounts to a radiance ratio of 1.29 and 1.24
respectively.

## Rotating Flat Plate Lat 0 Lon 90 Obs 90
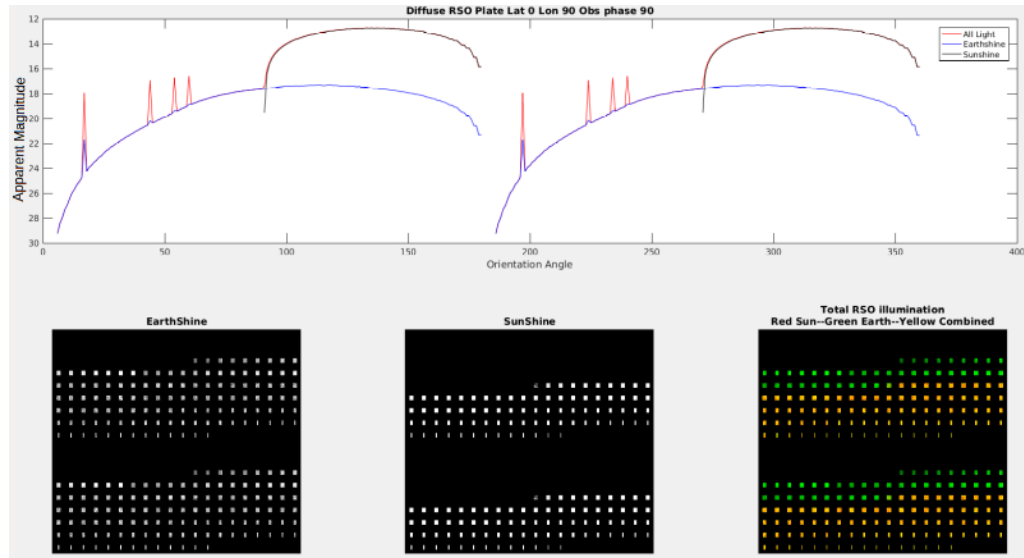


Figure 5.44: Real Earth diffuse Flat Plate Lat 0 Lon 90 Obs 90

## RSO relative Earth views
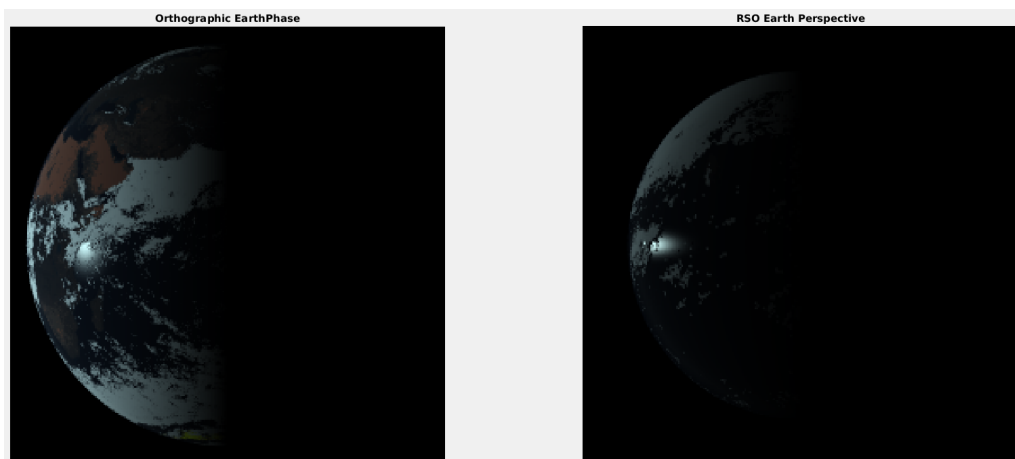


Figure 5.45: Lat 0 Lon 90 Obs 90 orthographic perspective view (left) RSO perspective view (right)

## Rotating Flat Plate Lat 0 Lon -90 Obs -90
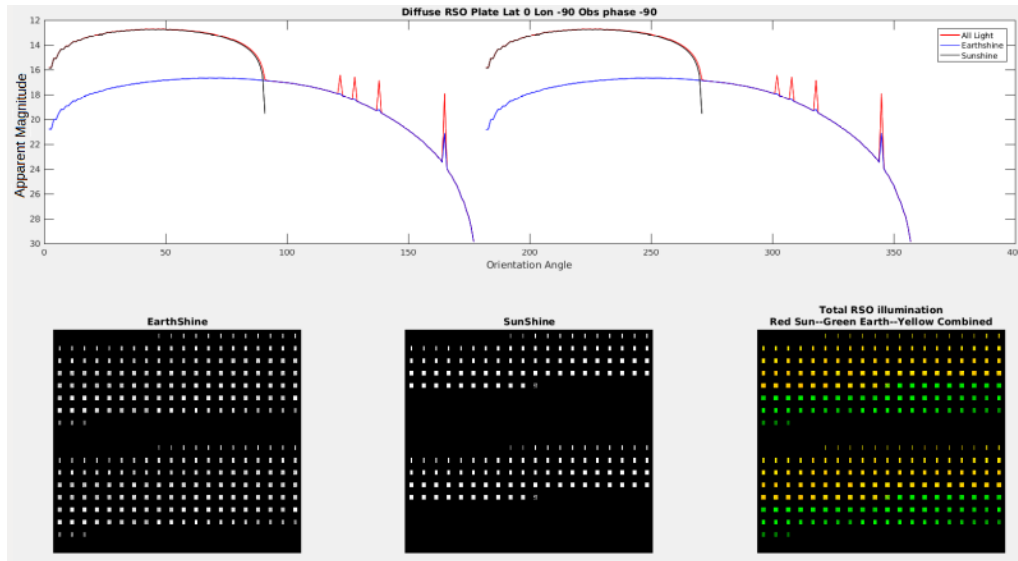


Figure 5.46: Real Earth diffuse Flat Plate Lat 0 Lon -90 Obs -90

## RSO Relative Earth Views
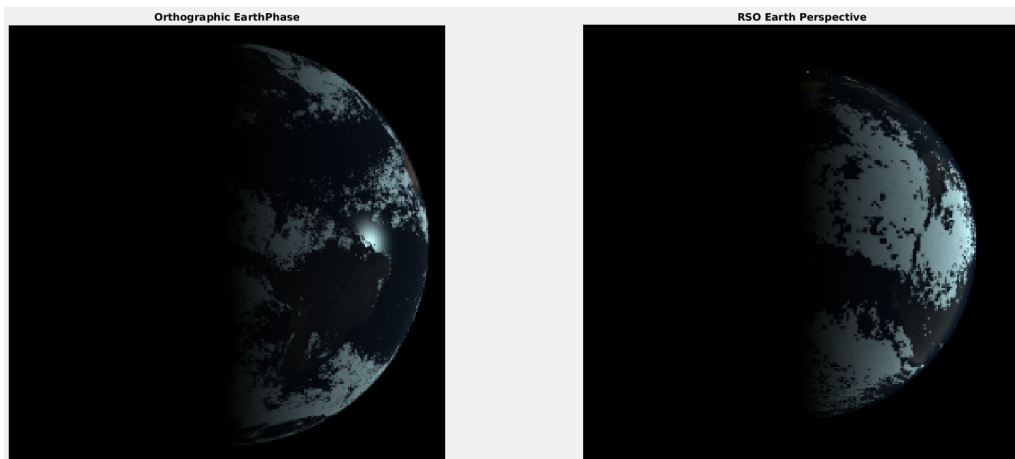


Figure 5.47: Lat 0 Lon -90 Obs -90 orthographic perspective view (left) RSO perspective view (right)

These simulation behave as we would expect.  The Lon of -90 simulation
has an apparent magnitude max of 16.69, where as the Lon of 90 has an apparent
magnitude of 17.52, a radiance ratio of 2.15.  This is congruent with the RSO
perspective images.  The diffuse model shows a maximum apparent magnitude of
17.5, a radiance ratio of 2.1 and 1.02 respectively.  Corresponding to a RMSE of
±0.83 and ±0.1810 respectively.

Though the RSO perspective of the Lon 90 RSO appears to be signifi-
cantly less bright, some of that is actually an illusion caused by the normalization.
The reflection of the sun in the ocean falls off significantly slower then that of the
geometric fall off of the clouds.  So while the scene is mostly populated with dark
objects, it is able to stay nearly as bright as the diffuse model.
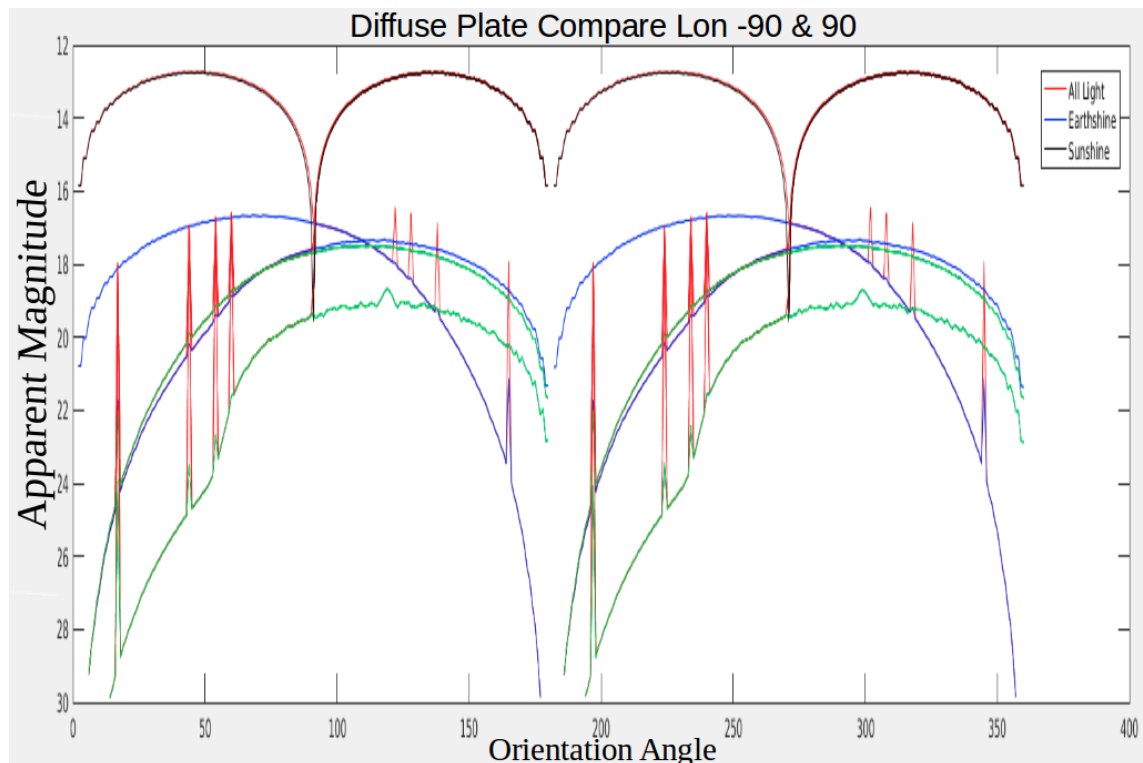


Figure 5.48: Real Earth Lon -90 (blue - top) Lon 90 (blue - bottom), diffuse Earth
(green - top), specular Earth [Not included in analysis] (green - bottom)

A dip can be seen in the Lon of 90 simulation - around the orientation

115

angle of 55 degrees. Interestingly, the same bright artifacts appear in the Lon of 90 and the two homogeneous simulations around 20, 45, 55, and 60 degree orientations angles. Those artifacts appear in the Lon of -90 simulation as well, but as if the Earthshine curves have been flipped about the 90 degree orientation mark, as in equidistant from an orientation of 180 degrees as the -90 degrees is from 0 degrees. It appears to be Earth object independent, which leaves only the potential for an issue with our RSO generation or DIRSIG lighting artifacts.

We expected the diffuse flat plate RSOs to behave similiary with both the diffuse model and the Real Earth model. While structurally they were similar, they had no consistent RMSE between models and a radiance ratio of up to 2.1. This shows how at the macro sampling size of the RSO perspectives, the Earth is still very heterogeneous.

## 5.3.4 Specular Flat Plate RSO

This collection of specular flat plate RSO simulations serve as a look into how directional illumination varies as a function of surface material properties. The specular RSO maybe adversely effected by Oblique reflection errors due to problems with material approximations using RossLi over a couple degrees on the edges of our Earthshine curves. This suit is of particular interest because it is expected to reveal where the extremes of Earthshine variability.

### Rotating Flat Plate Lat 0 Lon 0 Obs 0
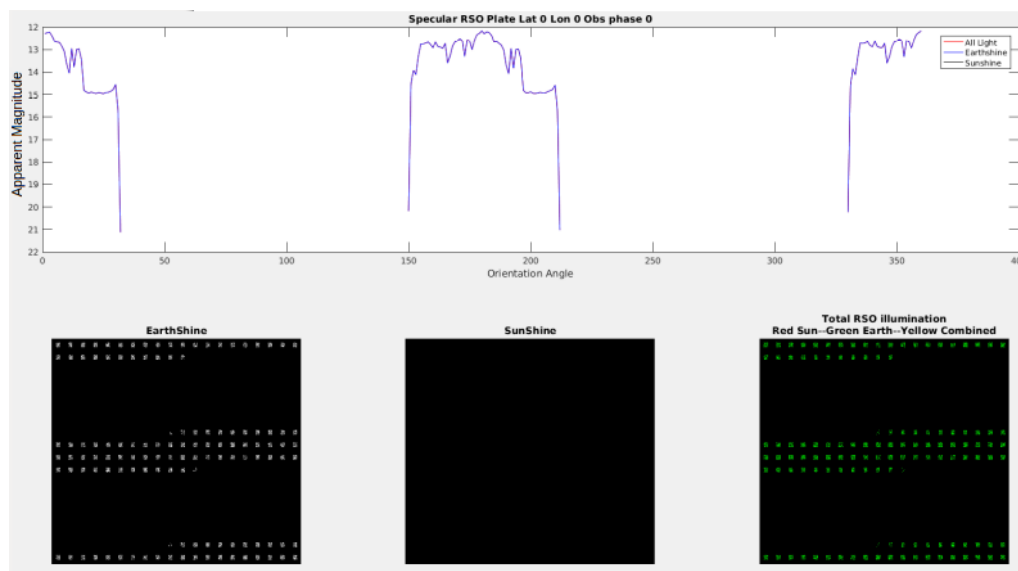


Figure 5.49: Real Earth specular flat plate Lat 0 Lon 0 Obs 0

### Rotating Flat Plate Lat 0 Lon 0 Obs 90
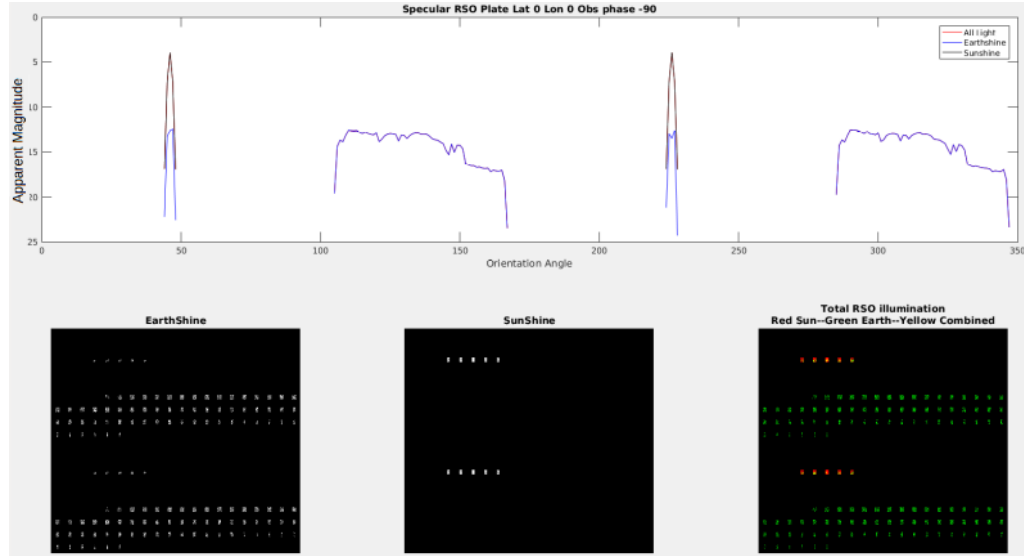
Figure 5.50: Real Earth specular flat plate Lat 0 Lon 0 Obs 90

## RSO Relative Earth Views
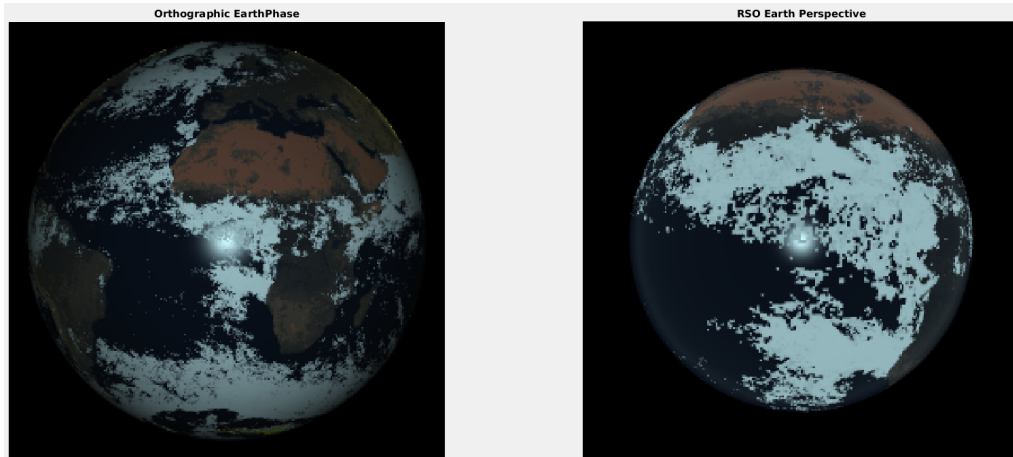


Figure 5.51: Lat 0 Lon 0 Obs 0 orthographic perspective view (left) RSO perspective
view (right)

The portion of the Earth being reflected into the direction of the virtual
sensor is a thin strip perpendicular to the vertical center of the RSO perspective
image. At the beginning of the Earthshine curve (150 degrees for Obs 0, 105 degrees
for the Obs of 90), the RSO normal is oriented towards the right most side of the
Observable Earth in the RSO perspective image. Increasing the RSO Orientation

angle corresponds to going left across the RSO perspective image. The wide field of view of our imaging system creates an elongation of the Earth on the edges, this is exemplified in the stretched ocean glint in the previous RSO perspective image of Lat 0 Lon -45 Obs -45 degrees. The RSO perspective image does not have a 1 to 1 spatial relation to the RSO Orientation angle.

This simulation matches our expectations very closely. As can be seen, the brightest portion of the measured Earthshine is in the center of the Earth, where there is a partial specular glint from the ocean. The darkest portion corresponds to a diffuse reflection from the ocean. The measured Earthshine changes as expected between the an Obs angle of 0 and 90 degrees, with a 45 degree shift and a skew favoring the an acute SOO phase. When compared to the homogeneous Earth models, all of the characteristic phenomenology is encapsulated.
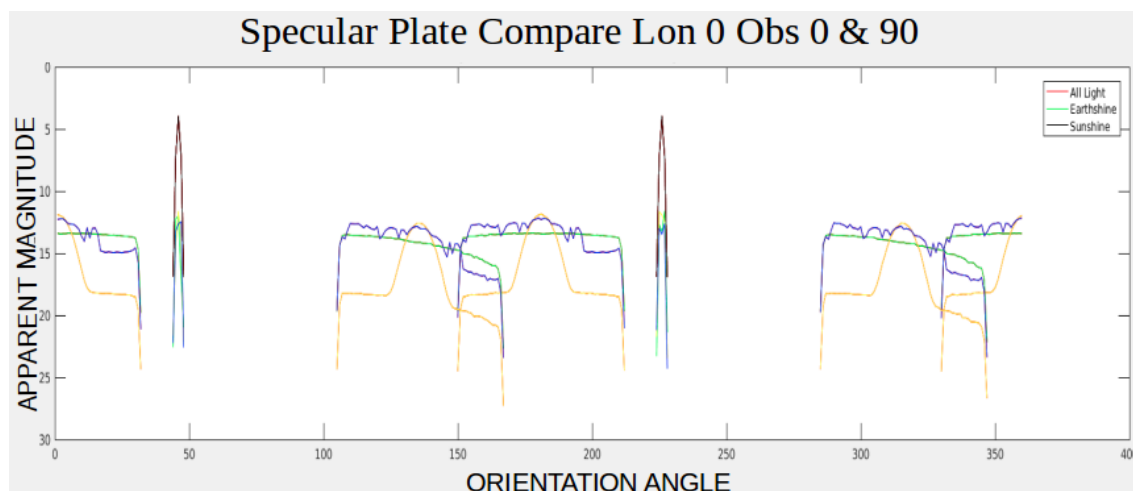


Figure 5.52: Real Earth Lon 0 Lat 0 Obs 0 (centered at 180) and Lon 0 Lat 0 Obs 90 (centered at 135) comparison of real Earth (blue) homogeneous specular Earth [Not included in analysis] (yellow) and homogeneous diffuse Earth(green) models

The max Earthshine of the Lat 0 Lon 0 Obs 0 is 12.17. The next largest source emanating from the bright diffuse clouds is 12.53. When compared to its diffuse Earth counter part of 13.38, we see a radiance ratio factor of 2.2. This seems reasonable due to the correspondence to the average albedo of the Earth, and the high albedo of clouds. There is a max apparent magnitude of 12.6 in our Obs 90 simulation. When compared to the max of the diffuse model of 13.5, we see a

radiance ratio of 2.75. We see a RMSE of $\pm 0.8275$ and $\pm 0.8565$ between the two simulations and the diffuse model respectively.

The largest discrepancy comes from approximating the ocean as a 0.3 diffuse reflector around the orientation angle of $200degrees$, with a radiance ratio of 3.44. It being larger makes sense, if anything it should be even larger. If it was in fact only reflecting the ocean, then a magnitude closer to that of the low portions of the specular Earthshine curve would be expected. With a radiance difference of 2000%, it stands to reason that there is more being reflected then just this. One factor is the projection of the BRDF on the edge of the Earth is larger then the center, so some of the near equatorial clouds on the minus Lon side of the Prime Meridian are actually near the center of the Gaussian that makes up the RSO BRDF.

## Rotating Flat Plate Lat 0 Lon 45 Obs 45
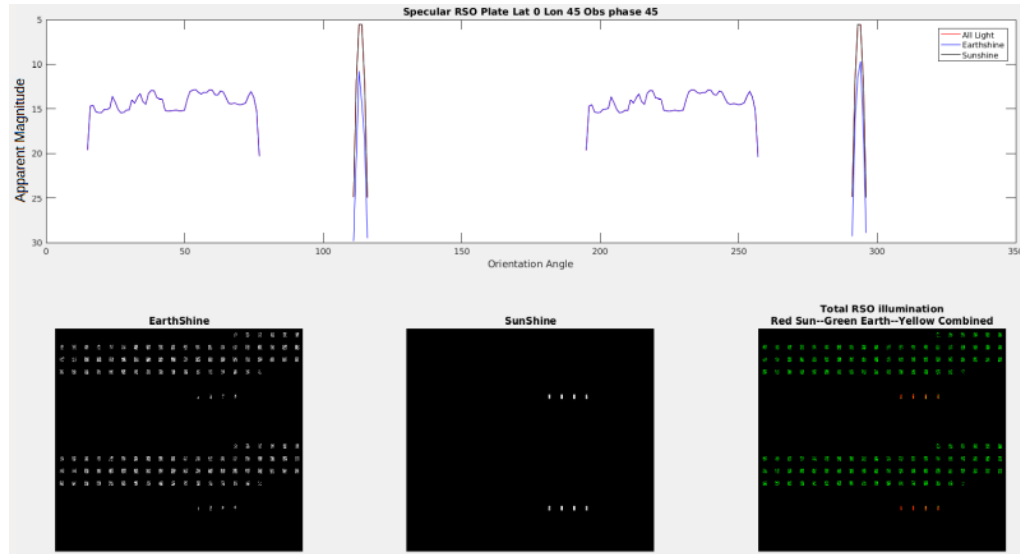


Figure 5.53: Real Earth specular flat plate Lat 0 Lon 45 Obs 45

## RSO Relative Earth Views
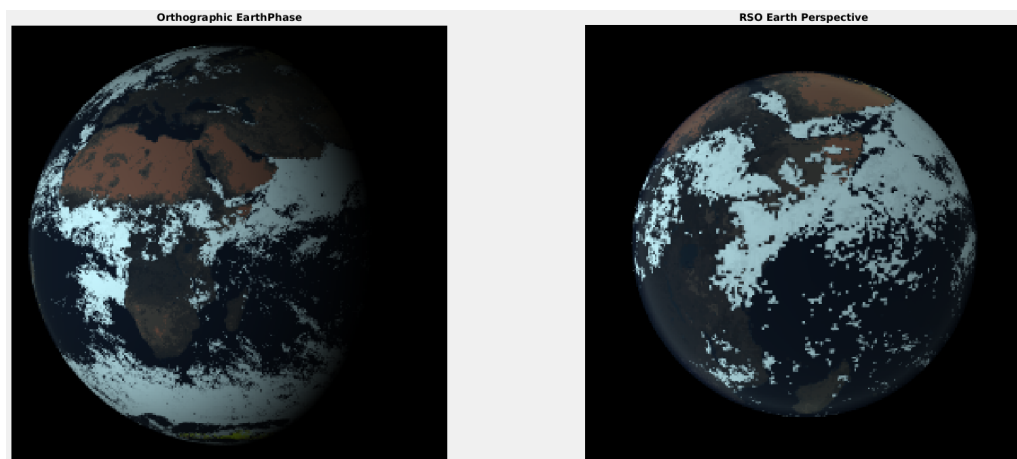


Figure 5.54: Lat 0 Lon 45 Obs 45 orthographic perspective view (left) RSO perspective view (right)

## Rotating Flat Plate Lat 0 Lon -45 Obs -45
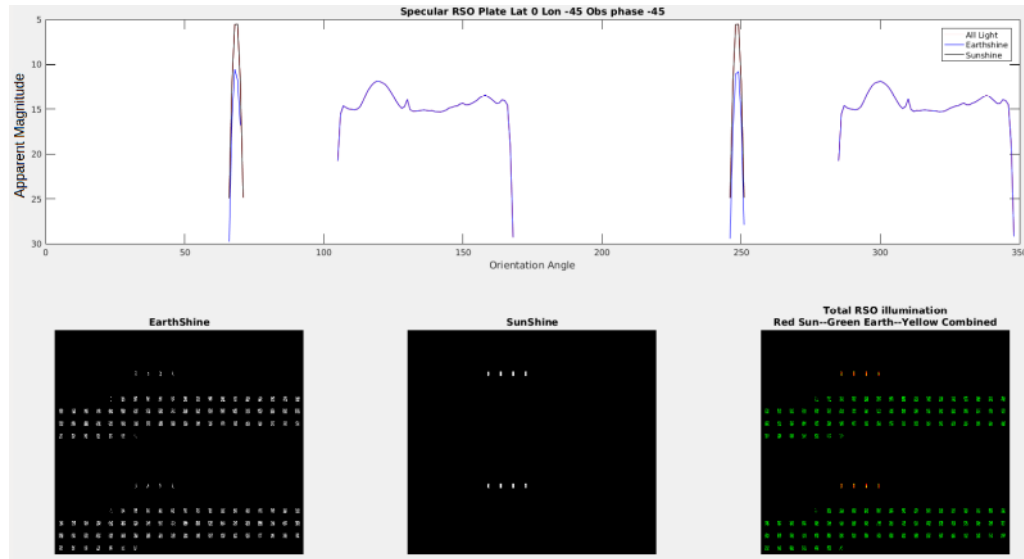


Figure 5.55: Real Earth specular flat plate Lat 0 Lon -45 Obs -45

## RSO Relative Earth Views
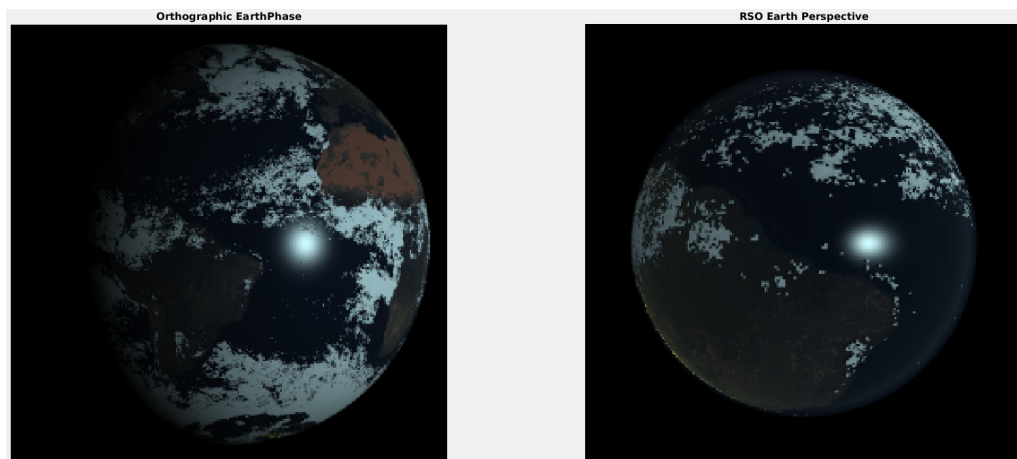


Figure 5.56: Lat 0 Lon -45 Obs -45 orthographic perspective view (left) RSO perspective view (right)

We see an apparent magnitude max of 12.84 and 11.89 respectively. These simulation again meet expectations. The plots have local minimums and maximums that correlate to the distribution of bright and dark material properties. The Lat 0 Lon -45 Obs -45 simulation does serve as reference for geometric warping caused by the large FOV of the RSO Earth perspective image. The maximum caused by the Ocean glint can be clearly seen around 120 degrees orientation angle. The remaining Earthshine measurement below 120 degrees, though greater then $\frac{1}{3}$ of the remainder of our RSO perspective image, only accounts for $\frac{1}{6}$ of our orientation angle. Once again we do get a large suspect signal for the diffuse component of the ocean, though notable less then the Sunshine and diffuse clouds in both cases. We get a RMSE between the two reflections, after geometrically aligning the plots, of $\pm1.03$. This corresponds to an average radiance ratio of 2.6. This seems like a lot, but actually appears consistent with the apparent inverse spatial relationship of the perspective RSO images.

## Rotating Flat Plate Lat 0 Lon 90 Obs 90
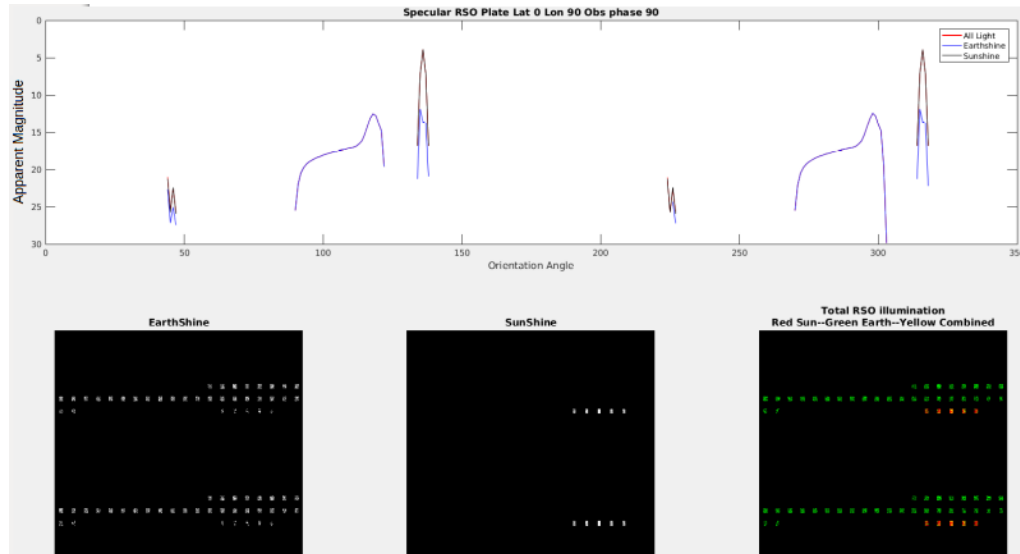


Figure 5.57: Real Earth specular flat plate Lat 0 Lon 90 Obs 90

## RSO Relative Earth Views
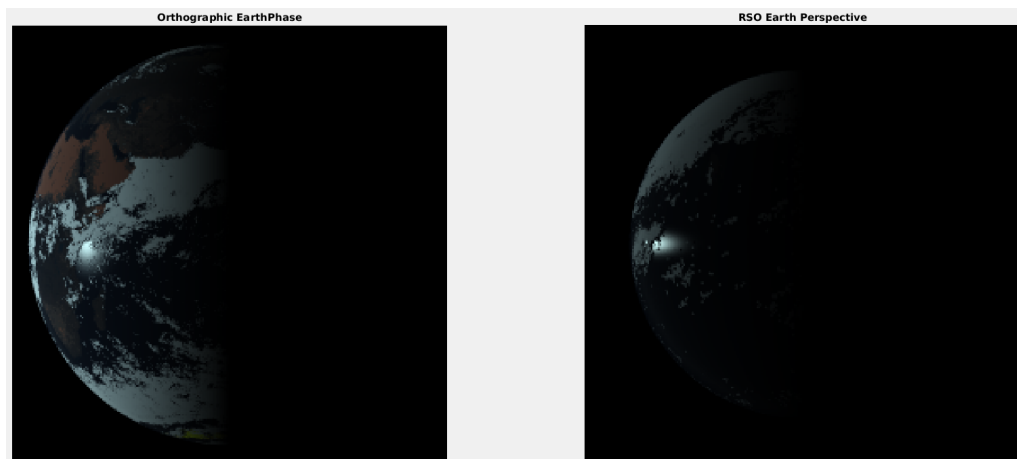


Figure 5.58: Lat 0 Lon 90 Obs 90 orthographic perspective view (left) RSO perspective view (right)

## Rotating Flat Plate Lat 0 Lon -90 Obs -90
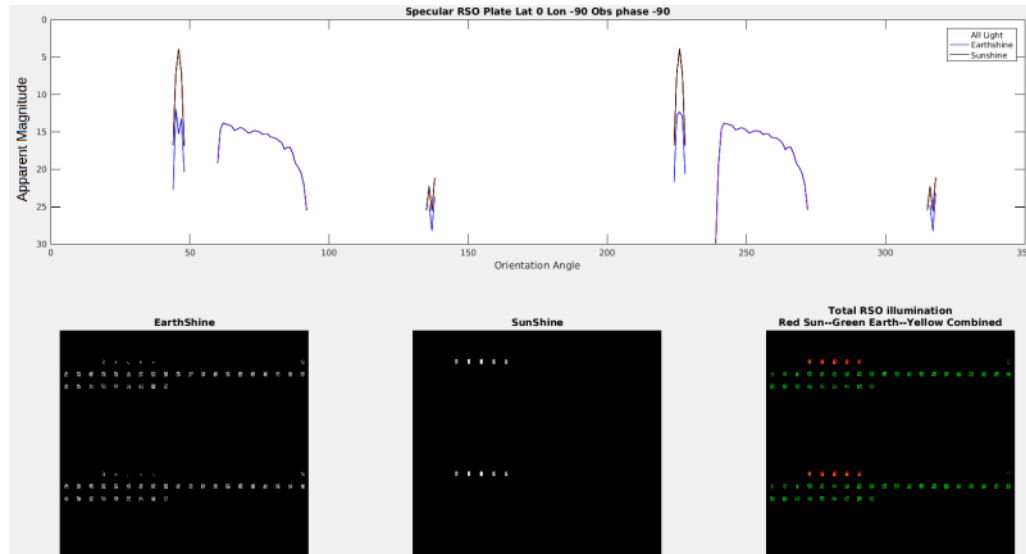


Figure 5.59: Real Earth specular flat plate Lat 0 Lon -90 Obs -90

## RSO Relative Earth Views
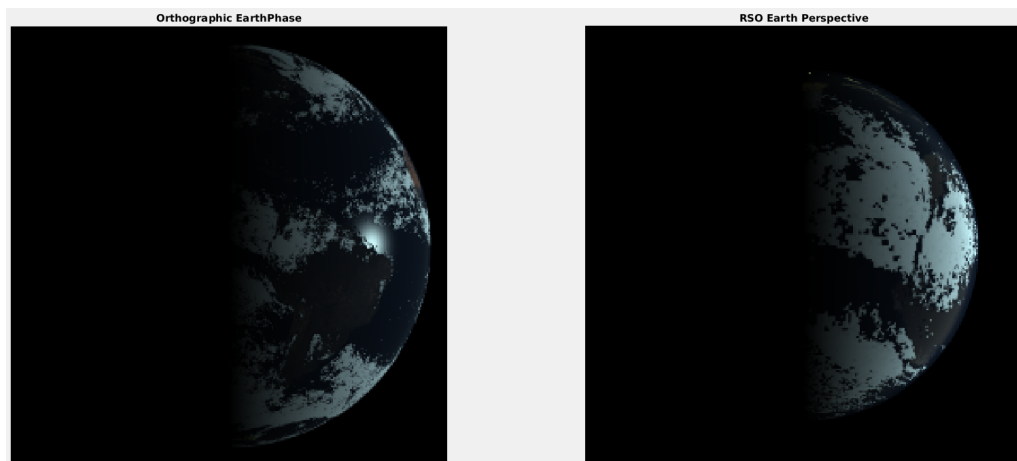


Figure 5.60: Lat 0 Lon -90 Obs -90 orthographic perspective view (left) RSO perspective view (right)

These simulations match our expectations well. The Lon 90 simulation
has the larger peak, with an apparent magnitude of 12.55, a radiance ratio of 8.0,
and a RMSE of ±1.41. The Lon -90 simulation has the observably brighter RSO
perspective with a peak Earthshine apparent magnitude of 13.85 compared to it's
homogeneous diffuse Earth flat plate RSO counter part of 14.81, a radiance ratio of
2.4, and a RMSE after geometrical alignment of ±0.73.
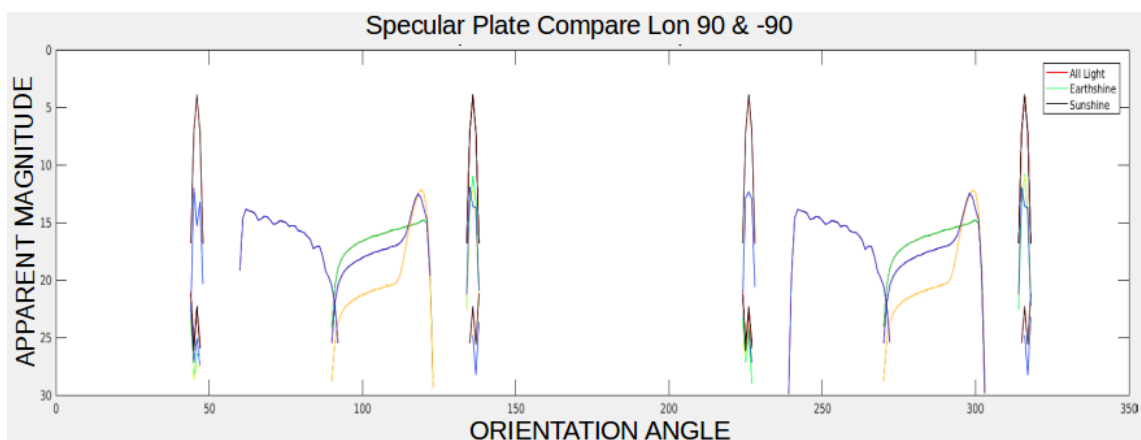


Figure 5.61: Real Earth Lat 0 Lon -90 Obs -90 (Centered at 180) and Lat 0 Lon 90
Obs 90 (Centered at 135) comparison of Real Earth (Blue) homogeneous specular
Earth [not included in analysis] (Yellow) and homogeneous diffuse Earth(Green)
Models

These simulations show how the diffuse model can really fail at encapsu-
lating the potential reflectance off the Earth. The diffuse model shows a dramatic
geometric fall off of Earthshine as we enter the limb of the Earth. In the presence of
a specular reflection of the sun in the ocean, this is not the case. We see a radiance
ratio as big as 8 and that is without a total specular reflection.

## 5.4 Summary of Results

In our spherical RSO examples, we found that regardless of material properties the
apparent magnitude RMSE was ≈ ±0.4, though the specular RSO had about 40%
larger Maximum Radiance ratios.

| Diffuse Sphere RSO | | | | | | | |
| --- | --- | --- | --- | --- | --- | --- | --- |
| Equatorial Orbit | | | | Polar Orbit | | | |
| Real Earth Max | Diff Earth Max | RMSE | Max Radiance Ratio | Real Earth Max | Diff Earth Max | RMSE | Max Radiance Ratio |
| 12.8 | 13.5 | 0.42 | 1.9 | 12.8 | 13.5 | 0.40 | 1.9 |
| Specular Sphere RSO | | | | | | | |
| Equatorial Orbit | | | | | | | |
| Real Earth Max | Diff Earth Max | RMSE | Max Radiance Ratio | Real Earth Max | Diff Earth Max | RMSE | Max Radiance Ratio |
| 13.57 | 13.94 | 0.41 | 2.4 | 12.85 | 13.94 | 0.36 | 2.73 |

Figure 5.62: Table of sphere results

Theoretically, the diffuse approximation may differ by an apparent magnitude deviation of $\approx 1.25$ given a RSO perspective made up of a specular reflection in the ocean and the rest clouds, or get apparent magnitude deviation $\approx 1.5$ given an ocean scene with a cloud big enough to just barely block the solar reflectance. But given a RSO perspective from an altitude of 1000km, this is unlikely.

Our flat plates we found to be much more sensitive to the heterogeneity of the Earth. With spherical RSOs, the hemispherical distribution of normals actually worked to mitigate the fall off of oblique SOOs. With the introduction of orientation, the error of our flat plates scaled with the incongruence between our real Earth model and a diffuse Earth model, coupled with the incongruence between the distribution on the diffuse spherical RSOs. We found for the diffuse flat plates there is are similar max radiance ratios as the diffuse spheres, but typically larger apparent magnitude RMSEs.

| Diffuse Sphere RSO | | | | | | | |
| --- | --- | --- | --- | --- | --- | --- | --- |
| Equatorial Orbit | | | | Polar Orbit | | | |
| Real Earth Max | Diff Earth Max | RMSE | Max Radiance Ratio | Real Earth Max | Diff Earth Max | RMSE | Max Radiance Ratio |
| 12.8 | 13.5 | 0.42 | 1.9 | 12.8 | 13.5 | 0.40 | 1.9 |
| Specular Sphere RSO | | | | | | | |
| Equatorial Orbit | | | | | | | |
| Real Earth Max | Diff Earth Max | RMSE | Max Radiance Ratio | Real Earth Max | Diff Earth Max | RMSE | Max Radiance Ratio |
| 13.57 | 13.94 | 0.41 | 2.4 | 12.85 | 13.94 | 0.36 | 2.73 |

Figure 5.63: Table of flat plate results

The specular flat plates are where we saw the largest incongruence between our models. The specular reflection can differ as much as the micro directional radiance

of the Earth can differ.  Theoretically, the apparent magnitude could differ by $\approx 2.5$ for a specular reflection off the ocean, or $\approx 1.5$ for a diffuse reflection off the water. While this is close to the theoretical limits of the other RSOs, the very small portion of the RSO perspective contributing to the observed Earthshine made this much more likely.

# Chapter 6

# Conclusion

## 6.1 Conclusion

We created a work flow which incorporated time sensitive satellite imagery and used it to create an Earth object in the radiative transfer engine DIRSIG. The Earth object created was determined from MODIS imagery to have an average spectral radiance RMSE of $\pm 14.86[\frac{watts}{m^2 sr \mu m}]$ over a sample of ROIs. Further analysis using EPIC imagery found a total radiance difference of $+3\%$ and a cross correlation of 0.656. Also using EPIC imagery it was found our Earth model produced a micro-region Earthshine radiance RMSE of $\pm 66[\frac{watts}{m^2 sr \mu m}]$ and a macro-region Earthshine radiance RMSE of $\pm 28[\frac{watts}{m^2 sr \mu m}]$ for objects with an altitude of 1000km. This was determined to result in an apparent magnitude error of $\pm 0.28$ for diffuse spherical RSOs, specular spherical RSOs, and diffuse flat plate RSOs with an altitude of 1000km. Also an apparent magnitude error of $\pm 0.66$ for specular flat plate RSOs with an altitude of 1000km.

We employed a homogeneous diffuse Earth and a real Earth model to explore how well a homogeneous diffuse sphere approximated the real Earth given different characteristic SOO phase, SEO phase, OBS ang, Orientation ang, material property, and RSO geometries. We showed a structural consistency with the phase and orientation dependence of the measured reflected Earthshine between the diffuse and real Earth models using the diffuse and specular spherical RSOs, and the diffuse plate RSOs. A RMSE of $\pm 0.4$ for both of the spheres and $\pm 0.8$ for the diffuse plate, and a max radiance ratio of 1.9, 2.7, and 2 respectively. We showed for the specular plate objects apparent magnitude RMSE of $\pm 1$ and a max radiance ratio of $\pm 8$.

In conclusion, with minimal RMSE, the visible Earthshine signature eminating from spherical RSOs with any BRDF or a diffuse plate RSO with an altitude of 1000km or greater, can be predicted using a diffuse sphere approximation of the Earth. Specular flat plates on the other hand have much more potential for statistically relevant error given a diffuse homogeneous Earth approximation. This paper includes calculations that future research may use to understand the potential need for a more robust approximation of the Earth for modeling the visible Earthshine signatures emanating from RSOs of different BRDFs and geometries.

## 6.2 Future Work

We ultimately sought to explore whether Earthshine could be leveraged to mitigate the risks posed by space debris. Our contribution was to build a tool which could do a temporally sensitive simulation of Earthshine illumination onto an RSO and then employ that tool to study the impact and variability on observed RSO apparent magnitude from Earthshine. One of the challenges of this work was to create an Earth object representative of the reflectance heterogeneity of the Earth given a time and date. The primary difficulties arose in accounting for the temporal variations of the clouds and the reflectance of the atmosphere. Future work may include using different sources of imagery to more accurately represent the cloud layer and explore different reflectance models to capture internal reflection of the atmosphere.

While this research did explore a large range of free parameters, many relevant parameterizations were not considered. Future work may include employing more real Earth models which explore the impact and variability due to season, time of day, and weather extremes. Different orbits, ideally those which are more representative of the orbits of existing debris fields, could be explored to better understand real reflected Earthshine orbital dynamics. More characteristic RSO geometries could be investigated; first off cylinders, which may serve as better representations of rocket bodies, but later geometries without symmetry. Imbuing our characteristic RSOs with material properties based on actual RSO materials could also help bridge the gap between theoretical and applicable.

Our study only considered generalized look angles in order to relate this work to the largest breadth of potential observers. Future work might consider specific observatories, taking into consideration parameterizations which were representative of real world scenarios. The primary goal of the inclusion would be to design survey strategies to perform experiments for collecting RSO measurements. A likely candidate for an observatory would be MCAT, utilizing its fast platform speed and capability for detecting dim objects.

Part of what we showed was Earthshine, given its out of phase relationship with the sun, has the potential to be a significant source of illumination for RSO detection. This is not the only benefit of having another out of phase source in the near Earth space environment. Future work may include utilization the known intensities and geometries of the two sources to uncouple geometric cross section and reflectance from optical cross section using a system of equations. Subsequent work could incorporate multiple measurements of a single RSO given different SEOs

and SOOs of a sphere to get a better uncoupling using an over determined system, or to take on more complex geometries.

Earthshine as a source of illumination on RSOs is a vast and relevant topic in mitigating the risks posed by space debris. Our work was the first known research into exploring this topic. While important and interesting results were obtain, much future work is needed to fully utilize Earthshine in protecting our near Earth space environment.

# Bibliography

[1] R. Wolfe, W. Esaias, A. Lyapustin, and X. Xiong, "Modis solar diffuser earth-shine modeling and analysis," in *SPIE Optics+ Photonics*. International Society for Optics and Photonics, 2006, pp. 629 606–629 606.

[2] D. Rutan, T. Charlock, F. Rose, S. Kato, S. Zentz, and L. Coleman, "Global surface albedo from ceres/terra surface and atmospheric radiation budget (sarb) data product," in *Proceedings of 12th conference on atmospheric radiation (AMS)*, vol. 11, no. 1. Citeseer, 2006, pp. 11–12.

[3] D. A. Bennett, J. A. Dank, D. W. Tyler, M. Gartley, and D. Allen, "Ssa modeling and simulation with dirsig," in *Advanced Maui Optical and Space Surveillance Technologies Conference. URL:¡ http://www. amostech. com/TechnicalPapers/2014/Poster/BENNETT*, 2014.

[4] J. Schott, "Remote sensing: The image chain approach," in *Oxford University Press*, 1997.

[5] U. N. O. for Outer Space Affairs (UNOOSA), "1967 treaty on principles governing the activities of states in the exploration and use of outer space, including the moon and other celestial bodies," jan 1967.

[6] C. P. Hoult and R. P. Wright, "Space surveillance catalog growth during sbirs low deployment," in *Aerospace Conference, 1999. Proceedings. 1999 IEEE*, vol. 4. IEEE, 1999, pp. 209–224.

[7] *Space Security 2010*. Pandora Press, 2010.

[8] T. Flohrer, H. Krag, H. Klinkrad, and T. Schildknecht, "Feasibility of performing space surveillance tasks with a proposed space-based optical architecture," *Advances in Space Research*, vol. 47, no. 6, pp. 1029–1042, 2011.

[9] J. R. Schott, S. D. Brown, A. Goodenough, and R. Raqueno. (1999) Dirsig. [Online]. Available: http://www.dirsig.org/docs/

[10] B. O'Connor, "Handbook for limiting orbital debris. nasa handbook 8719.14," *National Aeronautics and Space Administration, Washington, DC*, 2008.

[11] D. J. Kessler and B. G. Cour-Palais, "Collision frequency of artificial satellites: the creation of a debris belt," *Journal of Geophysical Research: Space Physics*, vol. 83, no. A6, pp. 2637–2646, 1978.

[12] V. Agapov and Z. Khutorovsky, "Analysis of rso's close approaches with the iss during two years flight," in *Space Debris*, vol. 473, 2001, pp. 433–439.

[13] S. Lederer, E. Stansbery, H. Cowardin, P. Hickson, L. Pace, K. Abercromby, P. Kervin, and R. Alliss, "The nasa meter class autonomous telescope: Ascension island," DTIC Document, Tech. Rep., 2013.

[14] M. Skolnik, "Radar handbook (2nd)," *McGraaw-Hill Book Company–New York., Cap*, vol. 39, 1990.

[15] M. Gruntman, "Passive optical detection of submillimeter and millimeter size space debris in low earth orbit," *Acta Astronautica*, vol. 105, no. 1, pp. 156–170, 2014.

[16] K. Fujimoto and D. Scheeres, "Correlation of optical observations of earth-orbiting objects and initial orbit determination," *Journal of guidance, control, and dynamics*, vol. 35, no. 1, pp. 208–221, 2012.

[17] J. R. Shell, "Commercially-hosted payloads for debris monitoring and mission assurance in geo," DTIC Document, Tech. Rep., 2011.

[18] T. Schildknecht, "Optical astrometry of fast moving objects using ccd detectors." *Geod.-Geophys. Arb. Schweiz, No. 49,*, vol. 49, 1994.

[19] P. Bely, *The design and construction of large optical telescopes*. Springer Science & Business Media, 2003.

[20] A. Massevitch and A. Losinsky, "Photographic tracking of artificial satellites," *Space Science Reviews*, vol. 11, no. 2-3, pp. 308–340, 1970.

[21] H. Cowardin, S. Lederer, G. Stansbery, P. Seitzer, B. Buckalew, K. Abercromby, and E. Barker, "Nasa's optical measurement program 2014," 2014.

[22] E. S. Barker, M. Matney, J.-C. Liou, K. Abercromby, H. Rodriquez, and P. Seitzer, "Comparison of orbital parameters for geo debris predicted by legend and observed by modest: Can sources of orbital debris be identified?" 2006.

[23] S. Navarro-Meza, M. Mommert, M. Reyes-Ruiz, D. E. Trilling, N. Butler, B. Pichardo, N. Moskovitz, and R. Jedicke, "First results from the rapid-response spectrophotometric characterization of near-earth objects using ratir," in *AAS/Division for Planetary Sciences Meeting Abstracts*, vol. 48, 2016.

[24] B. B. J. F. P. H. T. G. P. A.-M. E. B. G. S. H. COWARDIN, S. LEDERER and P. KERVIN., "The spie astronomical telescopes and instrumentation conference, 26 june 1 july, 2016, edinburgh, scotland, united kingdom." *Orbital Debris Quarterly*, vol. 20, 2016.

[25] G. H. Stokes, C. Von Braun, R. Sridharan, D. Harrison, and J. Sharma, "The space-based visible program," *Lincoln Laboratory Journal*, vol. 11, no. 2, pp. 205–238, 1998.

[26] M. Norkus, R. F. Baker, and R. E. Erl, "Evolving operations and decommissioning of the midcourse space experiment spacecraft," 2000.

[27] P. Goode, J. Qiu, V. Yurchyshyn, J. Hickey, M.-C. Chu, E. Kolbe, C. Brown, and S. Koonin, "Earthshine observations of the earth's reflectance," *Geophysical Research Letters*, vol. 28, no. 9, pp. 1671–1674, 2001.

[28] J. C. Stroeve and A. W. Nolin, "New methods to infer snow albedo from the misr instrument with applications to the greenland ice sheet," *IEEE Transactions on Geoscience and Remote Sensing*, vol. 40, no. 7, pp. 1616–1625, 2002.

[29] D. Wylie, D. L. Jackson, W. P. Menzel, and J. J. Bates, "Trends in global cloud cover in two decades of hirs observations," *Journal of climate*, vol. 18, no. 15, pp. 3021–3031, 2005.

[30] S. P. Mills, H. Agravante, B. Hauss, J. E. Klein, and S. C. Weiss, "Computer modeling of earthshine contamination on the viirs solar diffuser," in *Remote Sensing*. International Society for Optics and Photonics, 2005, pp. 59 780W–59 780W.

[31] G. L. Stephens, D. O'Brien, P. J. Webster, P. Pilewski, S. Kato, and J.-l. Li, "The albedo of earth," *Reviews of Geophysics*, vol. 53, no. 1, pp. 141–163, 2015.

[32] B. A. Wielicki, B. R. Barkstrom, B. A. Baum, T. P. Charlock, R. N. Green, D. P. Kratz, R. B. Lee, P. Minnis, G. L. Smith, T. Wong *et al.*, "Clouds and the earth's radiant energy system (ceres): algorithm overview," *IEEE Transactions on Geoscience and Remote Sensing*, vol. 36, no. 4, pp. 1127–1141, 1998.

[33] J. R. Schott, S. D. Brown, R. V. Raqueno, H. N. Gross, and G. Robinson, "An advanced synthetic image generation model and its application to multi/hyperspectral algorithm development," *Canadian Journal of Remote Sensing*, vol. 25, no. 2, pp. 99–111, 1999.

[34] B. Walter, "Notes on the ward brdf," *Proceedings of Technical Report PCG-05–06, Cornell Program of Computer Graphics*, 2005.

[35] W. Wanner, X. Li, and A. Strahler, "On the derivation of kernels for kernel-driven models of bidirectional reflectance," *Journal of Geophysical Research: Atmospheres*, vol. 100, no. D10, pp. 21 077–21 089, 1995.

[36] J. Monteith, "Vegetation and the atmosphere, vol. 1, principles," 1975.

[37] X. Li, A. Strahler *et al.*, "Geometric-optical bidirectional reflectance modeling of mutual shadowing effects of crowns in a forest canopy," *IEEE Transactions on Geoscience and Remote Sensing*, vol. 30, pp. 276–292, 1992.

[38] S. S. Inc. (2017) Modtran. [Online]. Available: https://www.rit.edu/ writobs/facility.htm

[39] C. Cox and W. Munk, "Measurement of the roughness of the sea surface from photographs of the suns glitter," *JOSA*, vol. 44, no. 11, pp. 838–850, 1954.